Summer 2019

Experimental Methods and Techniques for Improved Biomechanical Characterization of Diverse Murine Aortopathies

Brooks Alexander Lane

EXPERIMENTAL METHODS AND TECHNIQUES FOR IMPROVED BIOMECHANICAL CHARACTERIZATION OF DIVERSE MURINE AORTOPATHIES

by

Brooks Alexander Lane

Bachelor of Science
University of South Carolina, 2014

Submitted in Partial Fulfillment of the Requirements

For the Degree of Doctor of Philosophy in

Biomedical Engineering

College of Engineering and Computing

University of South Carolina

2019

Accepted by:

John F. Eberth, Major Professor

Susan Lessner, Committee Member

Mohamad Azhar, Committee Member

Tarek Shazly, Committee Member

Cheryl L. Addy, Vice Provost and Dean of the Graduate School

DEDICATION

I'd like to dedicate this work to my mother, Daisey, and my father, Clarence, for without their motivation, support, and advice beginning at the undergraduate level, I may have never joined the Biomedical Engineering Program at USC that sparked my interest in research and led me to pursue a graduate career.

ACKNOWLEDGEMENTS

First and foremost I'd like to acknowledge my advisor, Dr. John F. Eberth, for his continual guidance and abundant support throughout my studies, beginning from my first undergraduate research experience to the conclusion of graduate studies where he has allowed me to grow as a student and researcher. I'd also like to acknowledge my committee members – Dr. Susan Lessner, Dr. Mohamad Azhar, and Dr. Tarek Shazly – who have all devoted significant time and effort to this work and have always been willing and available to provide their expertise and engage in scientific discussion. I would like to thank my friends and colleagues David Prim, Colton Kostelnik, Nazli Gharraee, and Liya Du for their daily interaction, commiseration, and advice throughout periods of my graduate career. Lastly, I'd like to thank all the faculty and staff at the University of South Carolina Biomedical Engineering program, School of Medicine, and the Instrument Resource Facility for their active supporting roles throughout my studies.

ABSTRACT

Aortopathies constitute a broad class of diseases affecting the aorta – the largest artery responsible for distributing oxygenated blood to the systemic circulation. Specifically, aortic aneurysms (AAs) are described as a focal dilation of the vascular wall exceeding 50% of the normal vessel diameter. Ultimately AAs may stabilize, dissect, or rupture, with the latter virtually ensuring mortality. Currently clinicians consider prophylactic intervention based on size and growth-rate criteria that have been estimated from large-cohort statistical analyses. These criteria, however, fail to address the underlying mechanisms. Furthermore, 13% of small-to-mid sized AAs have been found to rupture prior to meeting these criteria. Clearly there exists a need for improved methods of evaluating aneurysm stability and predicting outcomes that can be utilized for patient-specific care strategies. Although advanced AAs are dangerous in the normal population, those suffering from heritable connective tissue disorders such as Loeys-Dietz Syndrome (LDS) present even greater clinical challenges. In either case, perioperative mortality rates for prophylactic repair are high, burdening clinicians with the decision to weigh the risks between intervention or rupture. Currently, there are no approved therapeutic management strategies for mitigation of AAs.

On the microstructural level, AAs present as complex, spatially heterogeneous tissues not well suited for analysis by conventional biomechanical techniques. In this dissertation we utilize gold nanoparticles to target degraded elastin at the site of murine

aneurysmal aortas and employ micro-computed tomography (micro-CT) to assess damage. Elastin is a key structural protein, fundamental to the healthy function of large arteries. Proteolytic degradation is performed using intraluminal elastase infusion to provide insight into the severity of AA disease with biaxial mechanical characteristics assessed *in situ*. We further utilize three mouse models of transforming growth factor beta (TGFβ) deficient mice (*Tgfb1*$^{+/-}$, *Tgfb2*$^{+/-}$, *Tgfb3*$^{+/-}$) to replicate the impaired passive and active mechanics of the ascending thoracic aorta that are commonly observed in LDS patients. These results are compared to controls and to the extreme case of elastase-induced thoracic AAs in order to capture the full spectrum of elastopathic aortic disease. To measure the complex strain fields from inflated and extended mouse AAs under physiological conditions, we developed and validated a device capable of full-field Stereo Digital Image Correlation (Stereo DIC) of submerged specimens. Bolstering experimental techniques for AA analysis that capture the complex soft tissue mechanical response can improve temporal and longitudinal studies that drive new therapeutic or interventional avenues with the potential for broad-reaching clinical translation. The associated mortality rates and lack of clinical options for AA patients motivate further studies to improve AA research in hopes of clarifying AA disease etiologies.

TABLE OF CONTENTS

LIST OF TABLES

LIST OF FIGURES

CHAPTER 1

INTRODUCTION – AORTOPATHIES

1.1 AORTIC PHYSIOLOGY & MICROSTRUCTURE OVERVIEW

Arteries of the systemic circulation share many common anatomical and physiological features and possess a structure-function relationship that enables optimal performance in their individual environments [1,2]. For example, the aorta is a large elastic conducting artery with dramatic microstructural variations that depend on the proximity to the heart and its local pulsatile environment [3]. The aorta consists of three tissue layers; a tunica intima, a tunica media, and a tunica adventitia. Although these layers are populated by their respective cell types, the different regions of the aorta (i.e. ascending thoracic vs. abdominal) contain varying amounts of each cellular and extra-cellular matrix (ECM) constituent. The innermost layer, the tunica intima, is a single layer of endothelial cells supported by a basal lamina predominantly composed of collagen type IV, laminin, and fibronectin, and is separated from an internal elastic lamina by a small amount of connective tissue and smooth muscle. This antithrombogenic inner layer helps to regulate transport while also providing transduced mechanical and chemical signals to mural cells. The bulk volume and load bearing layer of the artery is the tunica media, which contains smooth muscle cells that contribute to vascular tone through vasoconstriction or vasodilation, as well as a synthetic function involved in the production and remodeling of

the ECM. Fibroblasts are the predominant cell type of the outermost layer, the tunica adventitia, and play a role in ECM synthesis, turnover, and remodeling. In large blood vessels such as the aorta, bundles of nerves and smaller blood vessels (vasa vasorum) traverse the adventitia. Other cell populations are also present such as multipotent progenitor cells and resident immune cells (e.g., macrophages) [4–7].

Structurally, two major load-bearing proteins are found within the aortic wall: elastin and collagen. Together with the amorphous and gelatinous ground substance, the mechanical properties of arteries are endowed by the cellular interactions with these two constituents. Multiple types of collagen (type I, II, III, and IV) are present throughout, with types I and III accounting for 80-90% of total collagen content. Collagen has a turnover rate on the order of days to weeks, with excessive collagen deposition, or fibrosis, considered to be a pathological state [8,9]. Collagen fibers are undulated at low stretches and progressively engage upon stretch, eliciting a stiff non-linear material response [9]. In contrast, the ground substance is an amorphous, gelatinous, and viscous material filling the space between cells and proteins, consisting of bound and unbound water, glycosaminoglycans, and larger proteoglycans.

Elastin is formed into concentric layers called lamellae within the media, with the innermost lamella forming the boundary of the intima. A smaller amount of elastic fibers can also be found dispersed within the adventitia [10]. Elastic fibers consist of a crosslinked amorphous elastin core with several associated microfibrils (e.g., fibrillins, fibulins) [11]. Collectively, this constituent allows the aorta to distend during systole to accommodate the pulsatile blood ejected from the left ventricle and aortic valve. During diastole, the aorta recoils and uses the stored elastic energy to continuously propel blood to distal tissues in

an efficient process known as the Windkessel effect [12–14]. Ineffective elastin contributes to arterial stiffening, increased pulse wave velocity, pulse pressure propagation, and isolated systolic hypertension, and is therefore causal in numerous cardiovascular pathologies [15,16]. In healthy tissues, elastin turnover rates are on the order of 50 years and new elastin is not functionally cross-linked in adults. Therefore as a cardiovascular biomaterial, elastin has tremendous clinical significance [17]. In particular, defects in elastin contribute to aortic aneurysms and many other aortopathies [18,19].

1.2 ANEURYSM ETIOLOGIES

Aortopathies broadly encompass a wide range of cardiovascular diseases affecting the aorta, but this work will primarily focus on aneurysm and aneurysm-related aortopathies. Aortic aneurysms (AA) are broadly diagnosed as focal dilations of the arterial wall, prevalent in 8-16% in elderly populations age 65 or older, with 45,000 new AA diagnoses every year [20–22]. Although the exact etiology of non-syndromic abdominal aortic aneurysms (AAA) is unknown, risk factors and predispositions to AA disease include the male gender, smoking, and atherosclerosis [23]. On the other hand, syndromic forms of AAs normally present as thoracic aortic aneurysms (TAA) and are concomitant with genetic mutations that result in connective tissue disorders such as Loeys-Dietz Syndrome (LDS) [22,24]. LDS is caused by mutations in genes encoding for transforming growth factor-beta (TGFβ) and its signaling pathways. Patients with LDS often have rapidly progressing TAAs that lead to mortality at young ages [25]. Even though TGFβ dysfunction is clearly implicated in TAA formation of LDS patients, the underlying molecular mechanisms involved with individual TGFβ isoforms remain ambiguous and perplexing [26].

Although AAs may form in different regions (e.g., AAA, TAA) of the aorta and from different etiologies, AAs share similar complex microstructural maladaptive responses and features that ultimately lead to a spatially heterogeneous and weakened vasculature [3,27–30]. Histological examinations reveal chronic inflammation with medial degeneration and vascular smooth muscle cell apoptosis. Inflammatory cells and dysfunctional smooth muscle cells overexpress matrix metalloproteases (MMPs), leading to unbalanced collagen turnover and extensive elastin fragmentation and elastolysis [17]. Elastin fragments are also known pro-inflammatory chemoattractants, further eliciting immune responses and a vicious cycle of AA progression [31].

AA clinical outcomes range from stabilization to dissection and vessel failure (rupture). With no approved therapeutic strategies, clinicians are limited to invasive surgical or endovascular repair, making it a difficult decision on if, and when, to intervene. These decisions have a significant effect on patient outcomes [32]. Emergent AA interventions after rupture have abysmal patient outlooks, with 50% mortality before reaching the hospital; of those who make it to the hospital alive, only 60% survive repair operations [33,34]. For AAs diagnosed prior to rupture, clinicians consider prophylactic surgical repair based on AA size and growth rate criteria [35]. However, this does not address small-to-mid sized AAs that rupture prior to meeting interventional size criteria, or large asymptomatic AAs that eventually stabilize [36,37]. Additionally, perioperative mortality rates for prophylactic repair are still high, burdening clinicians with the decision to weigh risk between intervention or rupture [38,39]. Syndromic AAs pose an even more complex clinical challenge in that LDS TAAs show aggressive growth and increased propensities for dissection, requiring very early intervention with increased complexities

[40]. Therefore, there is a large need for improved methods of evaluating aneurysm stability and predicting outcomes that can be utilized for patient-specific care strategies. Emerging technologies, such as those utilizing gold nanoparticles (AuNPs), have previously shown utility in aneurysm diagnostics and histological assessments [41]. AuNPs are biologically inert, easily functionalized, and readily imaged through computed tomography (CT) imaging techniques, making them ideal for targeted drug delivery theranostic approaches for clinical treatments [42,43].

1.3 CHALLENGES IN ANEURYSM BIOMECHANICS

As described above, AA disease is associated with extracellular matrix (ECM) proteolysis and altered constituent turnover. These pathological processes generate complex spatially heterogeneous tissues with impaired mechanical stability. Current clinical indices employ Laplace's law (i.e., stresses are proportional to diameter of a cylinder) to assess aneurysm mechanics. Although this data is supported by large cohort studies, it is idealized, not mechanistic and ultimately fails to capture realistic loading modalities (heterogeneous, anisotropic) and artery geometry, resulting in poor clinical assessments. These limitations can lead to 13% rupture prior to meeting surgical criteria and 54% stable aneurysms exceeding size criteria [36,44,45].

The current indices are useful predictors but not comprehensive. Since AA disease has no therapeutic agent for mitigation, current research focuses have shifted to address the need for clinical improvements. Murine experimental models have been established [46–48] and are routinely used for *in vivo* studies of AA disease progression and therapeutic treatment [49–51]. However, standard *in vitro* biaxial mechanical analysis lacks the ability

to fully capture the complexity of AA mechanics. Thus, there is room for improvement in developing experimental techniques for *in vitro* and translational studies.

One promising approach seeks to address the complex and spatially heterogeneous AA mechanics through the use of stereo digital image correlation (StereoDIC), a powerful, non-contact optical imaging technique capable of measuring shape, deformation, and both in-plane and out-of-plane motions [52–54]. Stereo DIC can also be used in conjunction with standard biaxial mechanical analyses for improved material characterization. StereoDIC utilizes two cameras oriented at different perspectives but aimed at a common region to track a firmly adhered, yet randomly-generated speckle pattern on the specimen undergoing deformation. This data is used to calculate the localized surface strains and to reconstruct 3D shapes [55]. However, there are practical considerations in application of StereoDIC for strain measurements of soft tissues. First, soft tissues require adequate hydration while testing, which requires the addition of optical interfaces that introduce light distortion and bias in measurements. Secondly, as *in vitro* studies commonly utilize murine models, high magnification is required to obtain appropriate resolution in measurements of the strain field. These exacerbate light distortion effects at optical interfaces. Lastly, speckle patterning of murine arteries requires speckles on the order of 50-100 microns for adequate resolution, which proves challenging given traditional methods of ink application. Thus, to effectively implement StereoDIC for murine AA studies, one must take into account all of these considerations and validate the experimental set-up to ensure validity of measurements. With information gathered through StereoDIC, strain metrics can be used to assess local mechanical properties of AAs after therapeutic treatment or intervention to determine therapeutic efficacy in restoration of healthy arterial mechanics.

1.4 SUMMARY

Evaluating AA stability presents a complex problem for clinicians and researchers alike that must be overcome to improve future diagnostic and therapeutic treatments. In this dissertation, we use murine models of AAs to establish the potential for targeted gold nanoparticles localized to the AA site and correlate these with mechanical descriptors (Chapter 2). Additionally, we utilize murine models of altered TGFβ signaling (*Tgfb1*$^{+/-}$, *Tgfb2*$^{+/-}$, *Tgfb3*$^{+/-}$), common to LDS, to delineate changes in passive and active mechanical responses of the ascending aorta to reveal TGFβ ligand-specific effects on TAA. (Chapters 3 & 4). Lastly, we aim to present validation and error analysis of our StereoDIC device to enable future applications in strain field measurements for submerged murine aortic aneurysms (Chapter 5 & 6).

CHAPTER 2

FRAGMENTED ELASTIN-TARGETING GOLD NANOPARTICLES AS AN INDICATOR OF ANEURYSMAL MECHANICS[1]

[1] Lane BA, Wang X, Lessner SM, Vyavahare NR, Eberth JF. To be submitted to *Annals of Biomedical Engineering*

2.1 ABSTRACT

Although critical to clinical outcomes, the material properties of aortic aneurysms (AA) are difficult to assess using current non-invasive diagnostic techniques. Microstructural information such as the integrity of the proteinaceous network, however, could be used as a guide to predict if, and when, an AA requires surgical intervention. Here the degradation of a key structural protein, elastin, is assessed in the infrarenal section of the murine aorta using fragmented elastin-targeting gold nanoparticles (AuNPs). The corresponding signal-to-volume ratio of AuNP uptake in these tissues is quantified using non-invasive micro-computed tomography (micro-CT) and correlated with global metrics of biaxial mechanical behavior before and after 0, 0.5, and 10 U/ml of elastase infusion. After filtering the micro-CT signal, the gold-to-tissue volume ratios were found to increase with elastase concentrations, as did common geometric and mechanical hallmarks of AAs. The Spearman's Rho nonparametric measure of rank correlation indicated that gold-to-tissue volume ratios assessed at physiological conditions had positive correlations with diameter (ρ = 0.867, p-val=0.015), vessel dilation (ρ = 0.976, p-val = 0.015), and circumferential stress (ρ = 0.673, p-val =0.007) while correlating with decreases in wall thickness (ρ = -0.673, p-val = 0.017), circumferential stretch (ρ = -0.7234), area compliance (ρ = -0.831, p-val =0.003), and distensibility (ρ = -0.758, p-val = 0.005). In contrast, axial force and axial stress did not correlate with the micro-CT signal. These findings suggest that when combined with micro-CT, AuNPs can be used as a powerful tool in the estimation of mechanical and geometric features of aortic aneurysms.

2.2 INTRODUCTION

The clinical outcomes from aortic aneurysms (AA) include stabilization, dissection, and rupture. Often asymptomatic until aneurysm failure, patients requiring emergent surgical intervention have abysmal outcomes with 40% operative mortality [33,34]. To avoid this, clinicians consider prophylactic intervention based predominantly on AA size and growth rate criteria [35]. This surgical criterion was established based on large-cohort statistical studies, but fails to address the 13% of small-to-mid sized AAs that rupture prior to reaching minimum size criteria or the 54% of large, asymptomatic AAs that stabilize [36,37,44,45]. The limitations of a "one size fits all approach" arise, in part, from the large degree of heterogeneity, anisotropy, and asymmetric nature of arterial aneurysms [56–61]. Additionally, perioperative mortality rates for prophylactic repair remain high, burdening clinicians with the decision to weigh risk between intervention or rupture [38,39]. Currently, there are no approved therapeutic management strategies for mitigation of AAs; thus, the clinical options are limited to open surgical or endovascular repair [32]. AA disease is not limited to dilation and rupture, however, and other pathological hallmarks including vascular stiffening, systolic hypertension, inflammation, atherosclerosis, thrombosis, dissection, and dysfunctional mechanosensing are present, often with co-morbidities including myocardial infarction, claudication and even stroke [62,63]. Overall, there exists is a tremendous need for improved methods of evaluating aneurysm properties that can be utilized for patient-specific care strategies.

AA disease is associated with extracellular matrix (ECM) proteolysis and inflammation, ultimately leading to a weakening of the vascular wall [64–68]. Elastin degradation and dysfunction are key manifestations of AAs, eventually leading to

progressive dilatation and reduced distensibility [19,69–72]. Previous research by us, and by others, has shown that elastase infusion of large murine arteries generates a uniform, but significant, dilation *in vitro* that is well suited to biaxial analyses [18,73]. Moreover, a non-invasive diagnostic tool that provides visualization of local elastolysis, and thus disease severity, can enable clinicians to better evaluate aneurysm properties and the initiation of comorbidities [74].

Emerging technologies such as injectable gold nanoparticles (AuNP) can be adapted for AA diagnostics with targeted localization after systemic administration and readily imaged through computed tomography (CT) scans due to the high electron density of gold [42,75,76]. AuNPs can also be modified with bioactive agents or antibodies to improve localization and therapeutic benefits [77]. Previous research using a low-density lipoprotein (LDL) receptor knockout angiotensin-II infusion mouse model has shown that systemically administered, modified AuNPs tagged with an antibody against fragmented elastin localize to AAs and correlate to tissue failure in vivo [41], warranting further investigation of AuNP localization and arterial stability. In this work, we use micro-CT to investigate the uptake of fragmented-elastin targeted AuNP *in vitro* using arteries exposed to three concentrations of elastase (0, 0.5, 10 U/ml), each generating different degrees of elastolysis, and utilize standard biaxial mechanical analyses to determine the relationship between AuNP uptake and arterial mechanics.

2.3 METHODOLOGY

2.3.1 Specimen Preparation

All animal protocols were approved through the Institutional Animal Use and Care Committee at University of South Carolina. Wild-type 12-week-old C57BL/6J (JAX

#000664) mice were euthanized via carbon dioxide inhalation and perfused with saline solution supplemented with 30 U/mL heparin sodium via left ventricle puncture at 100 mm Hg. The abdominal aorta was isolated from the iliac bifurcation to the left renal artery via careful dissection from the surrounding perivascular tissues. Branches were carefully ligated using 10/0 nylon suture and the infrarenal aorta was cannulated on blunted 26G needles.

2.3.2 Biaxial Mechanical Testing and Data Analysis

The infrarenal aortas were mounted within our custom designed biaxial testing rig equipped with a thin load-beam cell (LCL-113G; Omega Engineering), pressure transducer (PX409; Omega Engineering), syringe pump (AL-1000; World Precision Instruments), and motorized axial actuator (Z825B; Thorlabs). All components are controlled and measurements are synchronized via a custom LabView code. The testing chamber was filled with phosphate buffered saline (PBS) solution, and PBS was flushed through the vessel lumen and device tubing to remove bubbles and to maintain tissue hydration throughout testing. The artery underwent five axial preconditioning cycles from unloaded length to 10% above the estimated *in vivo* stretch ratio (0 to 20-50 mN) followed by five cyclic pressurizations from 10-160 mmHg at the *in vivo* axial stretch ratio to minimize viscoelastic effects (see also citation [11]). The *in vivo* axial stretch was estimated through a series of axial-force extension tests at fixed luminal pressures to identify the force-pressure invariant relationship.

For data acquisition, the artery was extended to three axial stretch ratios (*in vivo* ± 10%) before undergoing three pressurization cycles (0-160 mmHg) with simultaneous force, inner and outer diameter, and pressure measurements at 10 mmHg increments. The

elastase treatment groups underwent the testing protocols described above, then the aorta was extended to the in vivo stretch and perfused intraluminally with 0.5 or 10 U/mL porcine pancreatic elastase solution and subsequently pressurized to 100 mmHg for 30 minutes. This treatment was followed by perfusion with Halt protease inhibitor cocktail containing aprotinin, a known serine protease inhibitor. The new unloaded geometry following elastase exposure was recorded and tissue subsequently underwent the same testing protocols described above at a common axial stretch ratio of 1.2 and maximum pressure of 140 mm Hg.

The mean circumferential σ_θ and axial σ_z stresses are calculated from the measured data using

$$\sigma_\theta = \frac{Pr_i}{h} \text{ , and } \sigma_z = \frac{F}{\pi(r_0^2 - r_i^2)}, \tag{2.1}$$

Likewise, the mid-wall circumferential λ_θ and axial λ_z stretch ratios are calculated from

$$\lambda_\theta = \frac{(r_i + r_o)}{(R_i + R_o)} \text{ , and } \lambda_z = \frac{l}{L}, \tag{2.2}$$

where r_i and r_o are the deformed inner and outer radii, R_i and R_o are the unloaded inner and outer radii, and l and L are the deformed and undeformed vessel lengths, respectively.

The lumen area compliance C_A and diameter distensibility D_d are estimated from [78]

$$C_A = \pi \frac{\Delta r_i^2}{\Delta P} \text{ , and } D_d = 2\frac{\Delta d_i / d_i}{\Delta P} \tag{2.3}$$

where ΔP is the change from diastolic to systolic transmural pressures (80 mmHg to 120 mmHg) with corresponding inner radii r_i and diameter measurements d_i at those loaded configurations.

2.3.3 Preparation and Use of Anti-Elastin Antibody-Conjugated Gold Nanoparticles

Fragmented elastin-targeted gold nanoparticles (AuNP) were synthesized as previously described [41]. Briefly, citrate-capped gold nanoparticles (150 ± 20 nm) underwent PEGylation and conjugation to a custom-made anti-elastin antibody (synthesized in-house at Clemson University) via carbodiimide EDC and Sulfo-NHS chemistry. The excess antibody was removed via centrifugation and nanoparticles were resuspended at a final concentration of 3 mg/mL in PBS. Prior to use, the AuNP suspension was periodically vortexed to create homogeneous solutions.

At the conclusion of mechanical testing, the infrarenal aorta was removed from the device and placed in PBS, where the branch ligatures were removed to provide the greatest intraluminal access for the AuNPs. The aorta was then placed in the gold nanoparticle solution on a shaker plate overnight at 4°C. The aortas were removed from the AuNP solution and placed in PBS for 1 hour on a shaker plate to remove excess unbound gold nanoparticles.

2.3.4 Micro-Computed Tomography Imaging

Aortas were immersed in corn oil and imaged (90 kV, 88 mAs, 18 x 18 voxel size, 0.2mm Cu filter) using a Quantum GX Micro-CT Imaging System (PerkinElmer). All CT scans were visualized and reconstructed using Caliper Micro-CT Analysis software by Analyze. Prior to analysis, each scan underwent stoichiometric Hounsfield unit calibration using the air above the sample and the specimen stage to obtain accurate relationships

between CT Hounsfield units and electron densities. Aortic tissue and gold nanoparticle signals were segmented separately and analyzed using the Caliper software Volume rendering feature.

2.3.5 Histology

Specimens were placed in PBS for one hour prior to Micro-CT imaging to rehydrate and then placed into fresh 4% paraformaldehyde at 4°C overnight. Samples were paraffin embedded, sectioned (5 μm) and stained with Hematoxylin and Eosin (H&E) for overall morphology. Elastin structures were identified through elastin autofluorescence using 470/22 excitation and 510/42 emission filters. Images were acquired on an EVOS FL Auto 2 microscope.

2.3.6 Statistics and Regression Analysis

Graphical results of mechanical data are presented as the mean ± standard error of the mean. The non-parametric analysis for calculating Spearman's Rho correlation coefficients ρ [1,-1] was performed to evaluate the strength of monotonic relationships between material/geometrical parameters and gold-to-tissue volume ratios with values of 1, 0 and -1 indicating strong, zero, or negative associations between parameters, respectively. Resulting significant relationships were plotted with Ordinary Least Squares (OLS) regressions. One-way ANOVA analysis was performed on micro-CT results and parameter comparisons between groups, * and ** denote p-values less than 0.10 and less than 0.05, respectively.

2.4 RESULTS

Controlled intraluminal elastase exposure at 100 mmHg for 30 minutes followed by perfusion of a protease inhibitor generated different magnitudes of dilation, 12 ± 3% for

0.5U/mL and 24 ± 1% for 10U/mL concentrations (Figure 2.1). Likewise, the entire pressure-diameter curve for elastase treated aortas shifted left (Figure 2.3A), illustrating a gradual dilation with increasing elastase concentrations. Dilation was due to a progressive fragmentation of the elastic microstructure (Figure 2.2). Axial force increased in vessels undergoing pressurization in the elastase treated groups (0.5U/mL = 14.26 mN; 10U/mL = 30.83 mN) compared to the force-invariant pressure relationship of the controls. This resulted in axial stiffening with higher axial stresses compared at a common stretch ratio (Control = 59.34 ± 2.39 kPa; 0.5U/mL: 92.28 ± 36.51 kPa; 10U/mL: 192.09 ± 55.82 kPa) (Figure 2.2B and 2.2D). A gradual increase in stiffness is also observed in the circumferential direction as shown by the left-shifted stretch-stress responses with higher circumferential stresses and lower circumferential stretches at 100 mm Hg (Control σ_θ = 70.24 ± 6.36 kPa, λ_θ = 1.5 ± 0.04; 0.5U/mL σ_θ = 108.22 ± 11.76, λ_θ = 1.45 ± 0.03; 10U/mL σ_θ = 134.54 ± 15.2 kPa, λ_θ = 1.17 ± 0.06) (Figure 2.3C). Micro-CT results showed an increase in localization of AuNPs within arterial tissues exposed to elastase when compared to controls, with gold-to-tissue signal volume ratios increasing along with elastase concentrations (Control = 0.37% ± 0.3%; 0.5U/mL = 4.70% ± 2.2%; 10U/mL = 7.56% ± 2.0%) (Figure 2.4 & 2.5). Some gold signal was present in the control tissues, especially around branches and near tissue incisions (Figure 2.4).

Spearman's Rho coefficients showed significant positive associations between dilation percentage (0.976), outer diameter (0.867), and circumferential stresses (0.673) and increases in gold-to-tissue signal volume ratio, whereas thickness (-0.673), circumferential stretch (-0.723), distensibility (-0.758), and lumen area compliance (-0.831) have negative but significant associations (Table 2.2). OLS regressions of these

variables are shown in Figure 2.6 and Figure 2.7, with the regression statistics which evaluate the strength of the linear relationship between the two variables displayed in Table 2.2. The percent dilation regression exhibited the greatest R^2 value (0.92), indicating a strong linear relationship; and the circumferential stretch had the lowest R^2 value (0.51), indicating a poorer linear fit. The means and standard deviations of control, 0.5U/mL, and 10U/mL treatment group geometric and material descriptors are shown in Table 2.1

2.5 DISCUSSION

Often elastase infusion experimental models are designed to eliminate elastin function within the artery to mimic extreme aneurysm phenotypes. In this work however, we perfused at both low and high elastase concentrations to induce a moderate aneurysm phenotype while using a control vessel also exposed to AuNPs. Medial thinning and a gradual loss of elastin after elastase perfusion resulted in biaxial mechanical changes reflected in the moderate to extreme dilation, showing gradual increases in axial and circumferential stresses and stiffening with increasing elastase concentrations. These changes recapitulate observations of increased vascular stiffening in the pathological progression of AAs [79,80]. Although greatly simplified, the resulting varied degree of elastolysis proves useful for *in vitro* analyses and quantification of mechanical properties in transient stages of AA disease in a configuration that is measurable using standard biaxial techniques [18,73].

As highlighted above, temporal progression and the severity of AA diseases can be reflected in deviations from the native homeostatic mechanical environment leading to maladaptive remodeling processes that further exacerbate disease progression. However, the current clinical diagnostic approach for aneurysm stability is limited to macroscopic

assessments with no histological context that lack a direct interpretation for mechanical stability [81]. To improve diagnostic approaches, and to build upon previous research revealing a correlation of elastin fragment-targeted AuNP localization to tissue failure [41], we showed that in two different severities of AA disease *in vitro*, elastin fragment-targeted AuNP localization is linked to mechanical descriptors of arterial tissues. The non-parametric Spearman's rank coefficient indicated that a greater localization of AuNPs (via gold-to-tissue volume ratio) is strongly associated with increased dilation, larger outer diameters, and increased circumferential stresses when measured at common loading conditions. Furthermore, increased AuNP localization was strongly associated with decreased medial thickness, diameter distensibility, and lumen area compliance. Although we are hesitant to assume a linear model, linear regression analyses revealed significant relationships between AuNP uptake and material descriptors, thereby further supporting links between AuNP localization and arterial mechanics.

Elastin degradation is a key manifestation of AAs, ultimately affecting the stability and function of the vessel wall. Identifying the relationships between localization of a fragmented elastin-targeting AuNP to local arterial mechanics enables clinicians to gather local histomechanical information directly linked to AA stability through routinely used CT imaging techniques. Paired with previous diagnostic and clinical indices, patient-specific care and intervention strategies can be refined to prevent unnecessary interventions or to advocate for prompt intervention prior to meeting established interventional criteria.

2.6 ACKNOWLEDGEMENTS

The authors would like to acknowledge Lorain Junor and Nazli Gharraee for their assistance in micro-CT training and analysis. This work was supported by the National Institutes of Health under grant number **(**R01HL133662) and in part by the National Science Foundation under grant number CMMI-1760906 (SML).

2.7 TABLES

Table 2.1: Geometric and Mechanical Descriptors. Summary of the mean geometrical, material, and stress parameters for controls, 0.5U/mL, and 10U/mL elastase-exposed infrarenal aortas. Data is presented as mean ± standard deviation. * and ** denote $P < 0.10$ and 0.05 respectively between elastase groups and the 0U controls. ^ denotes $P < 0.05$ between the 10U/mL and 0.5 U/mL treated elastase groups.

	Unloaded Dimensions		Loaded Dimensions & Stresses ($\lambda_z = \lambda_{iv}$ or 1.2, P = 100 mmHg)							Material Descriptors	
	Outer Diameter (μm)	Thickness (μm)	Outer Diameter (μm)	Dilation (%)	Thickness (μm)	Axial Force (mN)	λ_θ	σ_θ (kPa)	σ_z (kPa)	Diastolic-Systolic C_A (10^{-8} m^2/kPa)	Diastolic-Systolic D_d (mm Hg^{-1}x 10^2)
0U	649.51 ± 31.14	112.87 ± 14.19	861.08 ± 28.35	-	71.14 ± 3.26	10.37 ± 1.1	1.5 ± 0.04	70.24 ± 6.36	59.35 ± 4.14	1.24 ± 0.23	0.41 ± 0.09
0.5U	707.76 ± 12.41**	64.77 ± 2.85**	992 ± 35.69**	12% ± 3%	55.3 ± 5.95**	12.96 ± 7.77	1.45 ± 0.03**	108.22 ± 11.76**	92.27 ± 63.23	0.91 ± 0.23	0.21 ± 0.06**
10U	949.59 ± 76.02*^	59.54 ± 13.28**	1083.97 ± 44.15**^	25% ± 1%^	49.68 ± 6.66**	22.63 ± 0.66**^	1.17 ± 0.06**^	134.54 ± 15.2**^	192.08 ± 96.68**	0.88 ± 0.31*	0.19 ± 0.06**

Table 2.2: Spearman rho coefficients and Ordinary Least Squares (OLS) regression analysis. Summary of non-parametric statistical analysis to assess strengths of relationships between specified parameter and gold-to-tissue volume ratio, and OLS regression equation statistics ** indicates p-val < 0.05

			OLS Regression Statistics			
Parameter	Spearmans	P-value	Slope	Y-intercept	R^2	P-value
Dilation Percent (%)	0.9755**	<0.001	2.64	-0.0069	0.92	0.015
Outer Diameter (micron)	0.8667**	0.0027	4297.6	609.97	0.54	0.015
Circumferential Stress (kPa)	0.6727**	0.0394	776.29	76.549	0.62	0.007
Axial Stress (kPa)	0.5515	0.1043	1411.6	53.64	0.97	0.062
Axial Force (mN)	0.4545	0.1909	126.82	9.648	0.37	0.063
Thickness (micron)	-0.6727**	0.0394	-220.98	68.91	0.53	0.017
Circumferential Stretch	-0.7234**	0.018	-3.501	1.5424	0.51	0.02
Distensibility (mm Hg^{-1}) x 10^2	-0.7576**	0.0159	-0.0314	0.004	0.65	0.005
Lumen Area Compliance (m^2/kPa) x 10^{-8}	-0.8303**	0.0056	-6.9831	1.2597	0.69	0.003

2.8 FIGURES

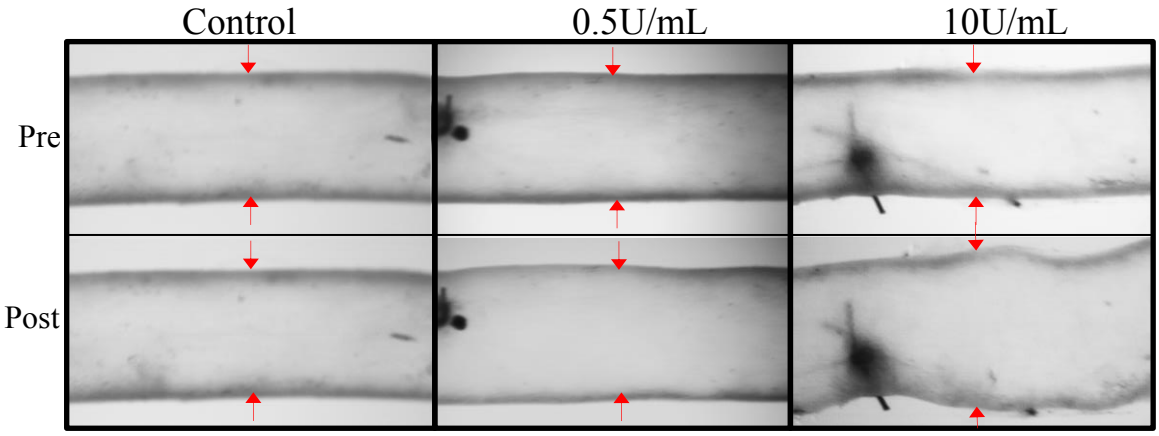

Figure 2.1: Elastase Exposure. Intraluminal perfusion of different concentrations of porcine pancreatic elastase (0, 0.5, 10 U/mL) for 30 minutes at 100 mm Hg and *in vivo* axial stretches produced varied degrees of damage and dilation of the infrarenal aorta.

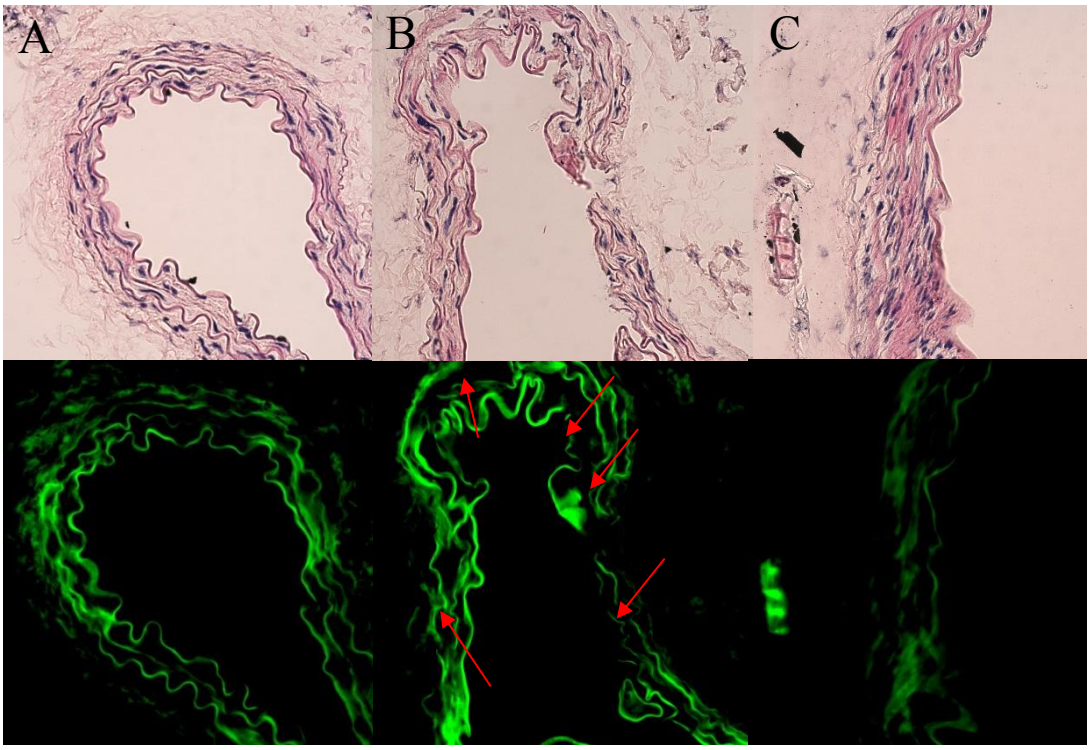

Figure 2.2: Representative samples of H&E stained and elastin auto fluorescence abdominal aortas following of intraluminal perfusion of A. 0 U/ml, B. 0.5 U/ml, and 10 U/ml porcine pancreatic elastase for 30 minutes with red arrows pointing to elastin fragmentation. Images taken at 40X magnification.

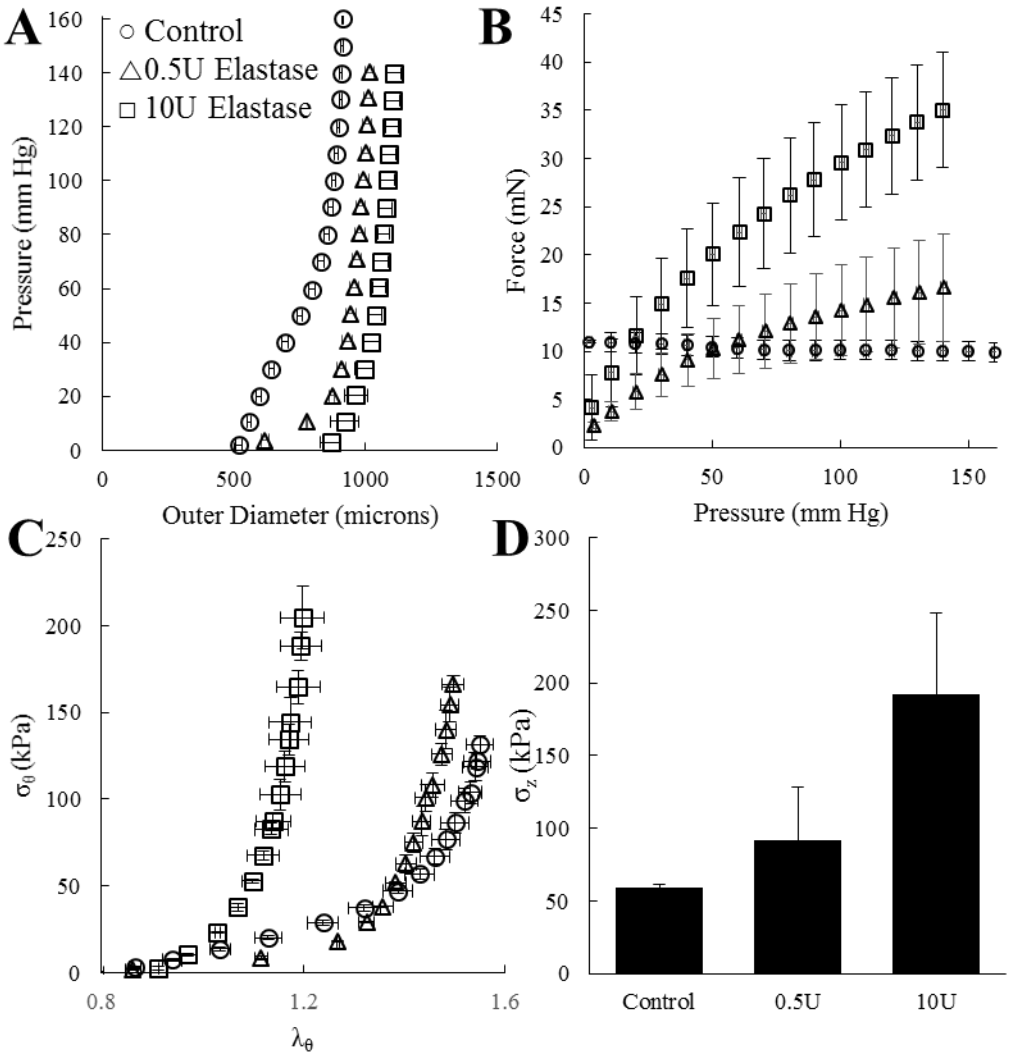

Figure 2.3: Averaged Biaxial Mechanical Data. A. Pressure-diameter B. Force-pressure C. Circumferential stretch-stress relationships between controls (0U/mL) (○), 0.5U/mL elastase (△), and 10U/mL elastase (□) exposed infrarenal aortas. D. Axial stress at 100 mm Hg and *in vivo* axial stretch for control and $\lambda_z = 1.2$ for elastase-exposed arteries. Data is presented as mean ± standard error of mean.

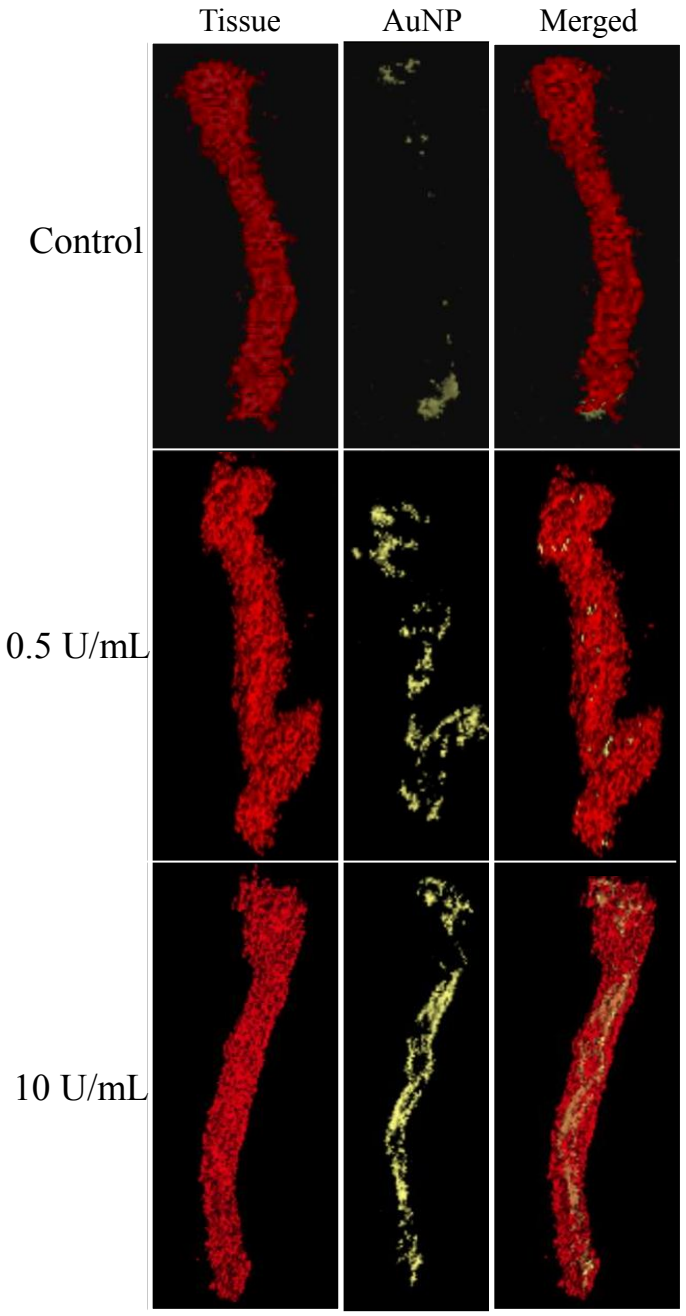

Figure 2.4: Micro-CT Results. Representative micro-CT scans of a control (top) and 0.5U/mL (middle) and 10U/mL (bottom) intraluminal elastase-perfused infrarenal aortas after overnight incubation in elastin-fragment targeted AuNP solution post biaxial mechanical testing

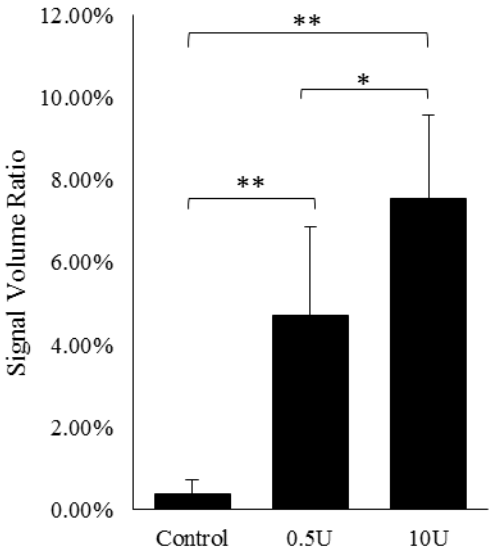

Figure 2.5: The ratio of volume of gold nanoparticles to total tissue volumes. * denotes p-val < 0.10 and ** denotes p-val < 0.05

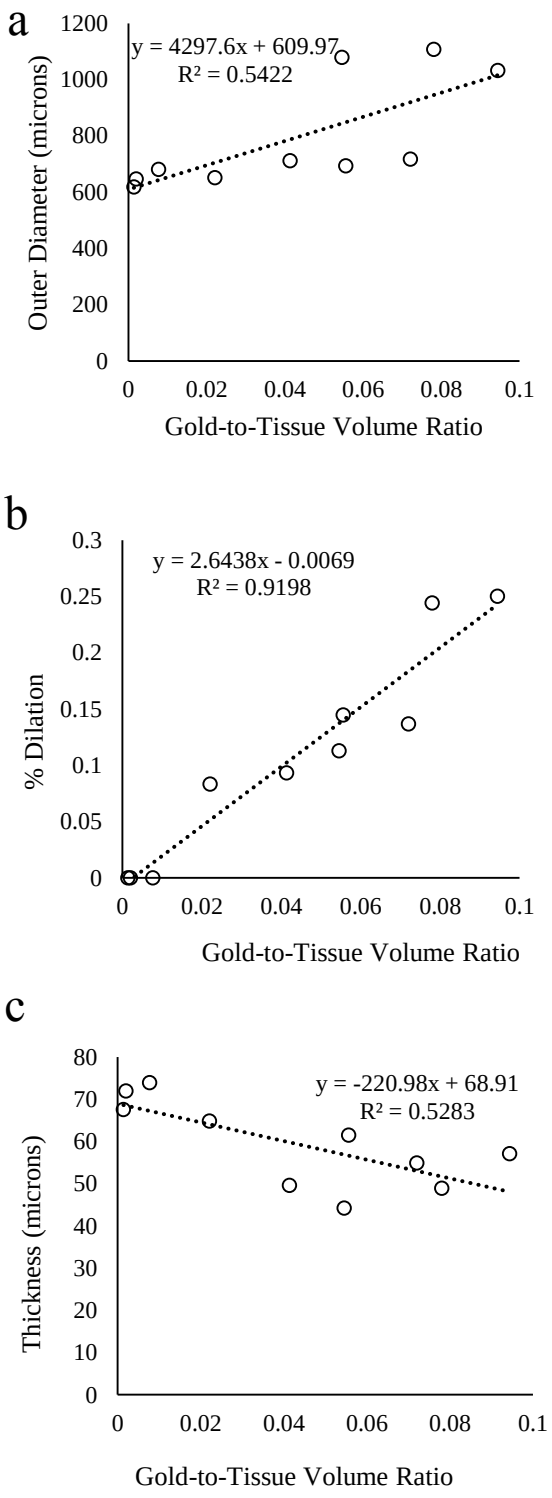

Figure 2.6: Ordinary Least Squares (OLS) Linear Regressions of geometric parameters and gold-to-tissue volume ratio. a-b show the significant, positive-trending linear relationships of outer diameter and percent dilation and c is the negative trending thickness relationship shown to be significant by Spearmans Rank-order statistical analysis.

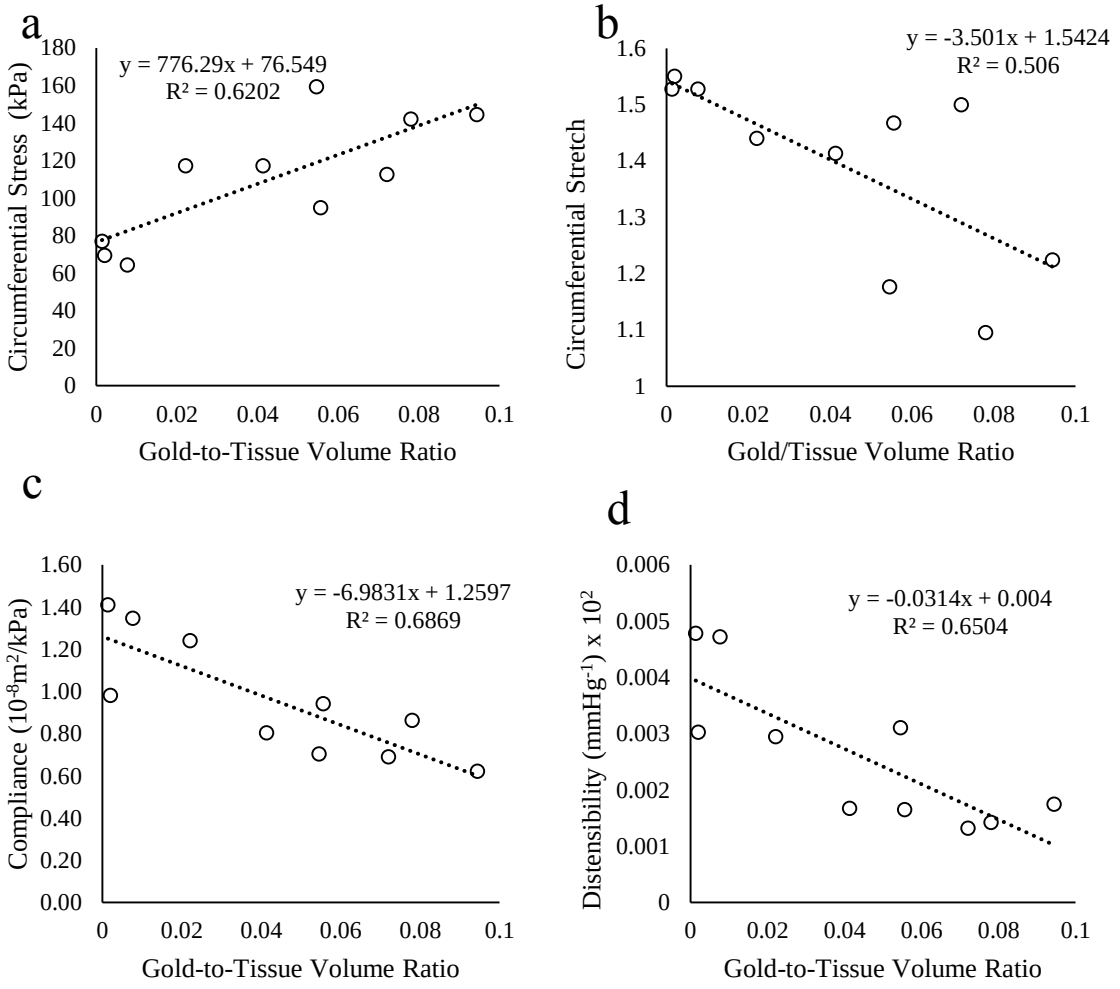

Figure 2.7: Ordinary Least Squares (OLS) Linear Regressions of mechanical and material descriptors and gold-to-tissue volume ratio. a) showing the positive-trending linear relationship with circumferential stress and b) the negative-trending linear relationship with circumferential stretch. c-d) are the negative-trending relationships of compliance and distensibility shown to be significant by Spearmans Rank-order statistical analysis

CHAPTER 3

DIFFERENTIAL MECHANICS OF THE ASCENDING AORTAS FROM TGFβ-1,-2, -3 HAPLOINSUFFICIENT AND ELASTASE INFUSED MICE[2]

[2] Lane B.A., Ferruzzi J., Chakrabarti M., Azhar M., and John F.E. To be submitted to *Laboratory Investigation*

3.1 ABSTRACT

The genetic causes of Loeys-Dietz syndrome (LDS) involve mutations to various genes encoding transforming growth factor beta (TGFβ) and its signaling molecules. LDS is characterized in part by diverse and deadly thoracic aortopathies. Although considerable attention has been paid to the mechanical properties of blood vessels harboring receptor and signaling pathway mutations, less is known about the role that individual TGFβ1, -β2, - β3 ligands play in the initiation and progression of thoracic aortopathies. Although these ligands act through the same receptor complex, each is expressed in unique yet overlapping fashion within the developing wall. In this investigation we studied the biaxial mechanical properties of the ascending thoracic aorta (ATA) from *Tgfb1*$^{+/-}$, *Tgfb2*$^{+/-}$, and *Tgfb3*$^{+/-}$ mice[3], their wild-type (WT) controls, and an elastase infusion model representative of complete elastic fiber network destruction. The latter was significantly different in virtually all metrics of comparison (outer diameter, thickness, axial force, stretch, stress, compliance) from the WT, *Tgfb1*$^{+/-}$, and *Tgfb2*$^{+/-}$ mice. *Tgfb1*$^{+/-}$ and *Tgfb2*$^{+/-}$ ATAs had no significant differences in circumferential stresses at systole (WT = 191.5 ± 30.99 kPa; *Tgfb1*$^{+/-}$ = 197.87 ± 3.07 kPa; *Tgfb2*$^{+/-}$ = 188.32 ± 9.12 kPa) from their WT counterparts. ATAs from *Tgfb2*$^{+/-}$ mice on the other hand, had a significant increase in loaded outer diameter when compared to *Tgfb1*$^{+/-}$. An increase in lumen area compliance was also observed in *Tgfb1*$^{+/-}$ (C_A = 0.1 ± 0.02 m^2/kPa × 10^{-8}) mice but conversely, this parameter decreased in *Tgfb2*$^{+/-}$ (C_A = 0.06 ± 0.01 m^2/kPa × 10^{-8}) mice compared to controls (C_A =

[3] At the time of submission, the *Tgfb3*$^{+/-}$ mice designed for use in the biaxial study had not reached maturity. A single sample (n=1) is included in Figure 3.4 but no conclusions are drawn from it due to the small sample size. Chapter 4 also contains uniaxial and myograph studies that include *Tgfb3*$^{+/-}$ mice (n=3). The current group of *Tgfb3*$^{+/-}$ mice will reach maturity and be tested prior to the submission of the completed manuscript.

0.08 ± 0.01 $m^2/kPa \times 10^{-8}$). Overall, *Tgfb1*$^{+/-}$ ATAs appeared vasoprotected while *Tgfb2*$^{+/-}$ mice were aortopathic at a level less severe than those generated using elastase infusion.

3.2 INTRODUCTION

Transforming growth factor beta (TGFβ) and its signaling pathways have been implicated in the initiation and progression of diverse thoracic aortopathies (TA) [82–87]. For example, Loeys-Dietz syndrome (LDS) patients have a propensity for sudden aortic dissection and can be divided into one of five subtypes (LDS1, LDS2, LDS3, LDS4, and LDS5) based on the underlying gene mutations that result in the syndrome (*TGFBR1*, *TGFBR2*, *SMAD3*, *TGFB2*, and *TGFB3*, respectively) [84,85,88–93]. In humans the TGFβ cytokine family is comprised of three isoforms (TGFβ1, -β2, -β3), each individually encoded by separate genes. Although these ligands act through a common receptor complex (TGFBR1/2), they regulate tissue development and vascular homeostasis via autocrine and/or paracrine signaling in a highly context-dependent and tissue-specific manner [82,87,94–98]. *Tgfb1*, *Tgfb2*, and *Tgfb3* genes, for example, are expressed in a distinct yet overlapping fashion in the developing mouse aorta with *Tgfb2* and *Tgfb3* abundantly expressed in the SMCs of the medial wall, while *Tgfb1* is the predominant isoform in the endothelium [82,99–102]**.** Given the unique and non-overlapping, multifactorial nature of TGFβ function (dozens of phenotypes among the three TGFβ ligand mice, reviewed in [103]), there are numerous potential mechanisms through which TGFβ could affect the complex differentiation and morphogenetic processes required for healthy aortic wall development. Thus, mutations can lead to diverse thoracic aortopathies. Further examination of TGFβ signaling dysfunction and the resultant propensity for TAs

through biomechanical analyses can delineate pathological manifestation and progression details on a vessel-level scale.

Mutations in *TGFB2,* and more recently *TGFB3* genes, are connected to familial TAs even though the receptors and other signaling pathways remain intact [84,85,88–90,92]. While it is evident that appropriate TGFβ signaling is essential to vascular homeostasis, the individual role TGFβ ligands play in aortopathy initiation and progression remains vague. Likewise, previous research has established murine models employing conditional TGFBR2 mutations to mimic LDS [104,105]. However, TGFBR2 mutant mice blockade all TGFβ ligand signal transduction, and as such, obscure the individual roles of these ligands in TA pathogenesis. Regardless, the effect of discrete TGFβ ligand dysfunction on arterial mechanics has yet to be established. A systematic comparison of genetic mutations in individual TGFβ ligands and resultant phenotypes can reveal pivotal information to appropriately manage LDS with therapeutic or surgical strategies. Thus, in this work we examine the biaxial mechanical properties of ascending thoracic aortas from global heterozygous mutant mice: *Tgfb1*$^{+/-}$, *Tgfb2*$^{+/-}$, and *Tgfb3*$^{+/-}$ and their controls. Furthermore, an elastase infusion model is used for comparison to show effects of extreme elastin destruction. All mice are examined at a predetermined transient disease stage to delineate the effect on overall vessel mechanics.

3.3 METHODOLOGY

3.3.1 Specimen Preparation

All animal protocols were approved through the Institutional Animal Use and Care Committee at University of South Carolina. *Tgfb* haploinsufficient mice aged 4-6 month (*Tgfb*1$^{+/-}$ n = 3; *Tgfb*2$^{+/-}$ n = 6; *Tgfb*3$^{+/-}$ n = 1) and aged matched wild-type controls (n=5)

were euthanized via carbon dioxide inhalation and perfused through a left ventricle puncture with saline solution supplemented with 30 U/mL heparin sodium at 100 mmHg. The ascending aorta was dissected free from the surrounding perivascular tissues from the aortic root to the brachiocephalic trunk. The left common carotid, subclavian artery, and distal descending aorta were ligated using 10/0 nylon suture. The ascending aorta was cannulated through the right innominate artery and at the aortic root using blunted 26G and 22G needles, respectively.

3.3.2 Biaxial Mechanical Testing

The ascending aorta was mounted within our testing system equipped with a thin load-beam cell (Omega Engineering; LCL-113G), pressure transducer (Omega Engineering; PX409), and syringe pump that were all integrated and controlled via a custom LabView code. The arteries all underwent five axial preconditioning cycles from the unloaded lengths to 10% above the estimated *in vivo* stretch ratio (0 to 20-50 mN) followed by five cyclic pressurizations from 10-160 mmHg at the *in vivo* axial stretch ratio to remove tissue viscoelastic response. The *in vivo* axial stretch was estimated through a series of axial-force extension tests at fixed luminal pressures to determine the length that exhibits a force-pressure invariant relationship.

For data acquisition, the artery was extended to three axial stretch ratios (*in vivo* ratio ± 10%) and underwent three pressurization cycles from 0-160 mmHg with simultaneous force, inner and outer diameter, and pressure measurements at 10 mmHg increments. For the elastase-treated controls, following normal testing protocols, the aorta was extended to the in vivo stretch and perfused intraluminally with 10 U/mL porcine pancreatic elastase solution. It was then pressurized to 100 mmHg for 30 minutes, followed

by perfusion with Halt protease inhibitor (ThermoFisher Scientific; Cat. No. 87786) cocktail containing aprotinin. The new unloaded geometry following elastase exposure was recorded, and the vessel subsequently underwent aforementioned testing protocols at only one axial stretch ratio of 1.2. A single stretch ratio was tested due to an observed tissue instability.

The average circumferential σ_θ and axial σ_z stresses are calculated with standard formulas

$$\sigma_\theta = \frac{Pr_i}{h} \text{ and } \sigma_z = \frac{F}{\pi(r_0^2 - r_i^2)}, \tag{3.1}$$

where P is the transmural pressure, F the axial force, h the wall thickness, r_i the deformed inner radius and r_o the deformed outer radius.

The mid-wall circumferential λ_θ and axial λ_z ratios are calculated from

$$\lambda_\theta = \frac{(r_i + r_o)}{(R_i + R_o)} \text{ and } \lambda_z = \frac{l}{L}, \tag{3.2}$$

with R_i and R_o are the unloaded inner and outer radii, and l and L are the deformed and undeformed vessel lengths, respectively.

The lumen area compliance C_A is estimated from [78]

$$C_A = \pi \frac{\Delta r_i^2}{\Delta P} \tag{3.3}$$

where ΔP is the change from diastolic to systolic transmural pressures (80 mmHg to 120 mmHg) with corresponding inner radii measurements at those loaded configurations.

3.3.3 Histology

At the conclusion of mechanical testing, all vessels were placed in fresh 4% paraformaldehyde solution in their unloaded states at 4°C overnight. Samples were paraffin embedded, sectioned (5 μm) and stained with Hematoxylin and Eosin (H&E) for overall morphology. Elastin structures were identified through elastin autofluorescence using 470/22 excitation and 510/42 emission filters. Images were acquired on an EVOS FL Auto 2 microscope.

3.3.4 Statistics

Statistical analysis was performed using one-way ANOVA analysis between each genotype and wild-type controls as well as between *Tgfb* haploinsufficient groups. P-values less than 0.10 were deemed statistically significant.

3.4 RESULTS

Overall, morphological assessments and biaxial mechanical testing of the ATAs reveal subtle differences in the tested *Tgfb* haploinsufficient models compared to wild-type controls. *Tgfb1*$^{+/-}$ ATAs exhibited on average smaller unloaded inner diameters and loaded outer diameters compared to control and *Tgfb2*$^{+/-}$ mice (Controls: p-val = 0.04 and p-val = 0.03, respectively; *Tgfb2*$^{+/-}$: p-val = 0.007 and p-val = 0.058, respectively), and qualitatively appear to have altered ATA curvatures compared to wild-type controls. *Tgfb2*$^{+/-}$ show slight dilation, although not statistically significant compared to controls (p-val = 0.19) but were significantly dilated compared to *Tgfb1*$^{+/-}$ (p-val = 0.058), with loss of distinct right innominate branch artery origin and angle from the arch. *Tgfb2*$^{+/-}$ mice also have a slight yet statistically significant increase in loaded thicknesses compared to wild-types (p-val = 0.10). *Tgfb3*$^{+/-}$, although limited in sample size, exhibit milder phenotypes

than both *Tgfb1* and *Tgfb2* heterozygous mice, appearing axially shorter with qualitatively altered inner and outer curvatures (Figure 3.1). Histologically, $Tgfb1^{+/-}$ showed healthy elastin lamellae and structures throughout the arterial wall, similar to the wild-type controls. $Tgfb2^{+/-}$ aortas showed early signs of elastin fragmentation although not ubiquitous throughout the sections. The elastin lamellae were significantly fragmented with a large loss of elastin structures in comparison to the age-matched wild-types.

Elastase perfused controls demonstrate severe loss of elastin integrity resulting in severe dilation and stiffening at physiological pressures (Figure 3.3A), with significant increases in loaded and unloaded diameters, increased circumferential stresses, and decreased wall thickness and lumen area compliance compared to controls and *Tgfb* heterozygous mouse models (see Table 3.1) All haploinsufficient ATAs exhibited similar magnitudes of axial force measurements under inflation, whereas the elastase models show increases in force over pressure cycling, although at smaller magnitudes due to testing limitations of axial stretch due to tissue instability at right innominate artery branch ligation (Figure 3.3B). $Tgfb1^{+/-}$ and $Tgfb2^{+/-}$, although slightly undersized and dilated, respectively, exhibit a more compliant circumferential stress-stretch relationships with higher circumferential stretches at systolic pressures (WT = 1.61 ± 0.05; $Tgfb1^{+/-}$ = 1.73 ± 0.03, p-val = 0.003; $Tgfb2^{+/-}$ = 1.75 ± 0.13, p-val = 0.02) with no significant differences in circumferential stresses (WT = 191.5 ± 30.99 kPa; $Tgfb1^{+/-}$ = 197.87 ± 3.07 kPa; $Tgfb2^{+/-}$ = 188.32 ± 9.12 kPa) in comparison to wild-type controls (Figure 3.3C). $Tgfb1^{+/-}$ ATAs show increased axial stresses, while $Tgfb2^{+/-}$ show reduced axial stresses in comparison to wild-types, although these differences were not statistically significant at *in vivo* axial stretches, calculated at the deformed state at 120 mm Hg (Figure 3.3D). However, $Tgfb2^{+/-}$

- did show a significant decrease in axial stresses compared to *Tgfb1*$^{+/-}$ mice (*Tgfb2*$^{+/-}$ = 44.78 ± 8.19; *Tgfb1*$^{+/-}$ = 58.51 ± 11.16, p-val = 0.07). Furthermore, we observe a significant increase in lumen area compliance of *Tgfb1*$^{+/-}$ (C_A = 0.1 ± 0.02 m^2/kPa × 10^{-8}, p-val = 0.08) but a decrease in *Tgfb2*$^{+/--}$ mice (C_A = 0.06 ± 0.01 m^2/kPa × 10^{-8}, p-val = 0.06) compared to controls (C_A = 0.08 ± 0.01 m^2/kPa × 10^{-8}), with significant differences also noted between *Tgfb1*$^{+/-}$ and *Tgfb2*$^{+/-}$ mice (p-val = 0.018). A summary of unloaded and loaded dimensions, in addition to loaded stress parameters and lumen area compliance, is shown in Table 3.1. Although a sample size of only 1 cannot be used for comparison, the *Tgfb3*$^{+/-}$ pressure-response is comparable to wild-type controls but also displays a moderately compliant circumferential stretch response with higher circumferential stresses (λ_θ = 1.80, σ_θ = 230.8 kPa). Additionally, the preliminary data suggests higher axial stresses at systolic pressures in *Tgfb3*$^{+/-}$ mice compared to wild-types (WT 49.74 ± 7.9; *Tgfb3*$^{+/-}$ 62.2 kPa) (Figure 3.4). Further testing will be required to form stronger conclusions for the *Tgfb3*$^{+/-}$ group.

3.5 DISCUSSION

Although biaxial mechanical analysis across all *Tgfb* ligand haploinsufficient mouse strains is incomplete at this time (lacking sufficient sample sizes of *Tgfb3*$^{+/-}$), we can briefly address apparent manifestations of *Tgfb1* and *Tgfb2* ligand signaling dysfunction in the ATA biaxial mechanical properties. Reduced *Tgfb1* signaling shows a significant reduction in loaded outer diameters, while reduced *Tgfb2* signaling contributes to mild but not statistically significant aortic dilation at 6 months, possibly suggesting early aneurysm pathogenesis, as seen in LDS [106] and noted from Dr. Azhar's previous work showing increased dilation and aneurysm formation at 9 months of age through ultrasound

studies (unpublished). Additionally, *Tgfb2*$^{+/-}$ mice did show a significant increase in loaded ATA outer diameters compared to *Tgfb1*$^{+/-}$ mice. While reduced *Tgfb1* or *Tgfb2* ligands result in distinct macroscopic changes, interestingly, both genotypes exhibit similar transient compliant circumferential stress-stretch relationships compared to controls at this period in aortopathic progression, suggesting compensatory maladaptive signaling resulting in microstructural environments that may promote further pathogenesis. A more detailed discussion will follow after all datasets are completed.

3.6 ACKNOWLEDGEMENTS

We would like to thank members of Dr. Azhar's lab: John Johnson and Aniket Bhattacharya for their assistance in animal genotyping, care, and arterial dissections. We would also like to acknowledge Shahd Hasanain for her assistance in data collection and processing. This work was supported through funding from the American Heart Association (17GRNT33650018) and by the National Institutes of Health under grant number **(**R01HL133662).

3.7 TABLES

Table 3.1: Biaxial data from Ascending Thoracic Aorta (ATA) from wild-type (WT), *Tgfb1*$^{+/-}$, *Tgfb2*$^{+/-}$, and elastase mouse models. * indicates significance compared to wild-types, ^ indicates significance compared to elastase model, and # indicates significance compared to *Tgfb1*$^{+/-}$ model. p-val < 0.10 was considered statistically significant.

	Unloaded Dimensions			Loaded Dimensions & Mechanical Properties							
	Outer Diameter (μm)	Inner Diameter (μm)	Thickness (μm)	Outer Diameter (μm)	Thickness (μm)	Axial Force (mN)	λ_w	λ_θ	σ_θ (kPa)	σ_z (kPa)	Diastolic-Systolic C_A (10^{-8} m^2/kPa)
WT	1152.35 ± 18.83^	979.03 ± 5.73^	86.66 ± 10.1^	1808.97 ± 30.85^	78.66 ± 9.66^	19.61 ± 1.94^	1.59 ± 0.06	1.61 ± 0.05^	191.5 ± 30.99^	49.74 ± 7.9^	0.08 ± 0.01^
***Tgfb1*$^{+/-}$**	1115.82 ± 40.88^	802.34 ± 25.16*^	156.74 ± 13.43*^	1736.02 ± 45.84*^	70.74 ± 2.09^	21.52 ± 4.36^	1.58 ± 0.01	1.8 ± 0.04*^	197.87 ± 3.07^	60.33 ± 17.48^	0.1 ± 0.02*^
***Tgfb2*$^{+/-}$**	1172.36 ± 73.34^	875.17 ± 28.71^	148.59 ± 38.1*^#	1874.46 ± 87.02^#	82.85 ± 10.79^#	21.08 ± 1.66^	1.67 ± 0.1	1.79 ± 0.13*^	188.32 ± 9.12^	47.04 ± 6.53^	0.06 ± 0.01*^
***Tgfb3*$^{+/-}$**						Not included					
Elastase	2003.49 ± 127.56	1868.71 ± 115.55	67.39 ± 9.47	2072.77 ± 15.63	50.77 ± 2.32	11.2 ± 6.03	1.2 ± 0	1.04 ± 0.07	260.87 ± 14.58	34.65 ± 18.68	0.02 ± 0.0047

3.8 FIGURES

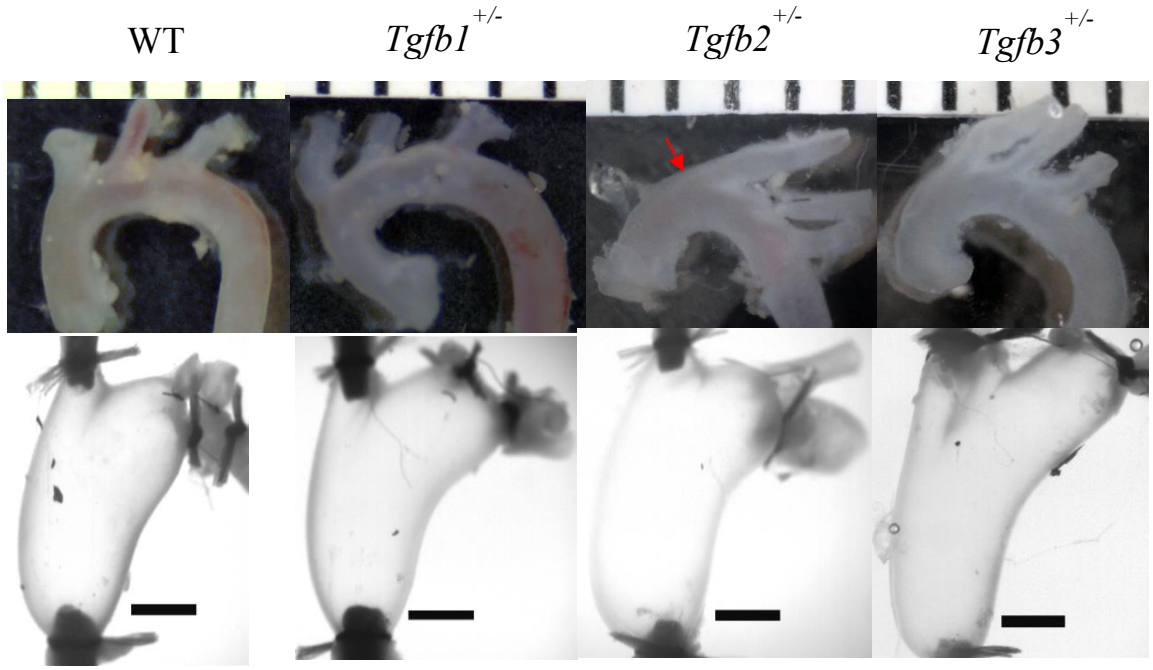

Figure 3.1: Ascending Thoracic Aorta Phenotypes. Representative images of the ascending thoracic aorta from wild-type (WT), *Tgfb*1$^{+/-}$, *Tgfb*2$^{+/-}$, and *Tgfb*3$^{+/-}$ mouse models prior to and after cannulation at 100 mm Hg. Scale bars in cannulated images are 1 mm.

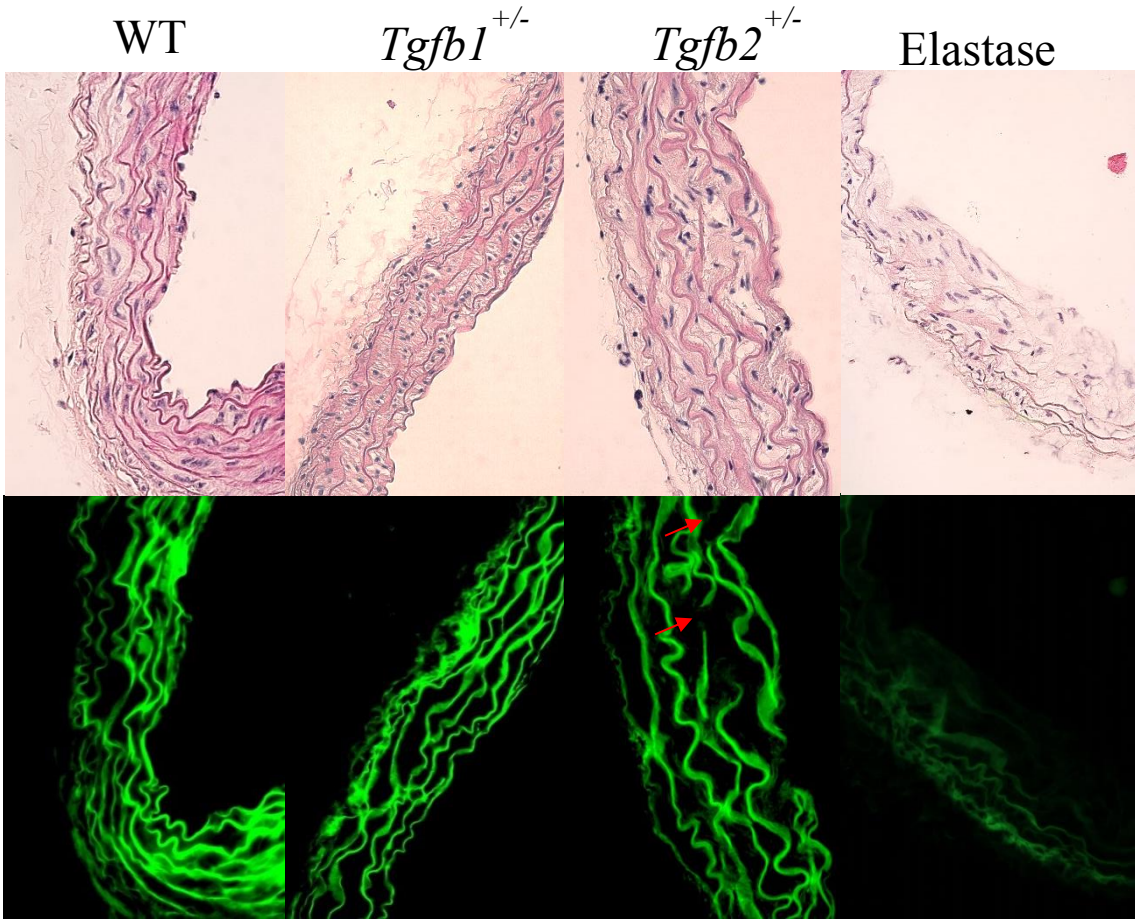

Figure 3.2: Histological Examination of ATA. H&E stains and corresponding elastin autofluorescence to examine elastin structures within the ATA of each *Tgfb* haploinsufficient murine models in comparison with wild-type control with red arrows pointing to elastin fragmentation. Images taken at 40X magnification.

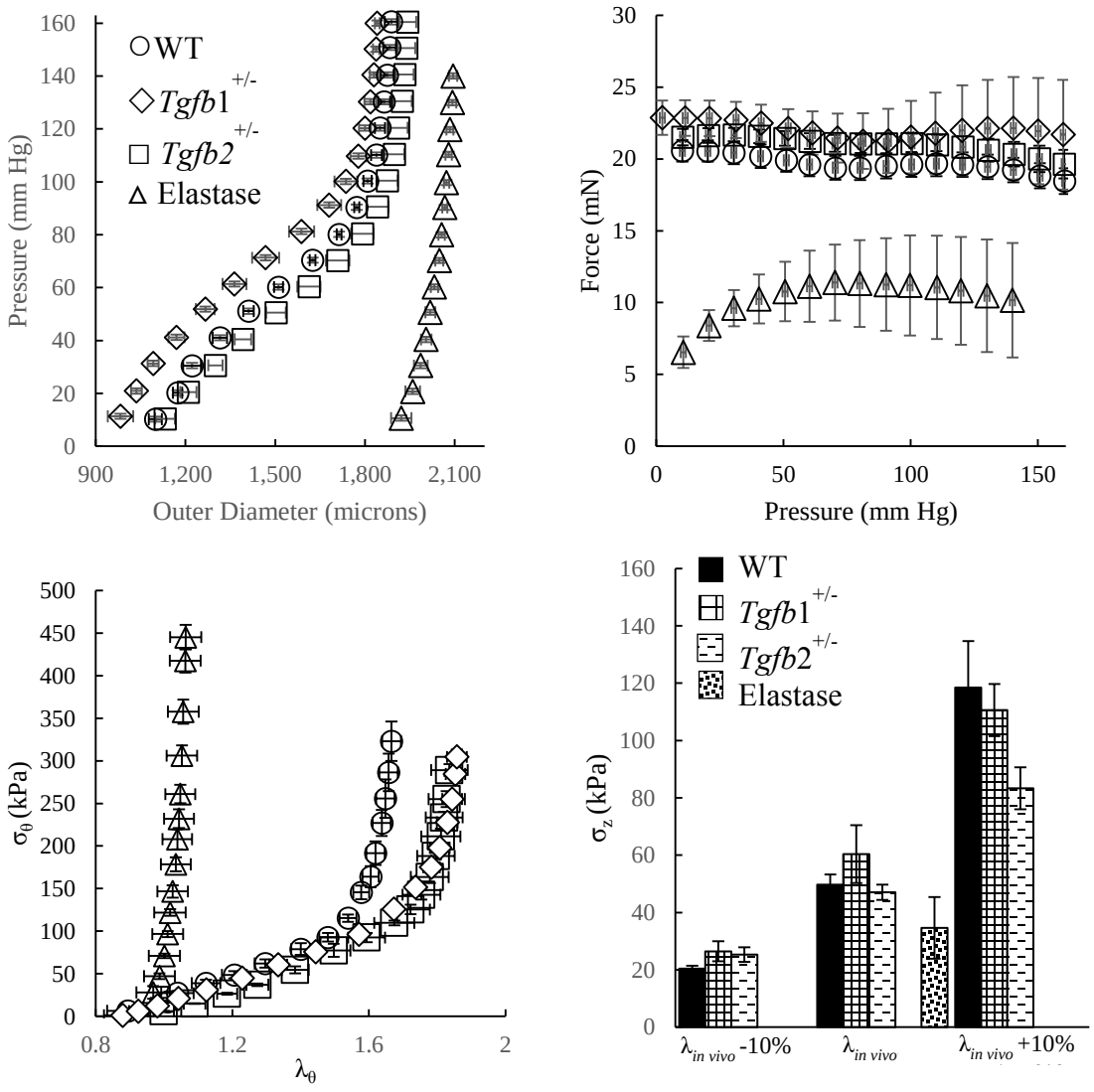

Figure 3.3: Biaxial Mechanics from the Ascending Thoracic Aorta (ATA) from wild-type (WT), *Tgfb1*$^{+/-}$, *Tgfb2*$^{+/-}$, and elastase mouse models.

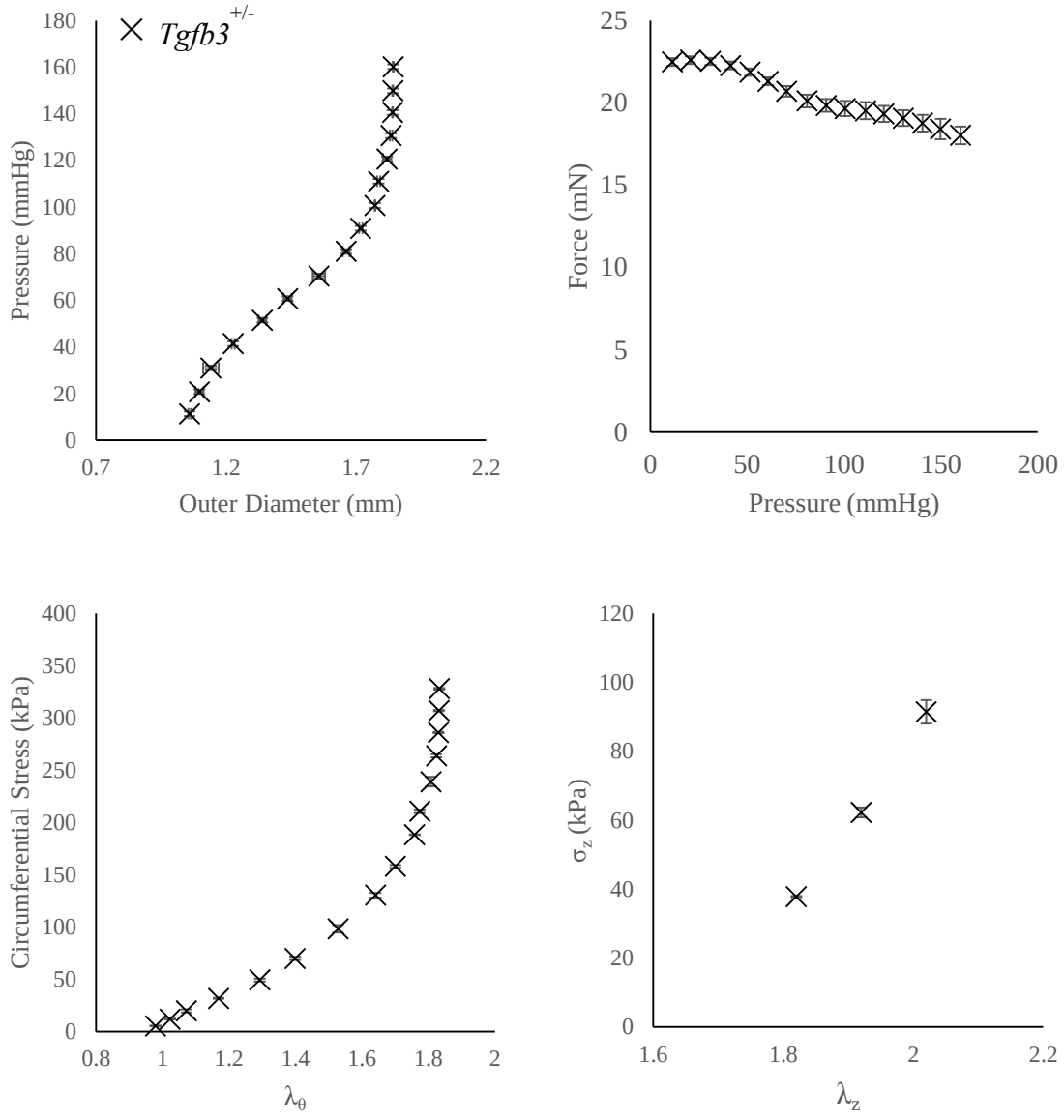

Figure 3.4**:** Biaxial Mechanics from the Ascending Thoracic Aorta (ATA) of a single *Tgfb3*$^{+/-}$ mouse (n=1).

CHAPTER 4

ACTIVE STRESS GENERATION IN THE ASCENDING AORTAS OF TGF BETA-LIGAND DEFICIENT MICE

4.1 ABSTRACT

Transforming growth factor-beta (TGFβ) and the associated signaling pathways form the genetic basis of the five types of the connective tissue disorder known as Loeys-Dietz Syndrome (LDS) (see also, Chapter 3). Collectively, LDS patients present with thoracic aortic dilation and are prone to sudden dissection and rupture. While it is apparent that the connective tissue, in particular the elastic network, is disrupted in LDS patients, vascular smooth muscle cell (SMC) dysfunction is also prevalent. The role of TGFβ signaling in SMC dysfunction, however, remains ambiguous, with confounding molecular findings. In this work, we assess SMC functionality through active stress generation measurements using wire myography across murine models of *Tgfb1*$^{+/-}$, *Tgfb2*$^{+/-}$, and *Tgfb3*$^{+/-}$ and age-matched wild-type controls to delineate specific TGFβ ligand loss-of-function manifestations in SMC contractility. Additionally, we compare the passive material responses under uniaxial extension to provide an assessment of extracellular matrix stiffness. Our findings revealed that *Tgfb2*$^{+/-}$ mice showed a significantly reduced (hypocontractile) capacity for active stress generation (*Tgfb2*$^{+\backslash-}$ = 35.8 ± 16.7 kPa; *Tgfb2*$^{+\backslash+}$ = 65.6 ± 15.7 kPa) while *Tgfb3*$^{+/-}$ mice were capable of increased (hypercontractile) active stress generation (*Tgfb3*$^{+\backslash-}$ = 158.2 ± 12.1 kPa; *Tgfb3*$^{+\backslash+}$ = 77.3 ± 13.0 kPa). Although trending towards hypocontractile behavior, *Tgfb1*$^{+/-}$ vessels showed no statistically significant differences in contractility (*Tgfb1*$^{+\backslash-}$ = 45.4 ± 6.3 kPa; *Tgfb1*$^{+\backslash+}$ = 64.4 ± 21.45 kPa). Collectively, these data suggest that a loss-of-function in *Tgfb2* or *Tgfb3* results in altered SMC contractility, revealing that disruption of these two isoform signaling pathways may indicate a higher propensity towards aneurysm formation.

4.2 INTRODUCTION

The transforming growth factor-beta (TGFβ) family of cytokines (TGFβ-1,-2,-3) regulates diverse vascular cell functions that are essential to maintaining vascular homeostasis [107–109]. These functions include smooth muscle cell (SMC) phenotypic modulation, differentiation [110,111], and proliferation, as well as maintenance of the extracellular matrix environment [112]. Since Loeys-Dietz syndrome (LDS) patients present with aggressive and lethal aortopathies (aneurysm and dissection), the passive and active mechanical responses of these tissues are likely affected (see also Chapter 3). The active or contractile component represents the mechanical contributions of SMC to the total stress state of the tissue [113,114]. In healthy tissues, SMCs are the predominant cell-type in the medial layer, actively maintaining the properties of the arterial wall, and adapting to acute and chronic mechanical or chemical stimuli. These functions are achieved through contraction and/or relaxation, as well as the synthesis and/or degradation of structurally significant constituents [1]. In LDS, dysfunctional TGFβ signaling leads to aberrant SMCs, affecting the vasculature's innate adaptive responses to generate vascular tone and to regain passive mechanical homeostasis. These effects are compounded by the altered mechanical state of the tissue, resulting in physical cues that drive maladaptive remodeling processes. Moreover, fragmented elastin is a known chemoattractant, inflammatory agent, and chemokine that can induce actin polymerization in SMCs [115]. There exists a pressing need to elucidate the role of pathological TGFβ signaling in SMC dysfunction that may reveal crucial information on aneurysm pathogenesis and progression in LDS.

While SMC dysfunction is evident using immunobiological and molecular tools, gross functional changes in contractility on a vessel-level scale from altered TGFβ

signaling can be assessed more directly. In this work, we reveal the differential effects of *Tgfb1*, *Tgfb2,* and *Tgfb3* loss-of-function on SMC functionality through assessment of active stress generation using $Tgfb1^{+/-}$, $Tgfb2^{+/-}$, $Tgfb3^{+/-}$ murine models and their wild-type controls. This work is an extension of Chapter 3 and is meant to inform more complete genetic and molecular analysis being performed in collaboration with Dr. Azhar's lab at the University of South Carolina, School of Medicine.

4.3 METHODOLOGY

Following animal protocols approved through the Institutional Animal Use and Care Committee at University of South Carolina (see also Chapter 3), the ascending thoracic aorta (ATA) was isolated from $Tgfb1^{+\backslash-}$ (4 months, n=3), $Tgfb2^{+\backslash-}$ (9 months, n=4), and $Tgfb3^{+\backslash-}$ (4 months, n=3) mice and age-matched Wild-Type (WT) controls (i.e., $Tgfb1^{+\backslash+}$, n=3; $Tgfb2^{+\backslash+}$, n=4; $Tgfb3^{+\backslash+}$, n=3). Vessels were cut into ring segments and cleaned of perivascular tissue. The ages designated for this study were selected based on unpublished observations of the onset of dilation from ultrasound data (Dr. Azhar's lab, not shown). The ring segments were mounted to a M1000 Radnoti wire myograph using 50 μm wires and submerged in temperature-controlled Krebs Henseleit Buffer (KHB) (118 mM NaCl; 4.7 mM KCl; 1.2 mM $MgSO_4$; 1.25 mM $CaCl_2$; 25 mM $NaHCO_3$; 11 mM glucose) at 37°C while being continually gassed with carbogen (95% O2, 5% CO2) (Figure 4.1). Rings were allowed to equilibrate for 30 minutes in the gassed-KHB solution, at which time they underwent three uniaxial preconditioning cycles including cyclical stretching to physiological levels of roughly $\lambda = 1.8$. To initiate SMC contraction, the KHB was refreshed and supplemented with 10^{-4} M phenylephrine, and then uniaxial extension was performed at 200 μm steps with 3-minute equilibration periods at each step.

Throughout extension testing, the force and length were recorded in real-time using the embedded myograph hardware and Axiocam 105 CMOS camera on a Zeiss Stemi 305 dissecting scope. The mechanical testing results generated with phenylephrine stimulation are denoted as the "total" mechanical response of the arterial ring representing a summation of the passive and active responses [114]. Subsequently, the KHB was refreshed and supplemented with 10^{-4} M sodium nitroprusside to stimulate SMC relaxation. The rings then underwent an identical uniaxial extension protocol to collect the response of the ECM, denoted as the "passive" mechanical state of the arterial ring. Then the ring sectors were removed, cut, and imaged to measure cross-sectional area. From this data, the 1-D Cauchy stress and stretch ratios were calculated using [116],

$$\sigma = \frac{F\lambda}{2HD}, \ \lambda = \frac{l + 2\pi a}{L + 2\pi a} \tag{3.4}$$

where H and D denote the undeformed thickness and width respectively; and L and l the undeformed and deformed distances between the wires, and a the radius of the wires. Active stresses were then calculated by subtracting the passive from the total response at common stretch ratios. The maximum active stress was found as the peak of the calculated active stress curve with the peak active stretch ratio occurring at this point (cf., Figure 4.3A), and denoted as the "optimal stretch ratio." To capture the simple passive mechanical behavior of the nonlinear stress-stretch curve, a tangential modulus was calculated as the slope around a stretch ratio of $\lambda = 1.8$ during the passive loading cycle.

Statistical analysis was performed using a one-way analysis of variance (ANOVA) single-factor analysis between heterozygous mice and wild-type counterparts and between each heterozygous group. P-values ≤ 0.05 were denoted with * and p-values ≤ 0.001 denoted with **.

4.4 RESULTS

Morphological assessment of the arterial rings revealed an increase in the undeformed cross-sectional areas between wild-types and *Tgfb2*$^{+\backslash-}$ mice (*Tgfb2*$^{+\backslash-}$ = 0.591 ± 0.19 mm^2, *Tgfb2*$^{+\backslash+}$ = 0.431 ± 0.20 mm^2; p-val = 0.04) while *Tgfb1*$^{+\backslash-}$ and *Tgfb3*$^{+\backslash-}$ showed no statistically significant differences in cross-sectional area (Figure 4.2 & Figure 4.3D). *Tgfb2*$^{+/-}$ mice showed a significantly reduced capacity for peak active stress generation compared to wild-type controls (*Tgfb2*$^{+\backslash-}$ = 35.8 ± 16.7 kPa; *Tgfb2*$^{+\backslash+}$ = 65.6 ± 15.7 kPa) while *Tgfb3*$^{+/-}$ were hypercontractile (*Tgfb3*$^{+\backslash-}$ = 158.2 ± 12.1 kPa; *Tgfb3*$^{+\backslash+}$ = 77.3 ± 13.0 kPa). *Tgfb1*$^{+/-}$ on the other hand, trended towards hypocontractility but did not reach statistical significance (*Tgfb1*$^{+\backslash-}$ = 45.4 ± 6.3 kPa; *Tgfb1*$^{+\backslash+}$ = 64.4 ± 21.45 kPa; p-val = 0.19) (Figure 4.3B). The stretch at which maximal active stresses were observed was also markedly decreased in *Tgfb2*$^{+/-}$ (1.76 ± 0.062) mice compared to *Tgfb2*$^{+/+}$ (1.98 ± 0.02) counterparts. The passive tangential modulus measured at an axial stretch of $\lambda = 1.8$ showed no statistically significant difference between each genotype and their respective age-matched WT mice. *Tgfb2*$^{+/-}$ mice however, trended towards increased stiffness with higher variation amongst samples (*Tgfb2*$^{+\backslash-}$ = 731.52 ± 453.6 kPa, *Tgfb2*$^{+/+}$ = 350.712 ± 134.7 kPa).

4.5 DISCUSSION

Active and passive stresses as well as stretch ratios were chosen as a metrics of comparison rather than force and length to account for differences in cross-sectional areas that may be present in these tissues. This is especially important given that the aneurysmal vessels are expected to be both thin and dilated, based on LDS characteristics. Previous research has shown that mutation of TGFBR2 in SMCs decreases contractile markers

[117], suggestive of reduced active stress generation *in vivo*. However, mutations in the TGFBR2 gene result in comprehensive TGFβ ligand signaling dysfunction and have also been shown to elicit compensatory signaling pathways [106], confounding the effects of specific TGFβ ligand isoforms on SMC functionality and cellular activity in pathological processes. Thus, using TGFβ ligand-specific loss-of-function heterozygous murine models, $Tgfb1^{+/-}$, $Tgfb2^{+/-}$, and $Tgfb3^{+/-}$, we assess individually their macroscopic effects on aortic morphology and SMC functionality through the ability of mutant vessels to maintain vascular tone and generate active stresses. Notwithstanding the complex biological and compensatory signaling mechanisms present on the cellular level, it is evident that loss-of-function in specific TGFβ ligands promotes different SMC contractility states, as reflected in their ability to generate active stresses. From our findings, there is a clear reduction in SMC contractility in $Tgfb2^{+/-}$ mice, generating half the active stresses compared to wild-types. $Tgfb2^{+/-}$ aortas also showed reduced stretch ratios at which the maximum active stress was generated, indicating differences in the force-tension relationship of the SMCs. Additionally, loss-of-function of *Tgfb1* appears to show lower active stress generation, although this trend was not statistically significant with our sample sizes. On the contrary, loss of function in *Tgfb3* promotes hypercontractile states in SMCs. We are the first to report the vessel-level mechanical analysis for active stress generation for these specific TGFβ ligand loss-of-function heterozygous mice; however, the underlying molecular and biological information related to the complex compensatory physiological processes that are observed in dysfunctional TGFβ signaling disease states (e.g., LDS) still remains vague and complex. Further investigation is needed to link the molecular information to tissue-level mechanical responses.

4.6 ACKNOWLEDGEMENTS

We would like to thank John Johnson and Mrinmay Chakrabarti for their assistance in animal genotyping, care, and arterial dissections. We would also like to acknowledge Nazli Gharraee for her help in establishing and troubleshooting the wire myography device and protocol. This work was supported through funding from the American Heart Association (17GRNT33650018)

4.7 TABLES

Table 4.1: Summary of wire-myography results across all *Tgfb* mice. Values are mean ± standard deviation. (*) denotes statistical significance between (+/-) and (+/+) while (^)denotes statistical significance between (+/-) models at $p < 0.1$ and $p < 0.05$ respectively.

	Tgfb1		*Tgfb2*		*Tgfb3*	
	+/- (n=3)	+/+ (n=3)	+/- (n=4)	+/+ (n=4)	+/- (n=3)	+/+ (n=3)
Max active stress (kPa)	45.4^ ± 6.3	64.1 ± 21.4	35.8^* ± 16.8	65.6 ± 15.7	158.2^* ± 12.1	77.30 ± 13.05
Cross-sectional Area (mm^2)	0.581 ± 0.07	0.510 ± 0.03	0.591* ± 0.19	0.431 ± 0.20	0.497 ± 0.12	0.481 ± 0.01
Optimal Stretch λ	2.05 ± 0.15	1.93 ± 0.17	1.775* ± 0.06	1.98 ± 0.03	2.25 ± 0.09	2.07 ± 0.05
Passive Tangential Modulus (kPa)	234.3 ± 52.6	241.9 ± 20.6	731.5 ± 453.6	350.7 ± 134.7	284.0 ± 59.3	300.3 ± 45.9

4.8 FIGURES

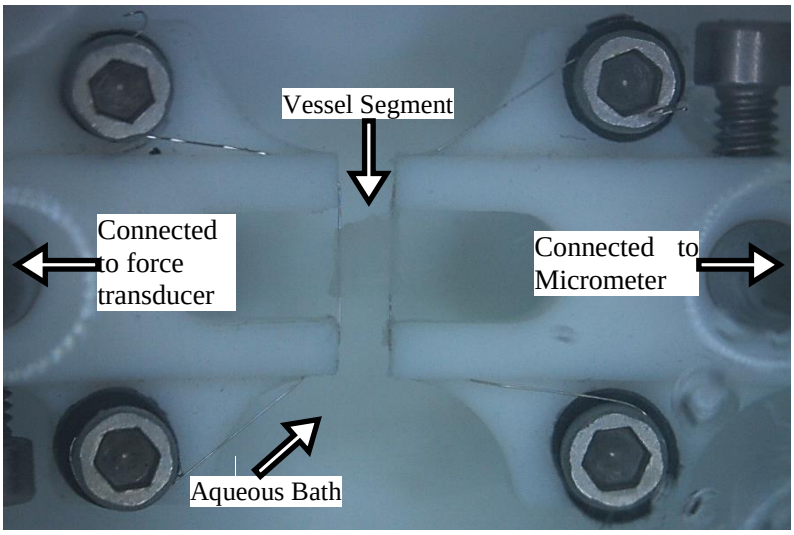

Figure 4.1: Overview of experimental set-up for thin wire myography experiments. Two wires are threaded intraluminally and secured to two control arms; one attached to a micrometer for axial extension and the other attached to a force transducer. Although difficult to see from the contrast of the tissue on the white background, the artery is mounted within an aqueous bath of KHB to maintain cell viability and to add vasoreactants.

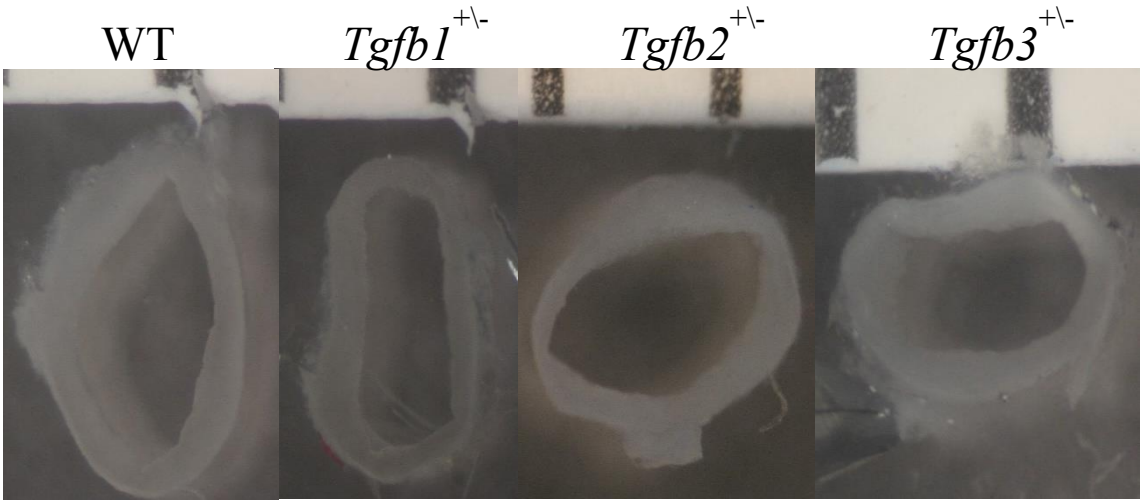

Figure 4.2: Ring Morphologies. Representative ring sector images from each strain of haploinsufficient mice and wild-type control

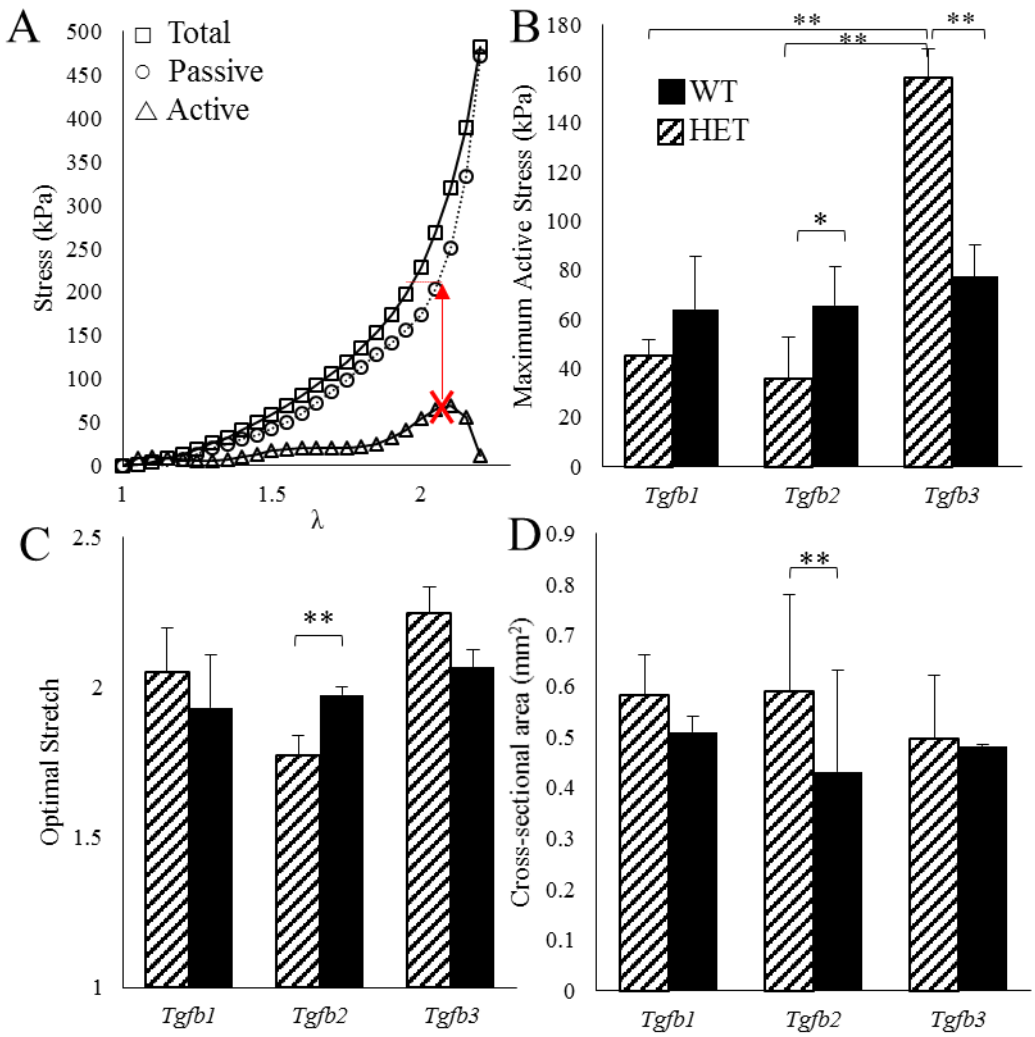

Figure 4.3: A. Representative data illustrating the calculation of the active responses from the total and passive conditions using wire-myography. B-D. Experiments for *Tgfb1*$^{+\backslash+}$, *Tgfb1*$^{+\backslash-}$, *Tgfb2*$^{+\backslash+}$, *Tgfb2*$^{+\backslash-}$, *Tgfb3*$^{+\backslash+}$, and *Tgfb3*$^{+\backslash-}$ mice, showing B. the maximum active stress generation, C. the optimal stretch ratio, and D. the cross-sectional area. (*) and (**) denotes statistical significance at $p < 0.1$ and $p < 0.05$ respectively.

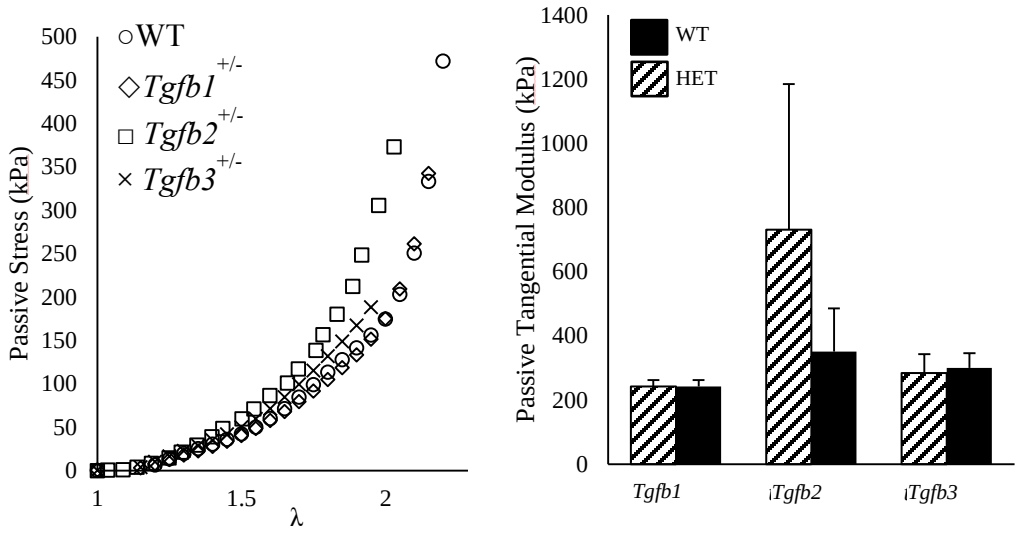

Figure 4.4: Representative passive mechanical characteristics for the *Tgfb1*$^{+\backslash-}$, *Tgfb2*$^{+\backslash-}$, *Tgfb3*$^{+\backslash-}$, and WT control mice. B. The tangential modulus measured at $\lambda = 1.8$ for each sample.

CHAPTER 5

NULL STRAIN ANALYSIS OF SUBMERGED ANEURYSM ANALOGUES USING A NOVEL 3D STEREOMICROSCOPY DEVICE[4]

[4]Lane B.A., Lessner S.M., Vyavahare N.R., Sutton M.A., Eberth J.F., In review for publication in *Computer Methods In Biomechanics and Biomedical Engineering (CMBBE)*

5.1 ABSTRACT

To measure the inhomogeneous 3D-strain fields present during inflation-extension testing of physiologically submerged micro-aneurysms, a Stereo Digital Image Correlation (StereoDIC) microscopy system is developed that revolves 15° stereo-angle cameras around a centrally-mounted target. Calibration is performed using submerged dot patterns and system accuracy verified using strain and deformation analyses for rigid body motions of speckle-patterned, micro-aneurysmal surrogates. In terms of the Green-Lagrange strain tensor and the 3D displacement fields, the results are stable even after 120 minutes, with maxima in both strain bias and strain standard deviation less than 2E-03 for all components, and micron-level displacement standard deviation.

5.2 INTRODUCTION

Aneurysms are a vascular pathology broadly characterized by a focal dilation of the arterial wall. The microstructure is considerably more complex than typical arterial specimens, containing heterogeneously distributed and often dysfunctional extracellular matrix, thrombotic and necrotic material, altered contractility, and inflammatory cell infiltration resulting in dilated, complex, and often asymmetric geometries [118,119], leading to spatially inhomogeneous strain fields present during inflation and extension experiments that cannot be studied effectively using conventional techniques [120]. For example, commonly utilized biaxial mechanical (i.e., pressure-diameter, force-length) analyses fail to capture the complex material responses associated with large degree of heterogeneity within these samples, especially for small mouse aortic and human cerebral vessels. [45,105]. Thus, there is a clear impetus for applying experimental methods that enable measurements of localized deformations at this scale.

One such technique is stereo-Digital Image Correlation (StereoDIC), a non-contact optical imaging approach enabling measurements of 3D shapes and local deformations. Developed in the 1990s by one of the authors [121,122], the StereoDIC method, originally known as 3D-DIC, was extended to the microscale via imaging by optical microscopes in 2004 [123]. In recent years, StereoDIC has been used by us and others for the measurement of complex strain fields in diverse blood vessels [54,124–126]. Briefly, SteroDIC utilizes two cameras oriented at different perspectives to view common regions of a uniquely speckle-patterned sample. The camera system is calibrated to determine optical and geometric parameters used to map 3D world coordinate points into 2D sensor coordinates [55]. Corresponding features or areas on the target are observed simultaneously by both cameras and are then pixel-matched and reconstructed into 3D shapes. The patterns can then be tracked for local strain measurements [55].

Despite the apparent advantages of using StereoDIC, there are numerous obstacles towards its practical implementation for micro-aneurysms. First, soft-tissues require an aqueous environment to maintain hydration and are often submerged in physiological solutions, for example to test active smooth muscle contractility through assorted vasoreactants [11,114]. Hydration also influences material stiffness, viscoelasticity, and material failure [127]. Unfortunately this requirement creates material interfaces that cause optical distortion due to light refraction and these distortions lead to systematic imaging bias [125,128,129]. Secondly, since many aneurysm studies exploit murine models of vascular disease appropriate optical magnification and speckle pattern size must be used to capture displacements that are on the order of microns [105,130]. Measuring these displacements requires high magnification, thus limiting the image depth-of-field and

further exacerbating the light distortion effects which can generate strain values without deformations. These so-called "pseudostrains" constitute inherent system errors (e.g., bias) and must be quantified and minimized *a priori* to ensure validity of measurements. In addition, previous studies by a co-author [131–133] have shown that slight time-varying changes in light intensity recorded by each pixel will introduce variability in both the displacements and strains obtained during image matching.

In this paper, we present our design and baseline validation results for a novel StereoDIC device used to gather full-field 360° information from submerged specimens of similar length scales to murine aortas or small human cerebral vessels. In a cost- and experimentally efficient-manner, we utilize two radially fixed stereo cameras on a motor-controlled rotational stage to gather images of a centrally located specimen submerged in an octagonal aqueous bath. Much like the function of modern x-ray computed tomography (CT) scanners, our imaging platform revolves around the specimen, thereby minimizing the camera and lens costs while reducing viscous and inertial effects. Here we calibrate the system and address the resultant errors that arise from the strain analysis of submerged rigid bodies subjected to translations and rotations. Designated as *null-strain analysis* for the remainder of the article, the experimental results for the rigid body motions include (a) temporal errors for fixed translation/rotation (b) errors originating from stereo-rig rotation, and (c) errors due to image analysis of both simple and complex shapes. Understanding these measurement errors are necessary to validate of the stereomicroscopy device for displacement and strain measurements of micro-aneurysms

5.3 METHODOLOGY

5.3.1 Device Fabrication & Specifications

An overview of our stereomicroscopy device configuration and a representative image of a speckle-patterned sample are shown in Figure 5.1. A custom machined polycarbonate rotation stage with a Pioneer Flywheel Ring Gear-M/T (FRG-152F) is mounted with a thrust bearing (McMaster-Carr; 60715K29) around an aluminum shaft for precise and smooth rotation of the camera system with minimal backlash. During calibration, grids are affixed to a shaft located at the center of the rotational stage. The shaft is threaded, allowing for the bath to be raised, locked in place, and sealed with an O-ring to facilitate exchange of imaging targets within the water-tight environment. During calibration, grids are affixed to the shaft but for translation studies, the specimen is mounted to an arm connected to a vertical axis micrometer. To drive the rotational stage, an integrated stepper motor, driver, controller, and driving gear (McMaster-Carr; 6627T24; 6325K33) used to move the rotational stage via LabView computer control, enabling 360° rotation while collecting images at 45° intervals. The rotation intervals are selected to maintain consistent small angles between each camera's optical axis and the normal to each side of the octagonal polycarbonate specimen bath. A complete rotation with stepwise image acquisition occurs in less than 10 seconds.

Two CMOS cameras (EO-1312M) with VZM 200i Zoom Imaging Lenses capable of 0.5-2X zoom (Edmund Optics; #37-553 and #54-715) were mounted on a 3-axis translation stage (Thorlabs; PT3) positioned on a radial line from the center of the specimen stage. The stereo-rig mounting hardware contains dual stereo angle adjustment screws and a locking mechanism to prevent unintentional shifting. The cameras were fixed at

individual pan angles 7°-8° above and below the normal plane, providing a stereo angle (φ) of ~15°. This stereo angle has been shown to enable adequate sensitivity to out-of-plane motion while maintaining minimal perspective differences between imaging subsets [55]. Moreover the small angle reduces refraction-related image distortions so that image correction algorithms that minimize errors in the image-based displacement and strain measurements can be implemented in the commercial VIC-3D software [134].

5.3.2 System Calibration

Four glass microscope calibration grid targets (Correlated Solutions, Inc.; CSI-016-D12) with 15 x 15 pitch and edge dimensions of 1.595 x 1.595, 2.465 x 2.465, 4.060 x 4.060, and 6.380 x 6.380 mm. respectively, are placed within a custom-fabricated slide holder and mounted to a rigid luer-lock fitting. The luer-lock enabled smooth interchange of both the calibration grids and specimens, and eventually will be used as a port for tissue perfusion and inflation. The bath was then raised into position and filled with phosphate buffered saline (PBS). Next, the camera magnification was adjusted for the appropriately-sized grid, based on the anticipated specimen size that occupies the maximum image field. Approximately 40 images of the calibration target are collected while it undergoes arbitrary in-plane and out-of-plane manipulations. An overview of the calibration grid, holder, and representative images are shown in Figure 5.2. From there, images were imported into VIC-3D Version 8 and used to determine internal and extrinsic camera parameters using a Variable Ray Origin (VRO) 4^{th} order camera system model to correct for the effects of image refraction and high magnifications [134]. Unlike the traditional pinhole camera model that employs a single point at which all camera light rays originate, our application allows for light rays to pass through refractive surfaces between the camera and specimen.

Thus, the VRO model permits the origin of the camera to vary from pixel to pixel to help reduce measurement bias. In particular, each ray is defined by two points, one at the sensor plane and the other in a plane parallel to the sensor plane at a distance equal to the focal length. The second point (ray origin) is then modeled as a function of pixel location using multiple polynomial functions. Calibration of this camera model based on distortion-corrected locations of the grid pattern is conducted with the traditional bundle adjustment method [55]. Then, due to the nominally fixed radial position of the cameras relative to the center of the specimen, the system is calibrated at a single rotational view.

5.3.3 Speckle Patterning

DIC measurements require a sufficiently dense and random speckle-patterned surface with high background contrast to minimize measurement errors [135]. Patterns must be appropriate in size, be firmly attached to the surface, and deform with loading [136]. A mean speckle size should be on the order of 3-7 pixels in each direction for a 35 x 35 $pixel^2$ subset size to ensure accurate matching with optimal spatial resolution; larger speckles can be used with large subsets resulting in reduced spatial resolution [137]. In this work, speckle patterns are created through atomization using a commercially available airbrush with a 0.3 mm diameter full-cone nozzle. High-velocity air atomization reduces the size of the liquid jet into smaller and randomly dispersed droplets. A uniform application of white India ink (Staples) was first applied generously to the specimen at close range and then black India ink splattering at a distance of 30-40 cm is used to generate random patterns with the appropriate distribution of speckle sizes. Subset sizes of 47 x 47 pixels for the straight needle and 35 x 35 pixels for the fusiform and saccular aneurysm analogues correspond to specimen areas of approximately 380 μm^2 each.

5.3.4 Shape Reconstruction

Consistent with best practices for reporting DIC data [138], Table 5.1 provides a list of parameters used to extract deformation and shape data from the stereo images acquired from our patterned samples. An overview of the VIC-3D 8 work-flow can be seen in Figure 5.3. The commercial software VIC-3D 8 uses global coordinate information (X,Y,Z) and calibrated camera model parameters for template or pattern matching across subsets to correlate subsets in pixel (sensor) coordinates, converting these matching pixel locations into camera coordinates (x, y, z) [55]. The camera coordinate system origin is defined as the center point between the two camera sensors shown in Figure 5.1B. For 360° reconstructions, subsets are identified on the specimen that span the overlapping surface area between adjacent angular positions and used to calculate the coordinate transformations between views within the camera coordinate system. The coordinate transformations between all eight views are used within VIC-3D to combine all data sets and obtain a continuous data set around the entire specimen.

5.3.5 Null Strain Analysis

Since the specimen undergoes only rigid body translation and/or rotation, StereoDIC analysis of the images should result in zero for all strains. Thus, for our study, a *null strain analysis* is performed to quantify both bias and random variability in the results immediately and up to 120 minutes after rigid body motion has been performed. An initial reference image of a speckle-patterned 18G (1.25mm), straight needle was collected, and subsequent images at the same view were recorded after 10, 30, and 120 minutes to investigate temporal stability. For each measurement, the stereo-rig was then rotated about the specimen to gather the full 360° reference state. Without any movement of the needle,

the stereo-rig rotation is repeated, and the newly acquired images are used with previous sets to determine possible measurement errors introduced during the imaging and image analysis process. At this point, the needle undergoes rigid body translation of roughly 1 mm in the vertical direction using a micrometer. The stereo-rig again is rotated about the specimen to gather a full 360° view. These images are then analyzed with either of the previous image sets to determine the errors associated with rigid body translation. This process was repeated with the complex and asymmetric analogues to show the utility, applicability, and limitations of the stereomicroscopy device.

For all strain analyses, the surface displacements were used to calculate the local Green-Lagrangian strains formulated as [127]:

$$E_{xx} = \frac{\partial u}{\partial x} + \frac{1}{2}\left[\left(\frac{\partial u}{\partial x}\right)^2 + \left(\frac{\partial v}{\partial x}\right)^2 + \left(\frac{\partial w}{\partial x}\right)^2\right]$$
$$E_{yy} = \frac{\partial v}{\partial y} + \frac{1}{2}\left[\left(\frac{\partial u}{\partial y}\right)^2 + \left(\frac{\partial v}{\partial y}\right)^2 + \left(\frac{\partial w}{\partial y}\right)^2\right] \tag{5.1}$$
$$E_{xy} = \frac{1}{2}\left(\frac{\partial u}{\partial y} + \frac{\partial v}{\partial x}\right) + \frac{1}{2}\left(\frac{\partial u}{\partial x}\frac{\partial u}{\partial y} + \frac{\partial v}{\partial x}\frac{\partial v}{\partial y} + \frac{\partial w}{\partial x}\frac{\partial w}{\partial y}\right)$$

where (u,v,w) are the displacements originally measured relative to (X,Y,Z), the global world coordinate system. However, (x,y,z) in Eq (5.1) are local coordinates based on a local tangent plane for each point on the specimen surface where strains are obtained. For a cylindrical specimen, x corresponds approximately to the θ direction around the specimen, y the vertical specimen axis, and z the normal or radial direction on the surface. Here, the step size in Table 4.1 defines the number of pixels each subset is shifted in the x- and y-directions to generate the next data point. As shown in Table 4.1, a 5 x 5 set of local displacement data is used as a strain filter to reduce noise in each mesh subdomain. To

combine data obtained from each rotation of the stereo-rig, the authors used stitching options within the software to integrate overlapping data sets and obtain a full 360° reconstruction of the specimen.

5.4 RESULTS

5.4.1 Calibration and Shape Reconstruction

In- and out-of-plane motions of the calibration grids were restricted to approximately 25-30° due to depth-of-field lens limitations. Calibration with the VRO 4th order camera model yielded low average distances between theoretical and actual positions ranging between 0.022-0.042 pixels with extrinsic camera pan angle parameter φ =15.23° closely matched to physical measurements. Figure 5.4 demonstrates the ability of our stereomicroscopy system to reconstruct the three different shapes (straight needle, fusiform analogue, and saccular analogue) upon application of adequate speckle patterns. Further, the 45° imaging intervals provided enough image overlap to match subsets at different angular positions and to calculate coordinate transformations used to stitch the individual data sets together and reconstruct a 360° representation of the specimen shape. Inspection of Figure 5.4 shows that there is a small region in the reconstruction at the neck of the saccular-shaped analog where data is not available due to obscurance. Such regions are oftentimes deemed "blind spots" for the specific imaging system.

5.4.2 Null Strain Analysis

Temporal stability of the system over the course of 120 minutes resulted in small, spatially-averaged strain measurements E_{xx} = -1.98E-3 ± 2.36E-3, E_{yy} = -1.5E-4 ± 1.12E-3 E_{xy} = 7.2E-5 ± 1.3E-3 with the greatest deviation occurring in the *x*-direction. Comparable colormaps are shown in Figure 5.5 and summarized as box-and-whisker plots in Figure

5.6. Rotation of the stereo-rig yielded similar pseudostrain magnitudes E_{xx} = 9.6E-5 ± 2.5E-3; E_{yy} = 2.1E-5 ± 8.9E-4; E_{xy} = -1.2E-5 ± 1.5E-3, as shown in Figure 5.7. After imposing rigid body translations in the vertical direction, the standard deviations in vertical displacements were at the micron-level for all samples (*Needle:* -1.234 ± 0.002 mm; *Fusiform:* -0.653 ± 0.008 mm; *Saccular:* -0.553 ± 0.007 mm). Likewise, pseudostrains generated through rigid body translation are comparable to those introduced through stereo-rig rotation. This was true for all shapes analyzed and shown by the box-and-whisker plots in Figure 5.9 for each specimen type. Of note, the straight needle underwent a larger translation than the other two specimens and was imaged at a higher magnification.

5.5 DISCUSSION

To demonstrate our high magnification stereo-rig system's capacity for acquiring full 360° measurements from StereoDIC analysis of submerged micro-aneurysms, a series of rigid body motion studies have been performed successfully. For specimens ranging down to the millimeter scale, displacement standard deviations were on the order of a few microns and strain bias and variability less than 0.002. These bias and variability values are reasonable, given that the length and diameter of a healthy mouse abdominal aorta are around 5 mm and 1 mm, respectively, with aneurysmal aortas experiencing a 2.5-fold increase in diameter [41]. Although the stereomicroscopy device is limited by "blind spot" obscurance occurring at steep changes in contour (Figure 5.4C) due to distortion and inadequate image overlap in these regions, such errors could be rectified by using larger stereo angles and lower magnification, at the cost of decreased in-plane measurement sensitivity and spatial resolution. Furthermore, the analysis is performed adequately with only two off-the-shelf cameras and lenses, thereby reducing costs and eliminating the need

to fabricate custom mirrors or imaging lenses. An adequately sized speckle pattern for rigid specimens is achieved using conventional airbrushing techniques; however, precise control over airbrush-generated speckle size is currently limited. This limitation leads to larger speckles and reduced spatial resolution, causing certain subsets to have poorer image matching accuracy, especially when applied to the regions of high strains typical of soft tissues. Alternate techniques are being explored that provide precise, high contrast patterns and can reduce strain measurement errors in soft tissues [139,140].

In the case of pure translation of rigid bodies, Eq. 5.1 should be zero for all components. Thus, the strain measurements in Table 5.2 provides baseline estimates for the bias and variability that is expected when employing the system to obtain full field deformation data. Additional inspection of Table 5.2 shows that temporal effects are small but increased slightly over the course of 120 minutes. Although these sources are difficult to isolate, the results show that the combined effect of all external factors (i.e., changes in ambient lighting, India ink pattern degradation, laboratory temperature, camera mounting hardware, vibrations) has minimal impact on the quality of the data. Even compounded over time, these are extremely small errors compared to global soft-tissue strains [18,41,125]. Moreover, comparison of the measurements with and without rigid body motion shows that the effect of rotating the stereo-rig about the specimen only slightly increased the standard deviation of strain measurements (Table 5.2), further confirming the stability of the optical system for deformation measurements[5]. Careful inspection of the

[5] The relatively high magnification of the stereo-rig shown in Figure 4.1 has a limited depth-of-field. Although our studies were not specifically focused on this issue, the authors did observe an increase in error at higher magnifications and larger displacements, as shown in Table 4.2 for translation of the straight needle. The slight increase in errors is due to defocusing of the specimen near the periphery of the image resulting in poorer subset matching and increased measurement errors.

strain measurements in Table 5.2 shows that the circumferential strain E_{xx} has the largest bias and standard deviation. These results are consistent with expectations, since the local *x*-direction is perpendicular to the camera plane and has larger subset matching errors that propagate into the displacement measurements. Additionally, it is important to note that all analyses shown here were performed with a step size of 7, with strain values smoothed over 5 data points to provide a fine spatial resolution at the cost of increased noise and larger standard deviations. Although these filters can be adjusted to find the perfect balance, we used the highest spatial resolution to illustrate the upper bounds of the system capabilities. Thus, a local planar fit at this surface increases strain errors. Overall, the measured bias and variability in strain are comparable to previously published values using different devices fabricated for similar purposes [128].

The VRO model was chosen for this application over the traditional pinhole camera model to help reduce measurement bias through material interfaces. The traditional model employs a single point at which all camera light rays originate. However, when rays pass through refractive surfaces between the camera and specimen, as required for our application, the pinhole model is prone to larger errors in shape and deformation measurements. In contrast, the VRO model allows for the origin of the camera to vary from pixel to pixel to help reduce measurement bias and has been shown in this work to be well-suited for optical measurements through material interfaces necessary for tissue hydration.

Although the present work did not track the strains of soft tissues per se, we demonstrated the capacity of our device to track particles undergoing large rigid-body transformations. We show only small errors using our novel approach for implementing StereoDIC to gather full field information on simple and complex shapes while maintaining

complete specimen hydration throughout testing. The full utility of the stereomicroscopy device can lead to a broader understanding of the heterogeneous strain fields present within aneurysmal tissues under loading, These strain data can be used to help identify diverse and heterogeneous material properties through the selection of the appropriate constitutive models, for example by using the virtual fields methods [54,141,142]. Furthermore, the measured bias and variability in strains for our work are comparable to previously published values using different devices fabricated for similar purposes [128], providing confidence in the overall methodology for forthcoming soft tissue studies.

5.6 ACKNOWLEDGEMENTS

The authors would like to acknowledge the contributions of Dr. Hubert Shreier and Micah Simonsen of *Correlated Solutions Inc.* and those of Mike Gore and Liya Du for mechanical assembly and assistance with image optimization, respectively. This work was supported by the National Institutes of Health under grant number **(**R01HL133662) and by the National Science Foundation under grant number (CMMI 1760906).

5.7 TABLES

Table 5.1: Image Correlation & Software Analysis Parameters.

Parameters	
FOV (mm)	Fusiform & Saccular 13.3 x 10.6 Straight Needle 10.1 x 8.06
Camera Sensor Size	1280 x 1024 pixels
Sensing Area (mm)	6.79 x 5.43
Pixel Size (μm)	5.3 x 5.3
Subset Size ($pixels^2$)	Fusiform & Saccular 35 x 35 Straight Needle 47 x 47
Step Size/Subset Spacing (pixels)	7
Strain Filter (pixel)	5 x 5 with central Gaussian weighting
Lens Focal Length, Dry (mm)	90
Depth of Field (mm)	0.6 - 1.5
Software	VIC-3D Version 8

Table 5.2: Pseudostrain Error Analysis Summary.

	$E_{xx} \times 10^3$	$E_{yy} \times 10^3$	$E_{xy} \times 10^3$
Temporal Errors			
10 min	-0.27 ± 1.88	-0.11 ± 0.82	-0.09 ± 1.03
30 min	-0.70 ± 1.91	-0.062 ± 0.78	0.05 ± 1.12
120 min	-1.98 ± 2.36	-0.15 ± 1.12	0.07 ± 1.25
Camera Rotation Errors			
1 Revolution	-0.10 ± 2.57	0.02 ± 0.90	-0.01 ± 1.59
Rigid Body Motion Errors			
Straight Needle	-0.133 ± 3.12	-0.20 ± 2.02	-0.002 ± 1.91
Fusiform	0.168 ± 2.50	0.141 ± 3.01	0.168 ± 1.95
Saccular	0.107 ± 2.79	0.182 ± 3.11	0.020 ± 2.22

5.8 FIGURES

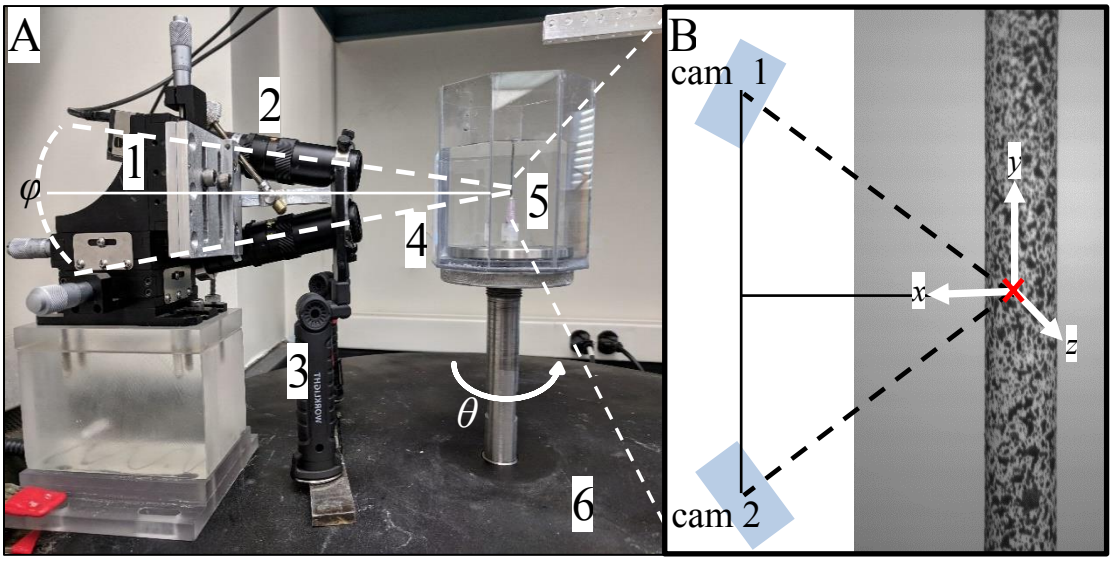

Figure 5.1: Experimental Setup A. Our custom-built, full-field, stereo-DIC device for submerged specimens includes: (1) a 3-axis camera micrometer stage, (2) a stereo-angle φ adjustable camera mount, (3) dual LED front light sources, (4) an octagonal media bath containing a (5) luer-lock specimen mount with perfusion port, and (6) a rotational angle θ controlled by a DC microstepper motor-driven stage and gear coupling (not shown). B. Camera coordinate system (*x,y,z)* with origin (×). The *x*-axis forms the baseline between the two cameras, the *z*-axis is orthogonal to this and constrained by the average plane between the two sensor planes, and the *y*-axis is orthogonal to these.

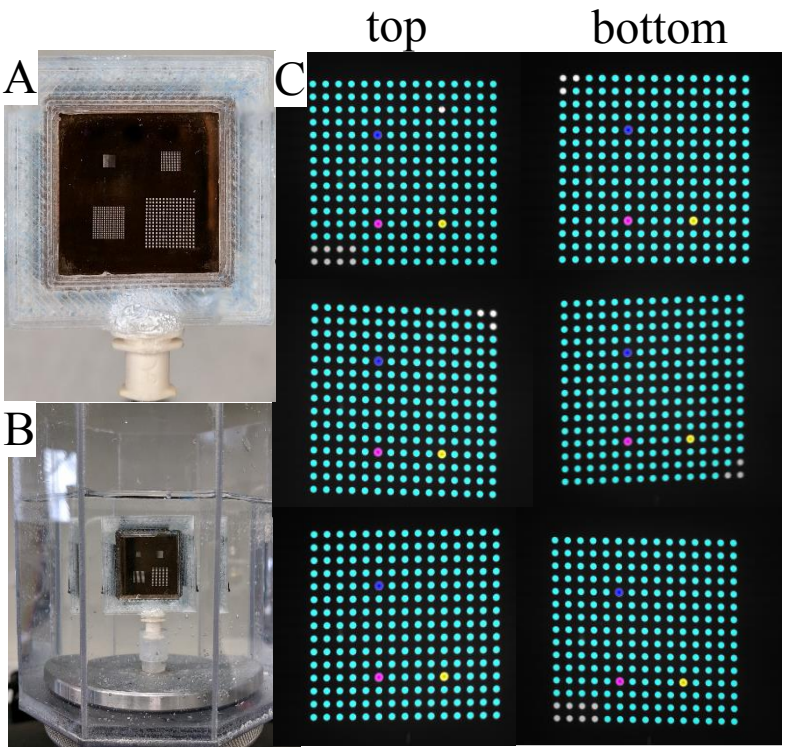

Figure 5.2: *A priori* calibration. A. Microscope calibration grid from *Correlated Solutions, Inc*. mounted to a custom-made luer-lock slide holder. B. The calibration grid is submerged in phosphate buffered saline within our octahedral bath. C. Examples of arbitrary rotations and translations of the glass slide used for calibration purposes.

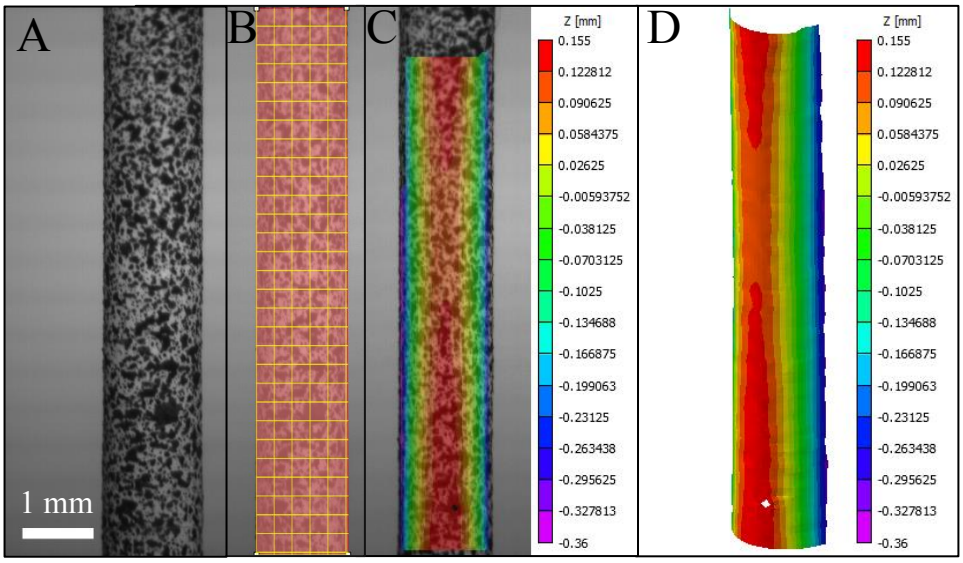

Figure 5.3: Digital image correlation analysis using VIC-3D 8. A. A representative image of the straight needle B. Region-of-interest and subset size (47x47) overlay projected onto the specimen C. Two-dimensional overlay of the camera coordinates in the z-direction and D. Resulting color contour of the *z* coordinate (i.e., depth of specimen)

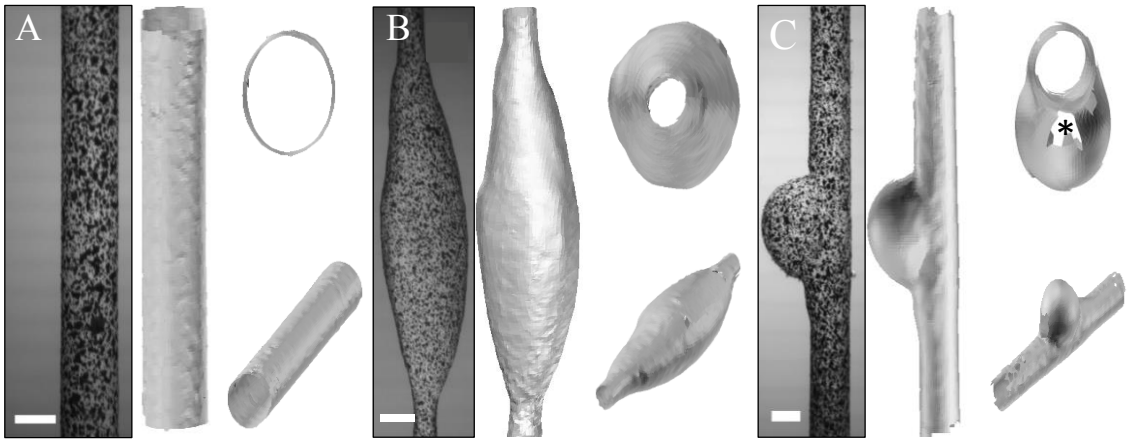

Figure 5.4: Rigid body reconstruction using sDIC for symmetric and asymmetric shapes. Images are gathered every 45° in our device under full hydration and are digitally reconstructed. Side, top, and isometric projections of A) a straight needle roughly the size of a mouse aorta, B) a fusiform-shaped aneurysm analog, and C) a saccular-shaped aneurysm analog. All scale bars are 1 mm. * indicates an area of insufficient surface reconstruction denoting a limitation or "blind-spot" obscurance in our system.

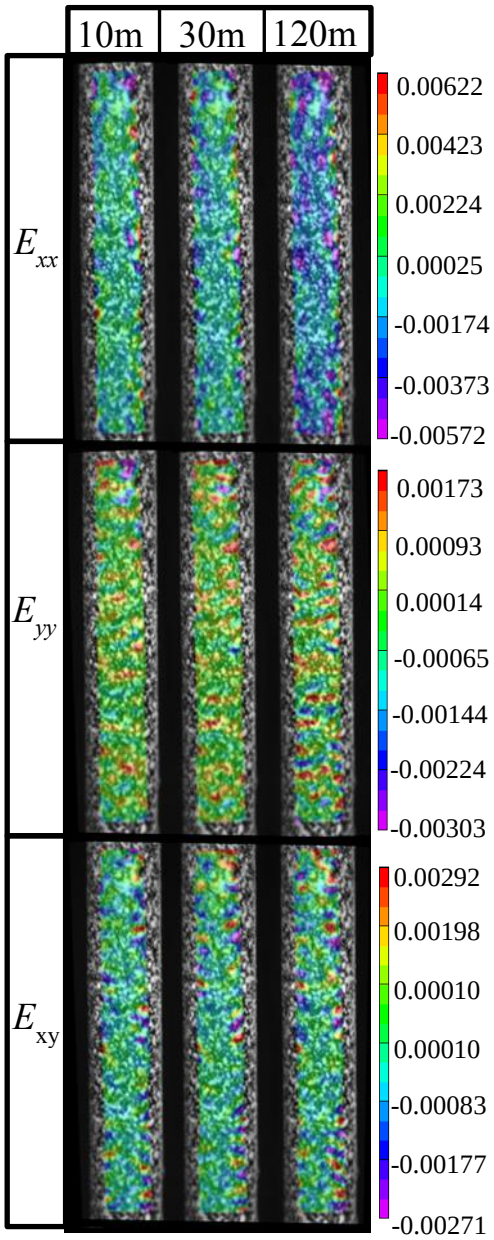

Figure 5.5: Temporal null strain analysis. Colormap of pseudostrains E_{xx}, E_{yy}, and E_{xy} of a speckle-patterned straight needle measured at 10, 30, and 120 minutes without rotation or translation to evaluate system stability over time.

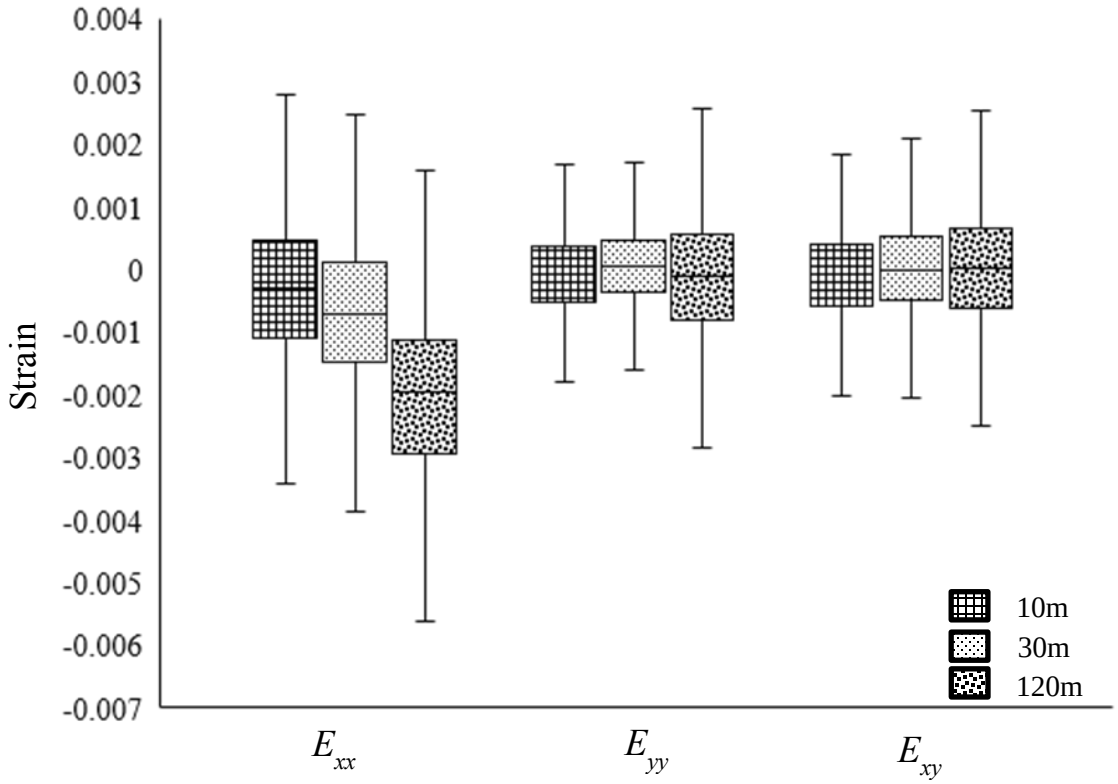

Figure 5.6: Temporal pseudostrain measurements. Box-and-whisker plots of resulting pseudostrain measurements at different timepoints showing median, upper quartile and lower quartile.

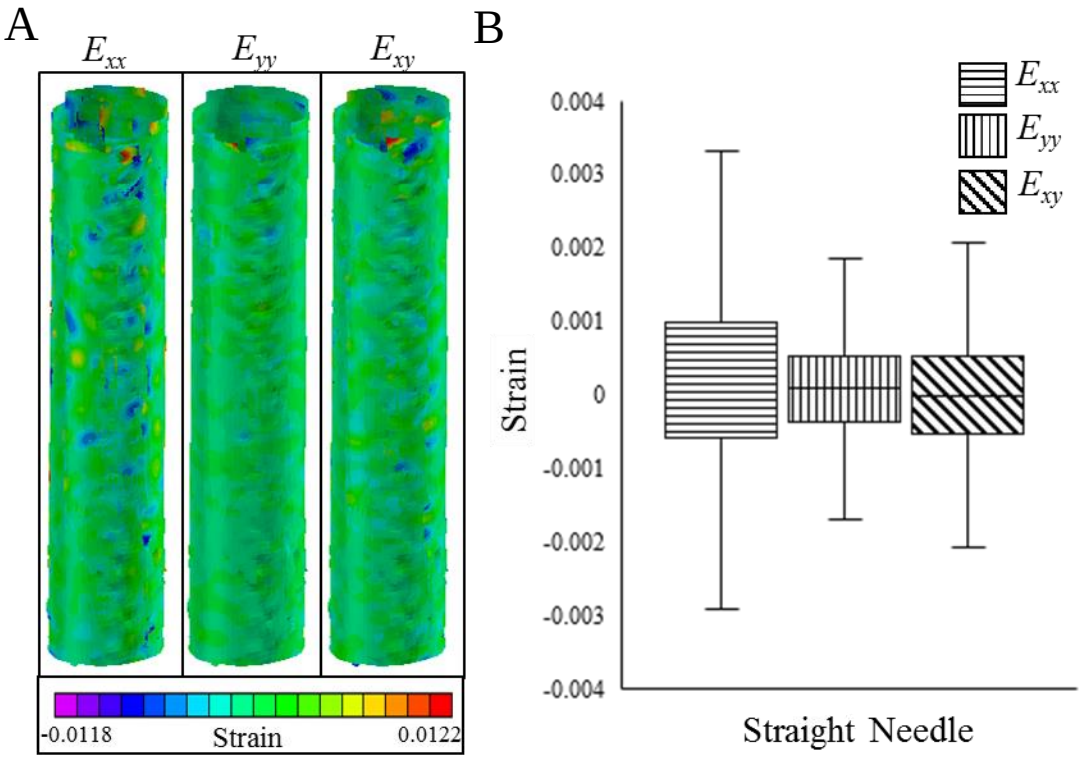

Figure 5.7: Null strain analysis for stereo-rig rotation. A) Colormap of pseudostrain measurements after rotation of the stereo-rig around the straight needle without rigid-body translation. Images are collected every 45° with each individual view stitched together to form one complete surface contour. B) Box-and-whisker plots show distribution of pseudostrains.

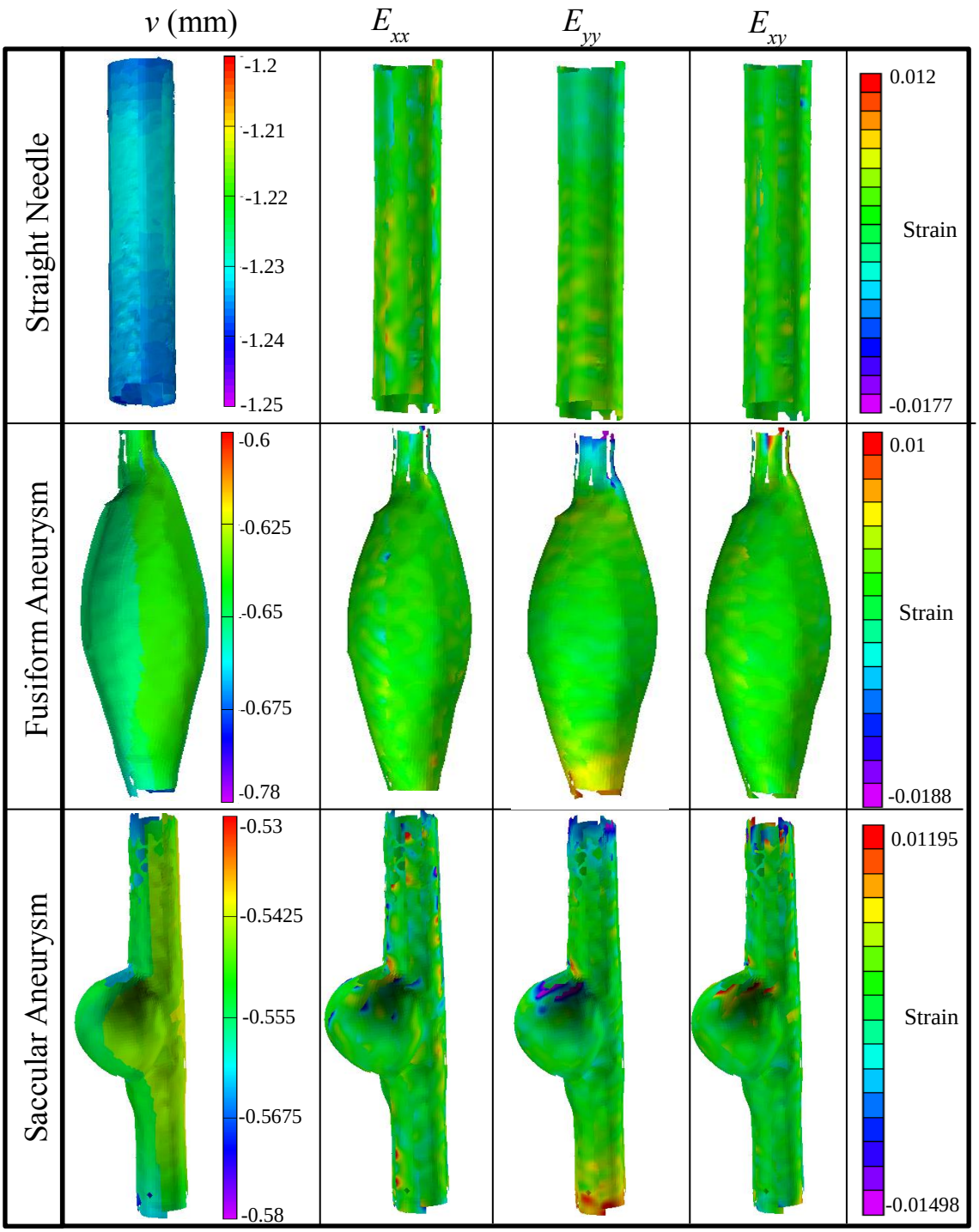

Figure 5.8: Rigid body motion null strain analysis. Colormaps of displacement and pseudostrain measurements after pure translation for three different shapes: (top) A straight needle roughly the size of a mouse aorta, (middle) a fusiform-shaped aneurysm analog, and (bottom) a saccular-shaped aneurysm analog.

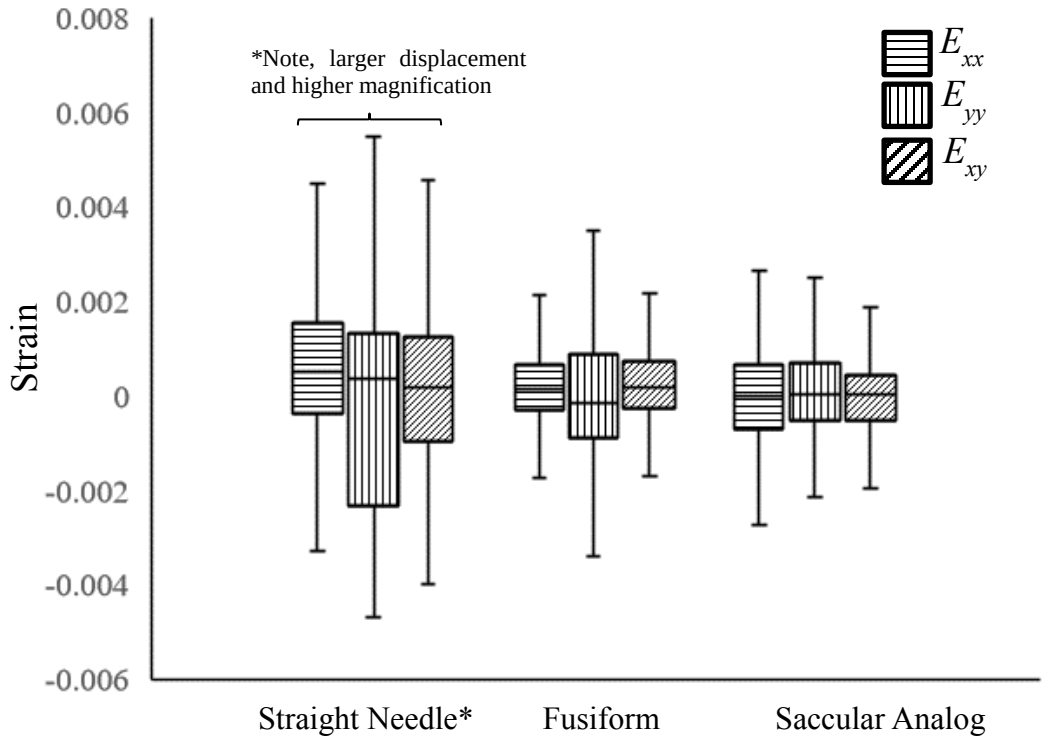

Figure 5.9: Rigid body motion null strain analysis box-plot. Box-and-whisker plot to show the distribution of pseudostrain measurements after rigid body translation of specimen.

CHAPTER 6

FULL-FIELD STEREO DIGITAL IMAGE CORRELATION STRAIN MEASUREMENT OF MURINE DESCENDING AORTA UNDER INFLATION-EXTENSION[6]

[6]Lane BA, Vyavahare NR, Lessner SM, Sutton MA, Eberth JF. To be submitted to *The Journal of Biomechanical Engineering*

6.1 ABSTRACT

In many aortopathies, asymmetrical mechanical loads and vascular cell dysfunction result in maladaptive remodeling with regional (local) microstructural changes that manifest as altered global mechanical properties. Routine experimental mechanical analyses, such as those gathered using echocardiology or simple biaxial testing, provide global metrics with a limited capacity to assess regional variations. Therefore, in this work, we demonstrate the implementation of a multi-axial murine artery stereo digital image correlation (StereoDIC) testing device for standard biaxial analyses and full-field strain measurements using the descending thoracic aorta. The device utilizes a single StereoDIC camera rig rotated about a centrally fixed specimen to acquire images at 45° intervals in both loaded and unloaded states while simultaneously measuring axial force and pressure. This approach enables both full-field localized strain measurements and standard biaxial analyses. After axial pre-stretching, strain measurements reveal a nearly principal and uniaxial deformation field in the *x*-, or circumferential, direction comparable to previously published full-field strain measurements (E_{xx} = 0.427 ± 0.127; E_{yy} = 0.062 ± 0.051; E_{xy} = 0.002 ± 0.046) at diastolic and systolic pressures. We also show distinct regional variations in strains in loaded states, suggested by the large standard deviation of the circumferential strain measurements and illustrated by the colormap. Therefore, we show our device has utility for future murine experimental aortopathic studies to evaluate regional microstructural changes in diseased states and their effects on arterial mechanics.

6.2 INTRODUCTION

Aortopathies encompass many vascular pathologies such as mural calcification, aortic aneurysm (AA), and dissection that result in maladaptive remodeling responses from

vascular smooth muscle cells to regain mechanical homeostasis, leading to localized changes in extracellular matrix (ECM) synthesis and degradation [9,15,30,115,143,144]. Microstructural changes in vascular ECM constituents impact regional material properties and contribute to vessel failure, hemorrhage, and significant morbidity. With the wide range of murine genetic, pharmacological, and surgical models available, there is a need for techniques capable of precise mechanical characterization of these evolving aortopathies that can lead to clinical translation [68,145–147]. Many standard experimental techniques rely on poor assumptions in order to provide global material metrics that adequately characterize nearly homogeneous and isotropic material responses; however, aortopathies often result in spatially heterogeneous and asymmetric tissues that undergo complex deformations under physiological loads. Therefore, there is a growing need to address experimental techniques used to evaluate advanced aortopathies to accurately capture realistic material responses that could elucidate novel features of vascular disease.

Of note, the non-contact optical imaging approach, Stereo-Digital Image Correlation (StereoDIC), enables full-field surface strain measurements of 3D objects through local deformation measurements. StereoDIC utilizes two cameras oriented at different perspectives to view common regions of uniquely speckle-patterned samples. The corresponding features on the specimen are observed simultaneously by both cameras and are then pixel-matched and reconstructed into 3D shapes. These patterns can then be tracked while the specimen is pressurized and extended in order to quantify local strain measurements [55]. StereoDIC has recently been used to measure the complex strain fields present is small and diverse blood vessels [54,124–126]. Although StereoDIC is advantageous for advanced mechanical characterization of diverse biomaterials,

implementation of full-field imaging of heterogeneous aortopathies in physiological media is experimentally challenging.

In this chapter, we apply our unique multi-axial murine artery inflation-extension testing device, described in the previous chapter, for full-field StereoDIC measurements of submerged murine arteries. Here we imprint a speckle pattern on the descending thoracic aorta (DTA) using an airbrush-based atomization technique, and the tissue is mounted within a physiological, aqueous bath. The artery is axially extended and pressurized per standard biaxial inflation-extension testing protocols while the stereo-rig rotates about the specimen at each loaded state, acquiring images at 45° intervals for 360° full-field strain analyses of the blood vessel under load. Thus, the full-field and standard biaxial mechanical characterization are both performed on the same tissue. Resultant strain fields at each angular position are transformed into a single contour plot for visualization.

6.3 METHODOLOGY

6.3.1 Device Fabrication

An overview of our multi-axial murine artery inflation-extension testing device to enable simultaneous full-field StereoDIC measurements is shown in Figure 6.1. The device is equipped with a syringe pump (AL-1000; World Precision Instruments) for static pressurization, a thin beam load cell force transducer (LCL-113G; Omega Engineering) to measure axial forces, a pressure transducer (PX409; Omega Engineering) for real-time pressure measurements, a control arm affixed to a 3-axis stage (PT3; Thorlabs) and a linear actuator (Z825B; Thorlabs) to orient and extend the specimen in the longitudinal direction. A custom machined polycarbonate rotation stage with a Pioneer Flywheel Ring Gear-M/T (FRG-152F) is mounted with a thrust bearing (60715K29; McMaster-Carr) around an

aluminum shaft for precise and smooth rotation of the camera system with minimal backlash. The shaft is threaded, allowing the bath to be raised, locked in place, and sealed with an O-ring to facilitate vertical mounting configuration of the specimen without interferences. An octagonal bath is utilized to provide planar interfaces between the camera optical axis and specimen at 45° intervals of the stereo-rig, avoiding complex optical distortions encountered at curved interfaces while providing enough imaging overlap to adequately reconstruct the specimen. An integrated stepper motor, driver, controller, and driving gear (6627T24; 6325K33; McMaster-Carr) are used to move the rotational stage. Two CMOS cameras (EO-1312M) with VZM 200i Zoom Imaging Lenses capable of 0.5-2X zoom (#37-553 and #54-715; Edmund Optics) were mounted on a 3-axis translation stage (PT3; Thorlabs) positioned on a radial line from the center of the specimen stage. The cameras were fixed at individual pan angles 7°-8° above and below the normal plane, providing a stereo angle (φ) of ~15° to ensure adequate sensitivity to out-of-plane motion while minimizing perspective differences between cameras [55]. Moreover, the small stereo angle reduces refraction-related image distortions, so that image correction algorithms can be implemented in the commercial VIC-3D software that minimize errors in the image-based displacement and strain measurements [134]. All components are integrated and controlled via a custom written LabView (National Instruments) script enabling real-time synchronized force, pressure, and image acquisition. This script facilitates the 360° rotation while acquiring images at 45° intervals of a specimen undergoing inflation-extension testing. A complete rotation with stepwise image acquisition occurs in less than 10 seconds.

6.3.2 Stereo-Digital Image Correlation System Calibration

Calibration of the system was performed as described in the previous chapter, and all images were imported into VIC-3D Version 8 using a Variable Ray Origin (VRO) 4th order camera system model at high magnifications [134] (See Chapter 5).

6.3.3 Specimen Preparation

A murine descending thoracic aorta (DTA) was isolated and cleaned of perivascular tissues through gentle dissection and branches were ligated using 10/0 nylon suture. The DTA was cannulated on blunted 26G needles, placed within a black India ink solution (Staples), and permitted to dry for 15 minutes to provide a black background on the specimen. The DTA was then rehydrated for 30 minutes in phosphate buffered saline (PBS), mounted within our device, extended to the measured *in vivo* axial stretch, and inflated to 100 mmHg. A pattern of white India ink (Staples) speckles was imprinted on the DTA while under load via atomization of a liquid jet into smaller droplets from a commercially available airbrush with 0.3 mm diameter full-cone nozzle. The airbrush was held approximately 30-40 cm away from the specimen to generate speckles on the entire specimen surface. The resulting pattern was then allowed to dry for 15 minutes prior to submersion again in PBS for 30 minutes for tissue rehydration prior to mechanical testing.

6.3.4 Standard Biaxial Testing

PBS was flushed through the vessel lumen and device tubing to remove bubbles. The artery then underwent five cycles of axial preconditioning from unloaded lengths to 10% above the estimated *in vivo* stretch ratio (0 to 20-50 mN), followed by five cycles of pressurization from 10-160 mmHg at the *in vivo* axial stretch ratio to minimize viscoelasticity (see also citation [11]). The *in vivo* axial stretch was measured *in vivo* prior

to excision, and it was also confirmed through a series of axial-force extension tests at fixed luminal pressures to identify the force-pressure invariant relationship.

For data acquisition, the artery was extended to three axial stretch ratios (*in vivo* ± 10%) and then underwent three pressurization cycles from 0-160 mmHg with simultaneous force, outer diameter, and pressure measurements at 10 mmHg increments. The stereo-rig was revolved around the specimen at each loaded state, acquiring images at 45° intervals. At the conclusion of testing, an intact ring segment of the artery was imaged to measure undeformed cross-sectional area *A*. Under the assumption of incompressibility, the deformed inner radius is calculated as:

$$r_i = \sqrt{r_o^2 - \frac{A}{\pi \lambda_z}} \tag{6.1}$$

The mean circumferential σ_θ and axial σ_z stresses are then calculated from the measured data using

$$\sigma_\theta = \frac{P r_i}{h} \text{ , and } \sigma_z = \frac{F}{\pi (r_0^2 - r_i^2)}, \tag{6.2}$$

Likewise, the mid-wall circumferential λ_θ and axial λ_z stretch ratios are calculated from

$$\lambda_\theta = \frac{(r_i + r_o)}{(R_i + R_o)} \text{ , and } \lambda_z = \frac{l}{L}, \tag{6.3}$$

where r_i and r_o are the deformed inner and outer radii, R_i and R_o are the unloaded inner and outer radii, and l and L are the deformed and undeformed vessel lengths, respectively.

6.3.5 Stereo-Digital Image Correlation

Images collected while testing are imported into VIC-3D 8 to define regions of interest and input subset size (55 x 55 pixels), providing subset tracking areas of approximately 390 μm^2. VIC-3D 8 uses transformed global coordinate information (X,Y,Z) and calibrated camera models for template matching between images, and camera projection lines to correlate subsets in pixel (sensor) coordinates. The software converts these matching pixel locations into camera coordinates (x, y, z) [55]. For full specimen reconstruction, subsets are identified on the specimen that span the overlapping surface area between adjacent angular positions and used to calculate the coordinate transformations between views within the camera coordinate system. The coordinate transformations between all eight views are used within VIC-3D to combine all data sets and to obtain a continuous data set around the entire specimen.

For all strain analyses, the surface displacements were used to calculate the local Green-Lagrangian strains [127]:

$$E_{xx} = \frac{\partial u}{\partial x} + \frac{1}{2}\left[\left(\frac{\partial u}{\partial x}\right)^2 + \left(\frac{\partial v}{\partial x}\right)^2 + \left(\frac{\partial w}{\partial x}\right)^2\right]$$
$$E_{yy} = \frac{\partial v}{\partial y} + \frac{1}{2}\left[\left(\frac{\partial u}{\partial y}\right)^2 + \left(\frac{\partial v}{\partial y}\right)^2 + \left(\frac{\partial w}{\partial y}\right)^2\right] \qquad (6.4)$$
$$E_{xy} = \frac{1}{2}\left(\frac{\partial u}{\partial y} + \frac{\partial v}{\partial x}\right) + \frac{1}{2}\left(\frac{\partial u}{\partial x}\frac{\partial u}{\partial y} + \frac{\partial v}{\partial x}\frac{\partial v}{\partial y} + \frac{\partial w}{\partial x}\frac{\partial w}{\partial y}\right)$$

where (u,v,w) are the displacements originally measured relative to (X,Y,Z), the global world coordinate system. However, (x,y,z) in Eq (6.4) are local coordinates based on a local tangent plane for each point on the specimen surface where strains are obtained. For a cylindrical specimen, x corresponds approximately to the θ direction around the specimen, y the vertical specimen axis, and z the normal or radial direction on the surface. Here, the

step size defines the number of pixels each subset is shifted in the *x*- and *y*- directions to generate the next data point. To reduce noise resulting from direct strain measurement in each mesh subdomain, a strain filter is used over 21 x 21 points for a virtual strain gauge size of 168 pixels (step size × # of points; $8 \times 21 = 168$). Consistent with best practices for reporting DIC data [138], Table 6.1 provides a list of parameters used to extract deformation and shape data from the stereo images.

6.4 RESULTS

System calibration with the VRO 4th order camera model yielded low residuals (0.062) between theoretical point locations and actual positions in images. Figure 6.2a shows representative images acquired at 45° increments of the murine DTA imprinted with the white speckle pattern. Upon image import and correlation in VIC-3D 8, the rigid transformations calculated between each adjacent view were used to transform individual angular views into a single 3D contour with minimal regions of interest lost on the specimen (Figure 6.2b). Standard biaxial mechanical analysis reveals the pressure-diameter, force-pressure, circumferential stress-stretch, and axial stress-stretch relationships of the DTA as shown in Figure 6.3. Biaxial analysis metrics indicate a midwall circumferential stretch ratio λ_θ of 1.49 at 120 mm Hg.

Stereo-DIC strain analysis shows the regional surface strain distributions of the DTA while undergoing inflation-extension tests at diastolic and systolic pressures in Figure 6.4. Note that regional strains in the *x*-, or circumferential, direction ($E_{xx} = 0.427 \pm 0.127$) are much larger in magnitude compared to those in the axial and shear directions ($E_{yy} = 0.062 \pm 0.051$; $E_{xy} = 0.002 \pm 0.046$), with strains calculated relative to a minimally pressurized but axially extended geometry. Strain measurements reveal, on average, a

nearly principal circumferential deformation field as expected in an artery extended and fixed at the *in vivo* length (see Figure 6.5; Table 6.1). Although direct comparison between the midwall stretch metric and surface strain measurements is difficult to interpret due to coordinate transformations and slightly different reference configurations, the spatially averaged circumferential strains measured herein are slightly lower than the global metric from biaxial analyses, once converted back to Cauchy strain metrics ($\lambda_\theta - 1 = 0.49$ vs $E_{xx} = 0.427 \pm 0.127$). The large standard deviation in strain measurements indicates inhomogeneous circumferential stretches in comparison to the global metric.

6.5 DISCUSSION

This work aims to validate our design for a cost-effective, multi-axial murine artery testing device for StereoDIC with the use of one stereo-camera rig rotated about a central physiologically submerged specimen for full-field strain measurement, in combination with a standard biaxial mechanical set-up. We have previously quantified the inherent system measurement bias ($E_{xx} \times 10^3 = -0.10 \pm 2.57$; $E_{yy} \times 10^3 = 0.02 \pm 0.90$; $E_{xy} \times 10^3 = -0.01 \pm 1.59$; see Chapter 5) and shown that this experimental approach incorporates minimal error in comparison to the expected magnitude of soft tissue deformations. Additionally, resultant strain magnitudes from our full-field StereoDIC analysis herein are reasonable and comparable with similar values reported in other studies, although performed on a different aortic region and with a slightly modified experimental configuration [128,148].

Although the utility of StereoDIC is evident for full-field measurements of murine arteries, there are notable practical limitations in patterning techniques. Previous work has investigated the use of different patterning techniques on murine arteries, but the reported

approaches require specialized optics and reagents, making cost-effective experimental implementation challenging [149], while airbrush patterning techniques are common and commercially viable for StereoDIC applications [126,135,136,148]. However, achieving ideal speckle sizes for optimal spatial resolution on specimens at the murine length-scale proves difficult. Indeed, ideal speckles should range between 3-7 pixels, equivalent to 20-50 microns at required magnifications [137], but the airbrush technique is limited in precision, resulting in 80-120 μm speckles which require larger subsets for appropriate correlation, thus reducing spatial resolution. For distal segments of the murine aorta such as the infrarenal region, unloaded specimens are only 400-700 microns in outer diameter; thus, speckles on the scale of ~100 μm cover a large vessel surface area, reducing speckle density for precise template tracking and strain measurements. Current research is ongoing to bolster effective speckle patterning techniques that can improve spatial resolution for more precise strain field measurements of submerged specimens [140].

Although slightly limited in spatial resolution, it is still evident from our findings that distinct regional variations in arterial deformation exist, possibly owing to vessel branches, diameter changes, and perivascular environment even in healthy tissues [2]. Standard biaxial mechanical analyses utilize macroscopic assessments and assumptions to describe global material responses that often neglect these regional variations. Thus, in aortopathies where regional heterogeneity is commonplace, macroscopic assessments lack the ability to accurately account for variation in material responses that may reveal regional mechanical manifestations of diseased states. However, this study was only performed on healthy tissue to validate the experimental approach and viability of baseline measurements prior to application in diseased states.

In conclusion, and in accordance with previous studies using techniques similar to StereoDIC, regional variations in strain fields are expected in many biomechanical experiments [148], yet are often overlooked through standardized biaxial mechanical tests. Thus, StereoDIC and other full-field measurement applications prove useful in experimental analysis of regional variations, especially in advanced aortopathies. Our device is capable of both standard biaxial inflation-extension testing and full field StereoDIC measurements, thereby enabling a comprehensive material response characterization that can be used with inverse and virtual field methods, to provide regional material characterization linked to underlying microstructural changes. These capabilities could provide insight on pathological progression and severity [54,124,141,142,150].

6.6 ACKNOWLEDGEMENTS

The authors would like to acknowledge the contributions of Dr. Hubert Shreier and Micah Simonsen of *Correlated Solutions Inc.* and those of Mike Gore for assistance with image optimization and mechanical assembly, respectively. The authors also thank Drs. Matt Bersi and Jacopo Ferruzzi for their advice on speckle-patterning techniques for soft tissues. This work was supported by the National Institutes of Health under grant number **(**R01HL133662) and by the National Science Foundation under grant number (CMMI 1760906).

6.7 TABLES

Table 6.1: Image correlation software parameters and strain measurement summary statistics

Parameters	
FOV (mm)	9.28 x 7.42 mm
Camera Sensor Size	1280 x 1024 pixels
Sensing Area (mm)	6.79 x 5.43
Pixel Size (μm)	5.3 x 5.3
Subset Size (pixels^2)	55 x 55
Step Size/Subset Spacing (pixels)	8
Strain Filter (pixel)	21 x 21 with central Gaussian weighting
Lens Focal Length, Dry (mm)	90
Depth of Field (mm)	0.6 - 1.5
Software	VIC-3D Version 8

Strain Measurements		
	80 mm Hg	120 mm Hg
E_{xx}	0.264 ± 0.127	0.427 ± 0.137
E_{yy}	0.027 ± 0.034	0.062 ± 0.051
E_{xy}	-0.008 ± 0.04	0.002 ± 0.046

6.8 FIGURES

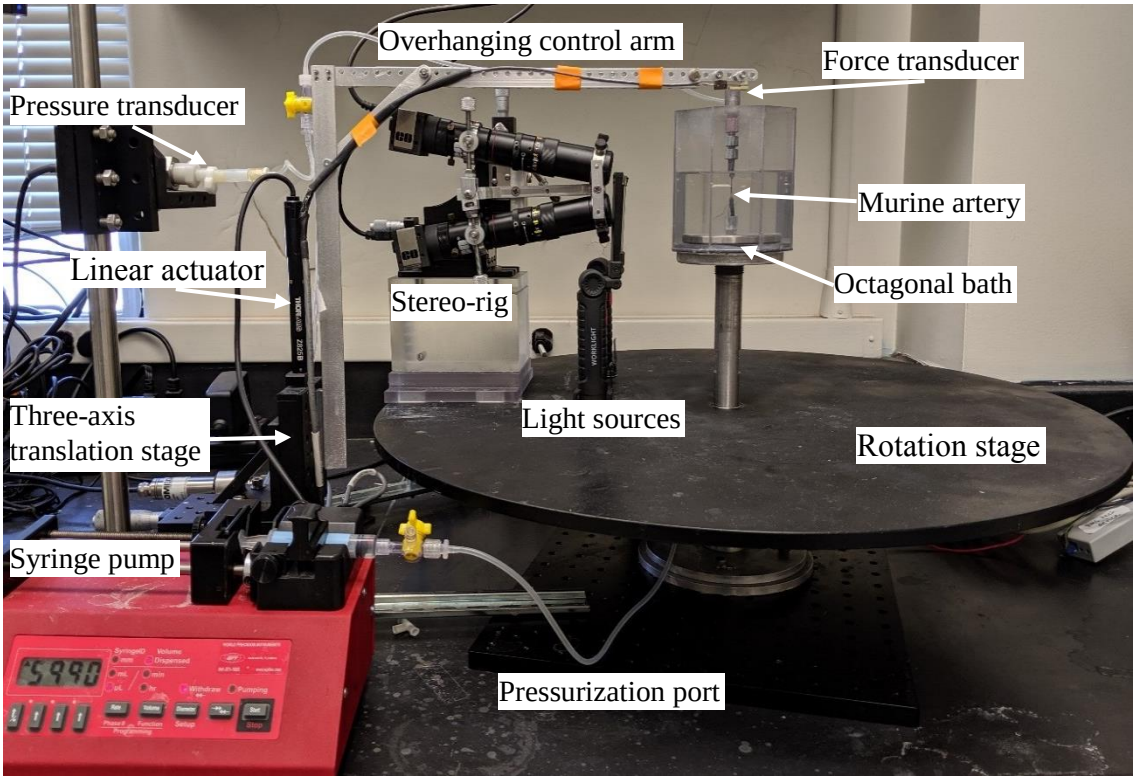

Figure 6.1: Multi-Axial Murine Artery Stereo-DIC Device Overview. Our unique multi-axial murine artery inflation-extension device with syringe pump, thin beam load cell force transducer, pressure transducer, and linear actuator is designed about a gear-driven rotation stage to permit stereo-rig rotation under loading for simultaneous Stereo-DIC measurements.

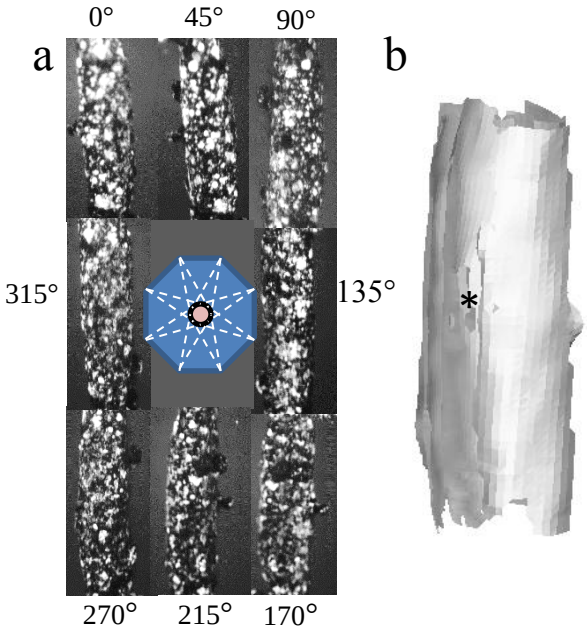

Figure 6.2: Three-dimensional Shape Reconstructions: (a) 360° Images of a speckle-patterned murine descending aorta (DTA) in the undeformed configuration and (b) the digital reconstruction of that shape using all 8 views. * indicates a poorly correlated region due to eclipse of speckle pattern by intercostal branch at unloaded state.

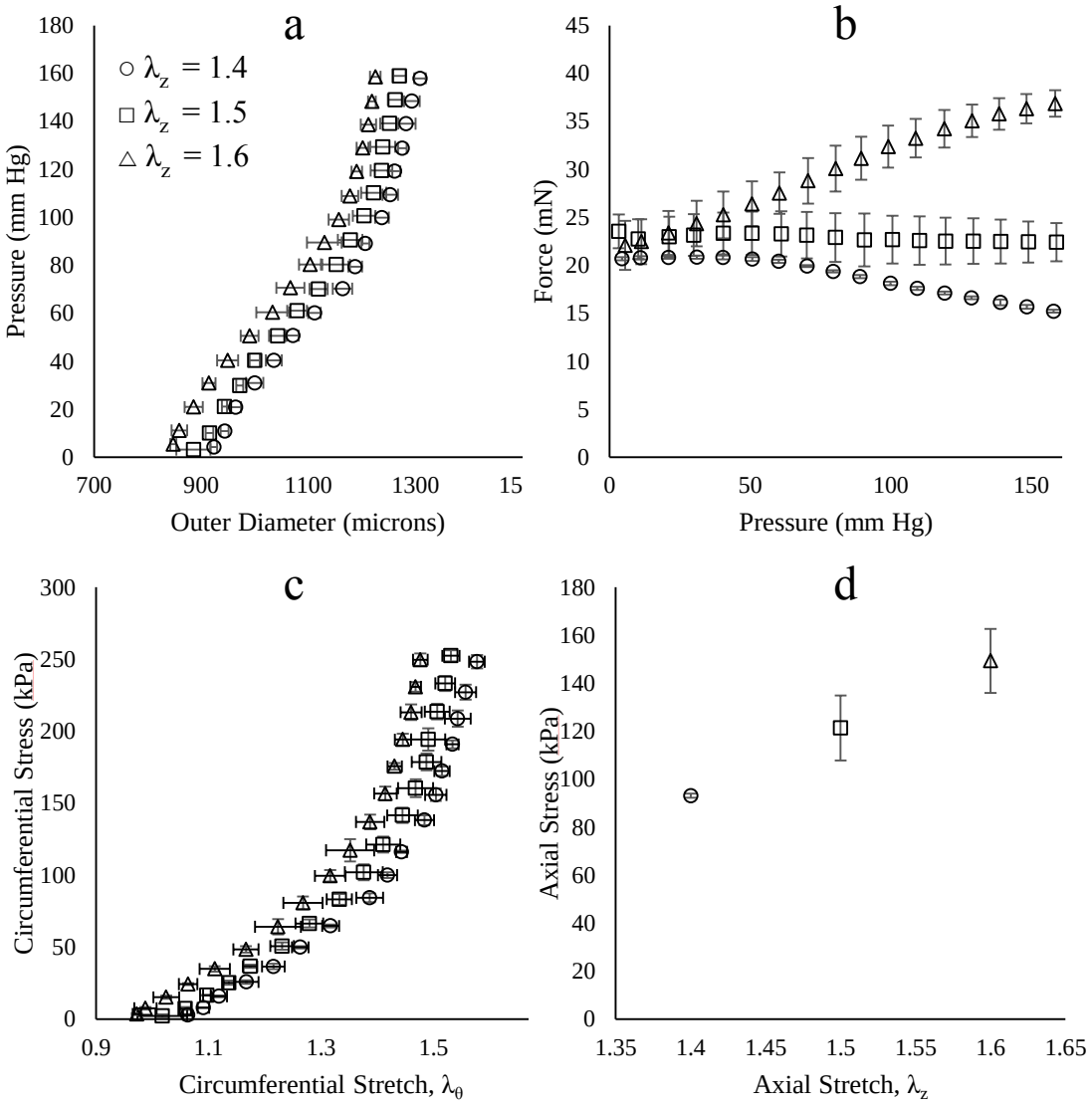

Figure 6.3: Standard Biaxial Mechanical Data for a Mouse Descending Aorta: (a) pressure-diameter, (b) force-pressure, (c) circumferential stress-stretch, and (d) axial stress-stretch material responses of murine descending artery. Data is mean ± standard deviation.

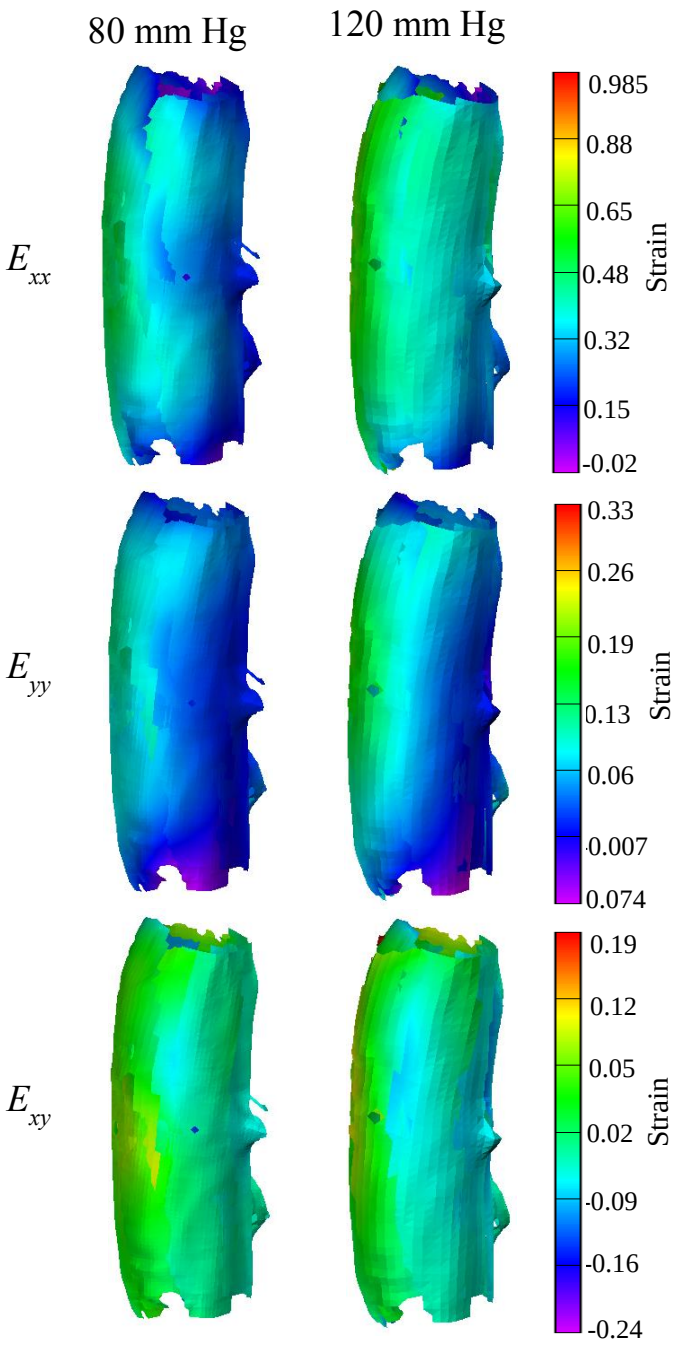

Figure 6.4: Stereo-DIC Measurements. Green-Lagrange strain measurements in the *x*- (circumferential), *y*- (axial), and shear directions at 80 and 120 mmHg and axial stretch of λ_z=1.5.

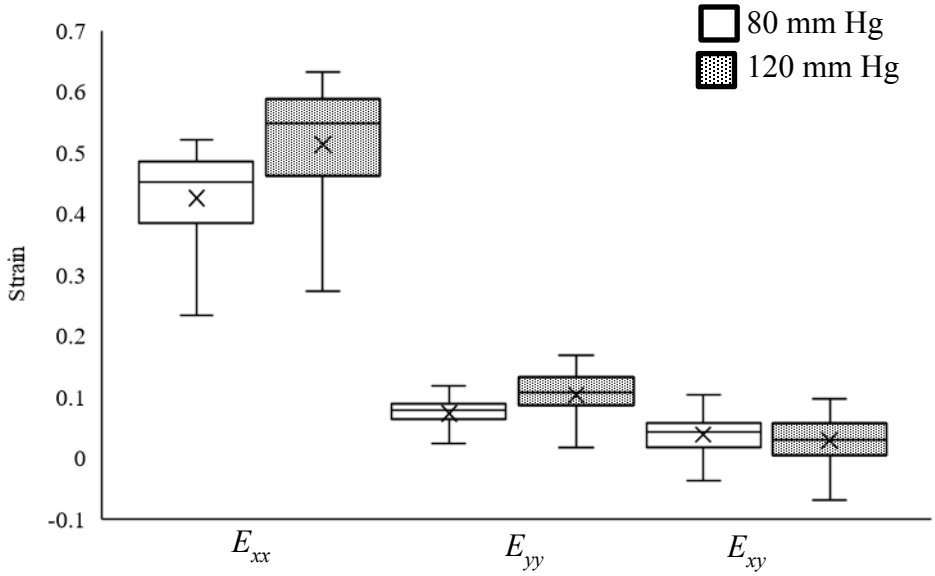

Figure 6.5: Box and Whisker Plot of Strain Data. Strains measured in the *x*-, *y*-, and shear directions at 80 mmHg and 120 mmHg from the unloaded state with x marking mean values.

CHAPTER 7

CONCLUSIONS

Vascular tissues exhibit a unique structure-function relationship heavily dependent on physiological loads within the body, with microstructural environments actively maintained by resident vascular cells to preserve their homeostatic mechanical environment. Alterations in extracellular matrix (ECM) constituents such as collagen and elastin are directly reflected in the mechanical function and properties of vascular tissues. In pathophysiological states, vascular cell dysfunction and altered mechanical loads trigger maladaptive remodeling responses in attempt to regain mechanical homeostasis, and as chronic pathologies persist, disparity between ECM synthesis and degradation results in spatially heterogeneous microstructural environments that may lead to complex localized deformations and weakened vascular walls. As the aorta is the central conduit for distal tissue perfusion and failure thereof often results in morbidity, further examination and characterization of aortopathies with complex biomechanical and cellular manifestations using murine models can reveal crucial information with potential for clinical translation to improve diagnostic and therapeutic management strategies.

Aortopathies refer to a wide range of syndromic and non-syndromic cardiovascular pathologies such as mural calcification, atherosclerosis, and familial connective tissue disorders such as Loeys-Dietz syndrome (LDS) that are often concomitant with aortic

aneurysms (AAs) and dissection. AAs are broadly diagnosed as focal dilations of the aorta, with current clinical management strategies based on macroscopic assessments of size and growth rates through ultrasonography, with little insight on microstructural changes outside of aortic biopsies, that can lead to premature or unnecessary intervention. As vascular function is directly influenced by the microstructural environment, improved microstructural information in conjunction with current clinical management strategies can improve AA prognoses. To this aim, we show that localization of fragmented-elastin-targeted gold nanoparticles (AuNP) in elastase-treated *in vitro* murine AAs can be used to indicate alterations in arterial mechanics (Chapter 2). Elastolysis is nearly ubiquitous to aortopathic AAs and can be readily visualized with uptake and localization of elastin-fragment-targeting AuNPs through computed tomography (CT) imaging modalities, providing improved AA diagnostic imaging methods linked to microstructural changes in elastin content that reflect altered vascular mechanical performance.

In contrast to non-syndromic AAs, where clinicians may decide not to intervene due to AA stabilization, syndromic AAs such as those in LDS show aggressive growth rates with high propensity for sudden dissection, making surgical intervention necessary and crucial to patient outcomes. Thus, improved understanding of the underlying disease mechanisms and biomechanical manifestations in LDS may reveal potential therapeutic avenues to curb the aggressive AA growth and dissection. As noted in this work, LDS is a genetic disorder resulting in dysfunctional transforming growth factor-beta (TGFβ) signaling dependent on three specific TGFβ ligands: TGFβ1 , TGFβ2, TGFβ3; two cell-surface receptors: TGFBR1, TGFBR2; and TGFβ-related signaling pathways: SMAD3. The TGFβ family of cytokines is pluripotent, with a host of context-dependent functions

in physiological processes, and vital for vascular homeostasis. Previous research has shown confounding and perplexing compensatory TGFβ signaling in LDS patients, warranting further examination of specific TGFβ ligand roles in aortopathy formation and progression. We utilize specific TGFβ ligand haploinsufficient murine models (*Tgfb1*$^{+/-}$, *Tgfb2*$^{+/-}$, and *Tgfb3*$^{+/-}$) to investigate loss-of-function in respective ligands and its effect on both passive and active mechanics of the ascending thoracic aorta with standard biaxial mechanical analyses and wire myography. TGFβ ligand haploinsufficient models manifest with certain biaxial mechanical differences in disease stages meant to represent early or pre-disease onset (Chapter 3). Additionally, loss-of-function of specific TGFβ ligands revealed distinct alterations in smooth muscle contractility with *Tgfb1*$^{+/-}$ approaching significance for slightly hypocontractile, *Tgfb2*$^{+/-}$ significantly hypocontractile, and *Tgfb3*$^{+/-}$ displaying hypercontractile smooth muscle cell responses (Chapter 4).

As alluded to above, aortopathies contribute to maladaptive remodeling responses that result in spatially heterogeneous tissues with complex geometries often observed in AAs. Standard biaxial mechanical techniques are capable of capturing the nonlinear homogeneous deformations of arterial tissues in order to provide global descriptors of vascular disease. However, heterogeneous and asymmetric tissues undergo complex local inhomogeneous deformations due to regional variations in vascular microstructures. To improve *in vitro* analyses of pathological tissues, full-field measurement techniques such as StereoDIC can be used. StereoDIC is a non-contact optical imaging technique that uses two cameras oriented at different perspectives of a common region with a unique speckle pattern to track surface motions and deformations in 3D. As the utility of StereoDIC is evident in full-field measurements, there are challenges for application in murine soft

tissues such as maintaining tissue hydration, which requires optical interfaces between the camera and specimen, introducing optical distortions that are exacerbated at high magnifications. Additionally, as aortopathies are axially and circumferentially heterogeneous, multiple stereo camera systems are often required to gather 360° information, adding significant costs to experimental set-ups. To overcome these challenges, we adopted a unique cost-effective approach to implementation of full field 360° StereoDIC by designing a device that rotates one stereo-rig about a centrally fixed specimen, acquiring images at 45° intervals. The device is also equipped to enable standard biaxial mechanical analyses with axial force measurements and controlled axial extensions. First, we validate inherent measurement bias introduced through optical distortions at interfaces, rotation of the stereo rig about the specimen, and rigid body motion of simple and complex shapes (Chapter 5), followed by full field 360° strain measurements of the murine descending aorta undergoing inflation-extension testing to then show the device functionality (Chapter 6) for future studies on diseased tissues.

In conclusion, AAs and other aortopathies present complex clinical and experimental challenges that must be addressed to comprehensively characterize the biomechanical characteristics of diseased blood vessels and gain insight into underlying mechanisms. A paradigm shift from global to local histological and mechanical metrics can be used to address the complex heterogeneous deformations observed in aortopathic diseases. StereoDIC enables strain field measurements and, when combined with advances in inverse methods and constitutive modeling, can be used to estimate regional material parameters that reflect local microstructural changes. Advanced experimental and analytical approaches can then be used to improve temporal and longitudinal translational

studies of AA disease to drive innovation for improved diagnostic, surgical and therapeutic approaches.

REFERENCES

1. Humphrey JD. Vascular adaptation and mechanical homeostasis at tissue, cellular, and sub-cellular levels. Cell Biochem Biophys. 2008;50: 53–78. doi:10.1007/s12013-007-9002-3
2. Zhou B, Alshareef M, Prim D, Collins M, Kempner M, Hartstone-Rose A, et al. The perivascular environment along the vertebral artery governs segment-specific structural and mechanical properties. Acta Biomater. 2016;45: 286–295. doi:http://dx.doi.org/10.1016/j.actbio.2016.09.004
3. Haskett D, Johnson G, Zhou A, Utzinger U, Vande Geest J. Microstructural and biomechanical alterations of the human aorta as a function of age and location. Biomech Model Mechanobiol. 2010;9: 725–736. doi:10.1007/s10237-010-0209-7
4. Zengin E. Vascular wall resident progenitor cells: a source for postnatal vasculogenesis. Development. 2006;133: 1543–1551. doi:10.1242/dev.02315
5. Hu Y, Zhang Z, Torsney E, Afzal AR, Davison F, Metzler B, et al. Abundant progenitor cells in the adventitia contribute to atherosclerosis of vein grafts in ApoE-deficient mice. J Clin Invest. 2004;113: 1258–1265. doi:10.1172/JCI19628
6. Moos MPW, John N, Gräbner R, Noßmann S, Günther B, Vollandt R, et al. The lamina adventitia is the major site of immune cell accumulation in standard chow-fed apolipoprotein E-deficient mice. Arterioscler Thromb Vasc Biol. 2005;25: 2386–2391. doi:10.1161/01.ATV.0000187470.31662.fe

7. Kau T, Sinzig M, Gasser J, Lesnik G, Rabitsch E, Celedin S, et al. Aortic development and anomalies. Semin Intervent Radiol. 2007;24: 141–152. doi:10.1055/s-2007-980040

8. Berillis P. The Role of Collagen in the Aorta's Structure. Open Circ Vasc J. 2013;6: 1–8. doi:10.2174/1877382601306010001

9. Humphrey JD. Cardiovascular Solid Mechanics: Cells, Tissues, and Organs. New York: Springer; 2002. doi:10.1007/978-0-387-21576-1

10. Faury G. Function-structure relationship of elastic arteries in evolution: From microfibrils to elastin and elastic fibres. Pathol Biol. 2001;49: 310–325. doi:10.1016/S0369-8114(01)00147-X

11. Eberth JF, Taucer AI, Wilson E, Humphrey JD. Mechanics of Carotid Arteries in a Mouse Model of Marfan Syndrome. Ann Biomed Eng. Springer US; 2009;37: 1093–1104. doi:10.1007/s10439-009-9686-1

12. Sethi S, Rivera O, Oliveros R, Chilton R. Aortic stiffness: pathophysiology, clinical implications, and approach to treatment. Integr Blood Press Control. 2014;7: 29. doi:10.2147/IBPC.S59535

13. Tsamis A, Krawiec JT, Vorp DA. Elastin and collagen fibre microstructure of the human aorta in ageing and disease: A review. J R Soc Interface. 2013;10. doi:10.1098/rsif.2012.1004

14. Prim DA, Potts J, Eberth J. Pulsatile Perfusion Bioreactor for Biomimetic Vascular Impedances. J Med Device. ASME; 2018;

15. Dao HH, Essalihi R, Bouvet C, Moreau P. Evolution and modulation of age-related medial elastocalcinosis: Impact on large artery stiffness and isolated systolic hypertension. Cardiovasc Res. 2005;66: 307–317. doi:10.1016/j.cardiores.2005.01.012

16. Safar ME. Pulse pressure, arterial stiffness, and cardiovascular risk. Curr Opin Cardiol. 2001/01/04. 2000;15: 258–263.

17. Shimizu K, Mitchell RN, Libby P. Inflammation and cellular immune responses in abdominal aortic aneurysms. Arterioscler Thromb Vasc Biol. 2006;26: 987–994. doi:10.1161/01.ATV.0000214999.12921.4f

18. Collins MJ, Eberth JF, Wilson E, Humphrey JD. Acute mechanical effects of elastase on the infrarenal mouse aorta: Implications for models of aneurysms. J Biomech. Elsevier; 2012;45: 660–665. doi:10.1016/J.JBIOMECH.2011.12.013

19. Campa JS, Greenhalgh RM, Powell JT. Elastin degradation in abdominal aortic aneurysms. Atherosclerosis. Elsevier; 1987;65: 13–21. doi:10.1016/0021-9150(87)90003-7

20. Dua A, Kuy S, Lee CJ, Upchurch GR, Desai SS. Epidemiology of aortic aneurysm repair in the United States from 2000 to 2010. J Vasc Surg. Elsevier; 2014;59: 1512–7. doi:10.1016/j.jvs.2014.01.007

21. Wanhainen A, Björck M, Boman K, Rutegård J, Bergqvist D. Influence of diagnostic criteria on the prevalence of abdominal aortic aneurysm. J Vasc Surg. Elsevier; 2001;34: 229–235. doi:10.1067/mva.2001.115801

22. Singh K, Bonaa KH, Jacobsen BK, Bjork L, Solberg S. Prevalence of and risk factors for abdominal aortic aneurysms in a population-based study : The Tromso Study. Am J Epidemiol. 2001;154: 236–244. doi:10.1093/aje/154.3.236

23. Norman PE, Curci JA. Understanding the effects of tobacco smoke on the pathogenesis of aortic aneurysm. Arterioscler Thromb Vasc Biol. 2013;33: 1473–1477. doi:10.1161/ATVBAHA.112.300158

24. Brownstein AJ, Ziganshin BA, Kuivaniemi H, Body SC, Bale AE, Elefteriades JA. Genes Associated with Thoracic Aortic Aneurysm and Dissection: An Update and Clinical Implications. Aorta (Stamford, Conn). 2017;5: 11–20. doi:10.12945/j.aorta.2017.17.003

25. Loeys BL, Schwarze U, Holm T, Callewaert BL, Thomas GH, Pannu H, et al. Aneurysm Syndromes Caused by Mutations in the TGF-β Receptor. N Engl J Med. 2006;355: 788–798. doi:10.1056/NEJMoa055695

26. Schepers D, Tortora G, Morisaki H, MacCarrick G, Lindsay M, Liang D, et al. A mutation update on the LDS-associated genes TGFB2/3 and SMAD2/3. Hum Mutat. 2018;39: 621–634. doi:10.1002/humu.23407

27. Lasheras JC. The Biomechanics of Arterial Aneurysms. Annu Rev Fluid Mech. 2007;39: 293–319. doi:10.1146/annurev.fluid.39.050905.110128

28. Chow MJ, Mondonedo JR, Johnson VM, Zhang Y. Progressive structural and biomechanical changes in elastin degraded aorta. Biomech Model Mechanobiol. 2013;12: 361–372. doi:10.1007/s10237-012-0404-9

29. Staiculescu MC, Kim J, Mecham RP, Wagenseil JE. Mechanical behavior and matrisome gene expression in the aneurysm-prone thoracic aorta of newborn lysyl oxidase knockout mice. American Journal of Physiology-Heart and Circulatory Physiology. 2017. doi:10.1152/ajpheart.00712.2016

30. Marque V, Kieffer P, Gayraud B, Lartaud-Idjouadiene I, Ramirez F, Atkinson J. Aortic Wall Mechanics and Composition in a Transgenic Mouse Model of Marfan Syndrome. Arterioscler Thromb Vasc Biol. 2001;21: 1184–1189. doi:10.1161/hq0701.092136

31. Adair-Kirk T, Senior R. Fragments of extracellular matrix as mediators of inflammation. Int J Biochem Cell Biol. 2008;40: 1101–1110. doi:10.1016/j.biocel.2007.12.005

32. Baxter BT, Terrin MC, Dalman RL. Medical Management of Small Abdominal Aortic Aneurysms. Circulation. 2008;117: 1883–1889. doi:10.1161/CIRCULATIONAHA.107.735274

33. Grant MW, Thomson IA, Van Rij AM. In-hospital mortality of ruptured abdominal aortic aneurysm. ANZ J Surg. 2008;78: 698–704. doi:10.1111/j.1445-2197.2008.04621.x

34. Johansson G, Markström U, Swedenborg J. Ruptured thoracic aortic aneurysms: A study of incidence and mortality rates. J Vasc Surg. Mosby; 1995;21: 985–988. doi:10.1016/S0741-5214(95)70227-X

35. Hiratzka LF, Bakris GL, Beckman JA, Bersin RM, Carr VF, Casey DE, et al. 2010 ACCF/AHA/AATS/ACR/ASA/SCA/SCAI/SIR/STS/SVM guidelines for the diagnosis and management of patients with Thoracic Aortic Disease: a report of the

American College of Cardiology Foundation/American Heart Association Task Force on Practice Guidelines, A. Circulation. 2010;121: e266-369. doi:10.1161/CIR.0b013e3181d4739e

36. Hall AJ, Busse EF, McCarville DJ, Burgess JJ. Aortic wall tension as a predictive factor for abdominal aortic aneurysm rupture: improving the selection of patients for abdominal aortic aneurysm repair. Ann Vasc Surg. 2000;14: 152–157. doi:10.1007/s100169910027

37. Choksy SA, Wilmink AB, Quick CR. Ruptured abdominal aortic aneurysm in the Huntingdon district: a 10-year experience. Ann R Coll Surg Engl. Royal College of Surgeons of England; 1999;81: 27–31. Available: http://www.ncbi.nlm.nih.gov/pubmed/10325681

38. Aggarwal S, Qamar A, Sharma V, Sharma A. Abdominal aortic aneurysm: A comprehensive review. Exp Clin Cardiol. Pulsus Group; 2011;16: 11–5. Available: http://www.ncbi.nlm.nih.gov/pubmed/21523201

39. Gazoni LM, Speir AM, Kron IL, Fonner E, Crosby IK. Elective Thoracic Aortic Aneurysm Surgery: Better Outcomes from High-Volume Centers. J Am Coll Surg. Elsevier; 2010;210: 855–859. doi:10.1016/J.JAMCOLLSURG.2010.01.013

40. Williams JA, Loeys BL, Nwakanma LU, Dietz HC, Spevak PJ, Patel ND, et al. Early Surgical Experience With Loeys-Dietz: A New Syndrome of Aggressive Thoracic Aortic Aneurysm Disease. Ann Thorac Surg. 2007;83. doi:10.1016/j.athoracsur.2006.10.091

41. Wang X, Lane BA, Eberth JF, Lessner SM, Vyavahare NR. Gold nanoparticles that target degraded elastin improve imaging and rupture prediction in an AngII mediated mouse model of abdominal aortic aneurysm. Theranostics. 2019;9: 4156–4167. doi:10.7150/thno.34441

42. Sinha A, Shaporev A, Nosoudi N, Lei Y, Vertegel A, Lessner S, et al. Nanoparticle targeting to diseased vasculature for imaging and therapy. Nanomedicine Nanotechnology, Biol Med. Elsevier; 2014;10: e1003–e1012. doi:10.1016/J.NANO.2014.02.002

43. Shirasu T, Koyama H, Miura Y, Hoshina K, Kataoka K, Watanabe T. Nanoparticles effectively target rapamycin delivery to sites of experimental aortic aneurysm in rats. PLoS One. 2016;11: 1–21. doi:10.1371/journal.pone.0157813

44. Maier A, Gee MW, Reeps C, Pongratz J, Eckstein H-H, Wall WA. A Comparison of Diameter, Wall Stress, and Rupture Potential Index for Abdominal Aortic Aneurysm Rupture Risk Prediction. Ann Biomed Eng. Springer US; 2010;38: 3124–3134. doi:10.1007/s10439-010-0067-6

45. Vorp DA. Biomechanics of abdominal aortic aneurysm. J Biomech. Elsevier; 2007;40: 1887–1902. doi:10.1016/J.JBIOMECH.2006.09.003

46. Daugherty A, Manning MW, Cassis LA. Angiotensin II promotes atherosclerotic lesions and aneurysms in apolipoprotein E–deficient mice. J Clin Invest. 2000;105. doi:10.1172/JCI7818

47. Tsui JC. Experimental models of abdominal aortic aneurysms. Open Cardiovasc Med J. Bentham Science Publishers; 2010;4: 221–30. doi:10.2174/1874192401004010221

48. Wang Y, Krishna S, Golledge J. The calcium chloride-induced rodent model of abdominal aortic aneurysm. Atherosclerosis. Elsevier Ltd; 2013;226: 29–39. doi:10.1016/j.atherosclerosis.2012.09.010

49. Habashi JP. Losartan, an AT1 Antagonist, Prevents Aortic Aneurysm in a Mouse Model of Marfan Syndrome. Science (80-). 2006;312: 117–121. doi:10.1126/science.1124287

50. Abdul-Hussien H, Hanemaaijer R, Verheijen JH, van Bockel JH, Geelkerken RH, Lindeman JHN. Doxycycline therapy for abdominal aneurysm: Improved proteolytic balance through reduced neutrophil content. J Vasc Surg. The Society for Vascular Surgery; 2009;49: 741–749. doi:10.1016/j.jvs.2008.09.055

51. Prall AK, Longo GM, Mayhan WG, Waltke EA, Fleckten B, Thompson RW, et al. Doxycycline in patients with abdominal aortic aneurysms and in mice: Comparison of serum levels and effect on aneurysm growth in mice. J Vasc Surg. 2002;35: 923–929. doi:10.1067/mva.2002.123757

52. Genovese K, Lee YU, Humphrey JD. Novel optical system for in vitro quantification of full surface strain fields in small arteries: I. Theory and design. Comput Methods Biomech Biomed Engin. 2011;14: 227–37. doi:10.1080/10255842.2010.545823

53. Genovese K, Collins MJ, Lee YU, Humphrey JD. Regional Finite Strains in an Angiotensin-II Induced Mouse Model of Dissecting Abdominal Aortic Aneurysms. Cardiovasc Eng Technol. 2012;3: 194–202. doi:10.1007/s13239-012-0083-9

54. Bersi MR, Bellini C, Di Achille P, Humphrey JD, Genovese K, Avril S. Novel Methodology for Characterizing Regional Variations in the Material Properties of Murine Aortas. J Biomech Eng. American Society of Mechanical Engineers; 2016;138: 071005. doi:10.1115/1.4033674

55. Schreier H, Orteu J-J, Sutton M a. Image Correlation for Shape, Motion and Deformation Measurements [Internet]. Springer, New York. 2009. doi:10.1007/978-0-387-78747-3

56. Vande Geest JP, Sacks MS, Vorp DA. The effects of aneurysm on the biaxial mechanical behavior of human abdominal aorta. J Biomech. Elsevier; 2006;39: 1324–1334. doi:10.1016/J.JBIOMECH.2005.03.003

57. Ferruzzi J, Vorp DA, Humphrey JD. On constitutive descriptors of the biaxial mechanical behaviour of human abdominal aorta and aneurysms. J R Soc Interface. The Royal Society; 2011;8: 435–50. doi:10.1098/rsif.2010.0299

58. Marais L, Zidi M. Mechanical behavior of the abdominal aortic aneurysm assessed by biaxial tests in the rat xenograft model. J Mech Behav Biomed Mater. Elsevier; 2017;74: 28–34. doi:10.1016/J.JMBBM.2017.04.029

59. Pancheri FQ, Peattie RA, Reddy ND, Ahamed T, Lin W, Ouellette TD, et al. Histology and Biaxial Mechanical Behavior of Abdominal Aortic Aneurysm Tissue Samples. J Biomech Eng. American Society of Mechanical Engineers; 2017;139: 031002. doi:10.1115/1.4035261

60. Seshaiyer P, Hsu FPK, Shah AD, Kyriacou SK, Humphrey JD. Multiaxial Mechanical Behavior of Human Saccular Aneurysms. Comput Methods Biomech Biomed Engin. 2001;4: 281–289. doi:10.1080/10255840108908009

61. Vorp DA, Schiro BJ, Ehrlich MP, Juvonen TS, Ergin MA, Griffith BP. Effect of aneurysm on the tensile strength and biomechanical behavior of the ascending thoracic aorta. Ann Thorac Surg. 2003;75: 1210–1214. doi:10.1016/S0003-4975(02)04711-2

62. Kanagasabay R, Gajraj H, Pointon L, Scott RAP. Co-morbidity in patients with abdominal aortic aneurysm. J Med Screen. SAGE Publications Sage UK: London, England; 1996;3: 208–210.

63. Humphrey JD, Milewicz DM, Tellides G, Schwartz MA. Dysfunctional Mechanosensing in Aneurysms. Science (80-). 2014;344: 477 LP – 479.

64. Ailawadi G, Eliason JL, Upchurch GR. Current concepts in the pathogenesis of abdominal aortic aneurysm. J Vasc Surg. Elsevier; 2003;38: 584–588. doi:10.1016/S0741-5214(03)00324-0

65. Sakalihasan N, Limet R, Defawe O. Abdominal aortic aneurysm. Lancet. Elsevier; 2005;365: 1577–1589. doi:10.1016/S0140-6736(05)66459-8

66. Petersen E, Wågberg F, Angquist KA. Proteolysis of the abdominal aortic aneurysm wall and the association with rupture. Eur J Vasc Endovasc Surg. Elsevier; 2002;23: 153–7. doi:10.1053/ejvs.2001.1572

67. Vallabhaneni SR, Gilling-Smith GL, How T V., Carter SD, Brennan J a., Harris PL. Heterogeneity of Tensile Strength and Matrix Metalloproteinase Activity in the Wall of Abdominal Aortic Aneurysms. J Endovasc Ther. 2004;11: 494–502. doi:10.1583/04-1239.1

68. Fillinger MF, Raghavan ML, Marra SP, Cronenwett JL, Kennedy FE. In vivo analysis of mechanical wall stress and abdominal aortic aneurysm rupture risk. J Vasc Surg. Elsevier; 2002;36: 589–597. doi:10.1067/mva.2002.125478

69. Dobrin PB, Mrkvicka R. Failure of Elastin or Collagen as Possible Critical Connective Tissue Alterations Underlying Aneurysmal Dilatation: http://dx.doi.org/101177/096721099400200412. SAGE PublicationsSage UK: London, England; 2016; doi:10.1177/096721099400200412

70. Shahmansouri N, Alreshidan M, Emmott A, Lachapelle K, Cartier R, Leask RL, et al. Evaluating ascending aortic aneurysm tissue toughness: Dependence on collagen and elastin contents. J Mech Behav Biomed Mater. Elsevier; 2016;64: 262–271. doi:10.1016/J.JMBBM.2016.08.006

71. Carmo M, Colombo L, Bruno A, Corsi FRM, Roncoroni L, Cuttin MS, et al. Alteration of elastin, collagen and their cross-links in abdominal aortic aneurysms. Eur J Vasc Endovasc Surg. Elsevier; 2002;23: 543–9. doi:10.1053/EJVS.2002.1620

72. Airhart N, Brownstein BH, Cobb JP, Schierding W, Arif B, Ennis TL, et al. Smooth muscle cells from abdominal aortic aneurysms are unique and can independently and synergistically degrade insoluble elastin. J Vasc Surg. Elsevier Inc.; 2014;60: 1033-1042.e5. doi:10.1016/j.jvs.2013.07.097

73. Ferruzzi J, Collins MJ, Yeh AT, Humphrey JD. Mechanical assessment of elastin integrity in fibrillin-1-deficient carotid arteries: implications for Marfan syndrome. Cardiovasc Res. Oxford University Press; 2011;92: 287–295. doi:10.1093/cvr/cvr195

74. Holmes DR, Liao S, Parks WC, Hompson RW. Medial neovascularization in abdominal aortic aneurysms: A histopathologic marker of aneurysmal degeneration with pathophysiologic implications. J Vasc Surg. Elsevier; 1995;21: 761–772. doi:10.1016/S0741-5214(05)80007-2

75. Ostdiek AM, Ivey JR, Grant DA, Gopaldas J, Grant SA. An in vivo study of a gold nanocomposite biomaterial for vascular repair. Biomaterials. Elsevier; 2015;65: 175–183. doi:10.1016/J.BIOMATERIALS.2015.06.045

76. Lei Y, Nosoudi N, Vyavahare N. Targeted chelation therapy with EDTA-loaded albumin nanoparticles regresses arterial calcification without causing systemic side effects. J Control Release. Elsevier; 2014;196: 79–86. doi:10.1016/J.JCONREL.2014.09.029

77. Nosoudi N, Chowdhury A, Siclari S, Parasaram V, Karamched S, Vyavahare N. Systemic Delivery of Nanoparticles Loaded with Pentagalloyl Glucose Protects Elastic Lamina and Prevents Abdominal Aortic Aneurysm in Rats. J Cardiovasc Transl Res. 2016;9: 445–455. doi:10.1007/s12265-016-9709-x

78. Prim DA, Mohamed MA, Lane BA, Poblete K, Wierzbicki MA, Lessner SM, et al. Comparative mechanics of diverse mammalian carotid arteries. PLoS One. 2018;13: 1–18. doi:10.1371/journal.pone.0202123

79. Raaz U, Zöllner AM, Schellinger IN, Toh R, Nakagami F, Brandt M, et al. Segmental aortic stiffening contributes to experimental abdominal aortic aneurysm development. Circulation. 2015;131: 1783–1795. doi:10.1161/CIRCULATIONAHA.114.012377

80. Iliopoulos DC, Kritharis EP, Giagini AT, Papadodima SA, Sokolis DP. Ascending thoracic aortic aneurysms are associated with compositional remodeling and vessel stiffening but not weakening in age-matched subjects. J Thorac Cardiovasc Surg. The American Association for Thoracic Surgery; 2009;137: 101–109. doi:10.1016/j.jtcvs.2008.07.023

81. Moxon J V, Parr A, Emeto TI, Walker P, Norman PE, Golledge J. Diagnosis and Monitoring of Abdominal Aortic Aneurysm: Current Status and Future Prospects. Curr Probl Cardiol. 2010;35: 512–548. doi:10.1016/j.cpcardiol.2010.08.004

82. Doetschman T, Barnett J V, Runyan RB, Camenisch TD, Heimark RL, Granzier HL, et al. Transforming growth factor beta signaling in adult cardiovascular diseases and repair. Cell Tissue Res. 2012;347: 203–223.

83. Hu JH, Wei H, Jaffe M, Airhart N, Du L, Angelov SN, et al. Postnatal Deletion of the Type II Transforming Growth Factor-beta Receptor in Smooth Muscle Cells Causes Severe Aortopathy in Mice. Arter Thromb Vasc Biol. 2015;35: 2647–2656. doi:10.1161/ATVBAHA.115.306573

84. Lindsay ME, Schepers D, Bolar NA, Doyle JJ, Gallo E, Fert-Bober J, et al. Loss-of-function mutations in TGFB2 cause a syndromic presentation of thoracic aortic aneurysm. Nat Genet. 2012;44: 922–927.

85. Boileau C, Guo DC, Hanna N, Regalado ES, Detaint D, Gong L, et al. TGFB2 mutations cause familial thoracic aortic aneurysms and dissections associated with mild systemic features of Marfan syndrome. Nat Genet. 2012;44: 916–921.

86. Cook JR, Carta L, Galatioto J, Ramirez F. Cardiovascular manifestations in Marfan syndrome and related diseases; multiple genes causing similar phenotypes. Clin Genet. 2014; 10.

87. Akhurst RJ, Hata A. Targeting the TGFbeta signalling pathway in disease. Nat Rev Drug Discov. 2012;11: 790–811.

88. Maccarrick G, Black III JH, Bowdin S, El-Hamamsy I, Frischmeyer-Guerrerio PA, Guerrerio AL, et al. Loeys-Dietz syndrome: a primer for diagnosis and management. Genet Med. 2014; 10.

89. Loeys BL, Mortier G, Dietz HC. Bone lessons from Marfan syndrome and related disorders: fibrillin, TGF-B and BMP at the balance of too long and too short. Pediatr Endocrinol Rev. 2013;10 Suppl 2: 417–423.

90. Ramirez F, Sakai LY, Rifkin DB, Dietz HC. Extracellular microfibrils in development and disease. Cell Mol Life Sci. 2007;64: 2437–2446.

91. Loeys BL, Schwarze U, Holm T, Callewaert BL, Thomas GH, Pannu H, et al. Aneurysm syndromes caused by mutations in the TGF-beta receptor. N Engl J Med. 2006;355: 788–798.

92. Bertoli-Avella AM, Gillis E, Morisaki H, Verhagen JMA, de Graaf BM, van de Beek G, et al. Mutations in a TGF-β Ligand, TGFB3, Cause Syndromic Aortic Aneurysms and Dissections. J Am Coll Cardiol. 2015;65: 1324–1336. doi:https://doi.org/10.1016/j.jacc.2015.01.040

93. Takeda N, Hara H, Fujiwara T, Kanaya T, Maemura S, Komuro I. TGF-β Signaling-Related Genes and Thoracic Aortic Aneurysms and Dissections. Int J Mol Sci. 2018;19: 2125. doi:10.3390/ijms19072125

94. Mu Y, Gudey SK, Landstrom M. Non-Smad signaling pathways. Cell Tissue Res. 2012;347: 11–20.

95. Moustakas A, Heldin CH. The regulation of TGFbeta signal transduction. Development. 2009;136: 3699–3714.

96. Roberts AB. Molecular and cell biology of TGF-beta. Miner Electrolyte Metab. 1998;24: 111–119.

97. Pardali E, Ten DP. TGFbeta signaling and cardiovascular diseases. Int J Biol Sci. 2012;8: 195–213.

98. Wharton K, Derynck R. TGFbeta family signaling: novel insights in development and disease. Development. 2009;136: 3691–3697.

99. Gittenberger-de Groot AC, Azhar M, Molin DG. Transforming growth factor beta-SMAD2 signaling and aortic arch development. Trends Cardiovasc Med. 2006;16: 1–6.

100. Azhar M, Schultz JEJ, Grupp I, Dorn GW, Meneton P, Molin DGM, et al. Transforming growth factor beta in cardiovascular development and function. Cytokine Growth Factor Rev. 2003;14: 391–407. Available: http://www.ncbi.nlm.nih.gov/pubmed/12948523

101. Molin DG, Bartram U, Van der HK, Van Iperen L, Speer CP, Hierck BP, et al. Expression patterns of Tgfbeta1-3 associate with myocardialisation of the outflow tract and the development of the epicardium and the fibrous heart skeleton. Dev Dyn. 2003;227: 431–444.

102. Millan FA, Denhez F, Kondaiah P, Akhurst RJ. Embryonic gene expression patterns of TGF beta 1, beta 2 and beta 3 suggest different developmental functions in vivo. Development. 1991;111: 131–143.

103. Arthur HM, Bamforth SD. TGFbeta signaling and congenital heart disease: Insights from mouse studies. Birth Defects Res A Clin Mol Teratol. 2011;91: 423–434.

104. Ferruzzi J, Murtada S Il, Li G, Jiao Y, Uman S, Ting MYL, et al. Pharmacologically improved contractility protects against aortic dissection in mice with disrupted transforming growth factor-β signaling despite compromised extracellular matrix properties. Arterioscler Thromb Vasc Biol. 2016;36: 919–927. doi:10.1161/ATVBAHA.116.307436

105. Bellini C, Bersi MR, Caulk AW, Ferruzzi J, Milewicz DM, Ramirez F, et al. Comparison of 10 murine models reveals a distinct biomechanical phenotype in thoracic aortic aneurysms. J R Soc Interface. The Royal Society; 2017;14: 20161036. doi:10.1098/rsif.2016.1036

106. Lindsay ME, Schepers D, Bolar NA, Doyle JJ, Gallo E, Fert-Bober J, et al. Loss-of-function mutations in TGFB2 cause a syndromic presentation of thoracic aortic aneurysm. Nat Genet. Nature Publishing Group; 2012;44: 922–927. doi:10.1038/ng.2349

107. Mann BK, Schmedlen RH, West JL. Tethered-TGF-β increases extracellular matrix production of vascular smooth muscle cells. Biomaterials. 2001;22: 439–444. doi:10.1016/S0142-9612(00)00196-4

108. Roberts AB, McCune BK, Sporn MB. TGF-β: Regulation of extracellular matrix. Kidney Int. Elsevier Masson SAS; 1992;41: 557–559. doi:10.1038/ki.1992.81

109. Hinderer S, Shen N, Ringuette LJ, Hansmann J, Reinhardt DP, Brucker SY, et al. In vitro elastogenesis: Instructing human vascular smooth muscle cells to generate an elastic fiber-containing extracellular matrix scaffold. Biomed Mater. 2015;10. doi:10.1088/1748-6041/10/3/034102

110. Guo X. Transforming growth factor-β and smooth muscle differentiation. World J Biol Chem. 2012;3: 41. doi:10.4331/wjbc.v3.i3.41

111. Rensen SSM, Doevendans PAFM, Van Eys GJJM. Regulation and characteristics of vascular smooth muscle cell phenotypic diversity. Netherlands Hear J. 2007;15: 100–108. doi:10.1007/BF03085963

112. Zhang Y, Alexander PB, Wang XF. TGF-β family signaling in the control of cell proliferation and survival. Cold Spring Harb Perspect Biol. 2017;9. doi:10.1101/cshperspect.a022145

113. Bogunovic N, Meekel JP, Micha D, Blankensteijn JD, Hordijk PL, Yeung KK. Impaired smooth muscle cell contractility as a novel concept of abdominal aortic aneurysm pathophysiology. Sci Rep. 2019;9: 1–14. doi:10.1038/s41598-019-43322-3

114. Zhou B, Prim DA, Romito EJ, McNamara LP, Spinale FG, Shazly T, et al. Contractile Smooth Muscle and Active Stress Generation in Porcine Common Carotids. J Biomech Eng. 2017;140: 014501. doi:10.1115/1.4037949

115. Cocciolone AJ, Hawes JZ, Staiculescu MC, Johnson EO, Murshed M, Wagenseil JE. Elastin, arterial mechanics, and cardiovascular disease. Am J Physiol Circ Physiol. American Physiological Society; 2018;315: H189–H205. doi:10.1152/ajpheart.00087.2018

116. Cox RH. Comparison of arterial wall mechanics using ring and cylindrical segments. Am J Physiol Circ Physiol. 1983;244: H298–H303. doi:10.1152/ajpheart.1983.244.2.H298

117. Inamoto S, Kwartler CS, Lafont AL, Liang YY, Fadulu VT, Duraisamy S, et al. TGFBR2 mutations alter smooth muscle cell phenotype and predispose to thoracic aortic aneurysms and dissections. Cardiovasc Res. 2010;88: 520–529. doi:10.1093/cvr/cvq230

118. Nordon IM, Hinchliffe RJ, Loftus IM, Thompson MM. Pathophysiology and epidemiology of abdominal aortic aneurysms. Nat Rev Cardiol. Nature Publishing Group; 2011;8: 92–102. doi:10.1038/nrcardio.2010.180

119. Frank M. Davis, Debra L. Rateri, AD. Abdominal Aortic Aneurysm: Novel Mechanisms and Therapies. Curr Opin Cardiol. 2015;116: 1477–1490. doi:10.1161/CIRCRESAHA.116.303790.The

120. Duprey A, Trabelsi O, Vola M, Favre JP, Avril S. Biaxial rupture properties of ascending thoracic aortic aneurysms. Acta Biomater. 2016;42: 273–285. doi:10.1016/j.actbio.2016.06.028

121. Luo PF, Chao YJ, Sutton MA, Peters WH. Accurate measurement of three-dimensional deformations in deformable and rigid bodies using computer vision. Exp Mech. 1993;33: 123–132. doi:10.1007/BF02322488

122. Helm JD. Improved three- dimensional image correlation for surface displacement measurement. Opt Eng. 2006;35: 1911. doi:10.1117/1.600624

123. Schreier HW, Garcia D, Sutton MA. Advances in light microscope stereo vision. Exp Mech. 2004;44: 278–288. doi:10.1177/0014485104041546

124. Badel P, Avril S, Lessner S, Sutton M. Mechanical identification of layer-specific properties of mouse carotid arteries using 3D-DIC and a hyperelastic anisotropic constitutive model. Comput Methods Biomech Biomed Engin. Taylor & Francis Group ; 2012;15: 37–48. doi:10.1080/10255842.2011.586945

125. Sutton MA, Ke X, Lessner SM, Goldbach M, Yost M, Zhao F, et al. Strain field measurements on mouse carotid arteries using microscopic three-dimensional digital image correlation. J Biomed Mater Res Part A. Wiley-Blackwell; 2008;84A: 178–190. doi:10.1002/jbm.a.31268

126. Kim J-H, Badel P, Duprey A, Favre JP, Avril S. Characterisation of failure in human aortic tissue using digital image correlation. Comput Methods Biomech Biomed Engin. 2011;14: 73–74. doi:10.1080/10255842.2011.592368

127. Eberth JF, Shazly T. Nonlinear Mechanics of Soft Biological Materials. In: Hayenga H, Aranda-Espinoza H, editors. Biomaterial Mechanics. CRC Press; 2017. pp. 25–50. doi:doi:10.1201/9781315152585-3

128. Genovese K, Lee YU, Humphrey JD. Novel optical system for in vitro quantification of full surface strain fields in small arteries: II. Correction for refraction and illustrative results. Comput Methods Biomech Biomed Engin. 2011;14: 213–225. doi:10.1080/10255842.2010.545823

129. Ke X, Sutton MA, Lessner SM, Yost M. Robust stereo vision and calibration methodology for accurate three-dimensional digital image correlation measurements on submerged objects. J Strain Anal Eng Des. 2008;43: 689–704. doi:10.1243/03093247JSA425

130. Daugherty A, Cassis LA. Mouse Models of Abdominal Aortic Aneurysms. Arterioscler Thromb Vasc Biol. 2004;24: 429–434. doi:10.1161/01.ATV.0000118013.72016.ea

131. Wang YQ, Sutton MA, Bruck HA, Schreier HW. Quantitative error assessment in pattern matching: Effects of intensity pattern noise, interpolation, strain and image contrast on motion measurements. Strain. 2009;45: 160–178. doi:10.1111/j.1475-1305.2008.00592.x

132. Ke X-DD, Schreier HW, Sutton MA, Wang YQ, Sutton MA, Ke X-DD, et al. Error Assessment in Stereo-based Deformation Measurements. Exp Mech. 2011;51: 423–441. doi:10.1007/s11340-010-9450-3

133. Ke X-D, Schreier HW, Sutton MA, Wang YQ. Error Assessment in Stereo-based Deformation Measurements. Exp Mech. 2011;51: 423–441. doi:10.1007/s11340-010-9450-3

134. Correlated Solutions I. VIC-3D Image correlation software. 121 Dutchman Blvd, Irmo, SC 29063;

135. Crammond G, Boyd SW, Dulieu-Barton JM. Speckle pattern quality assessment for digital image correlation. Opt Lasers Eng. Elsevier; 2013;51: 1368–1378. doi:10.1016/j.optlaseng.2013.03.014

136. Dong YL, Pan B. A Review of Speckle Pattern Fabrication and Assessment for Digital Image Correlation. Exp Mech. 2017;57: 1161–1181. doi:10.1007/s11340-017-0283-1

137. Lecompte D, Smits A, Bossuyt S, Sol H, Vantomme J, Van Hemelrijck D, et al. Quality assessment of speckle patterns for digital image correlation. Opt Lasers Eng. 2006;44: 1132–1145. doi:10.1016/j.optlaseng.2005.10.004

138. Jones I. A good practices guide for digital image correlation. Int Digit Image Correl Soc. 2018;

139. Bornert M, Brémand F, Doumalin P, Dupré JC, Fazzini M, Grédiac M, et al. Assessment of digital image correlation measurement errors: Methodology and results. Exp Mech. 2009;49: 353–370. doi:10.1007/s11340-008-9204-7

140. Lessner SM, Eberth JF. Beyond the Airbrush: Applications of Digital Image Correlation in Vascular Biomechanics BT - Advancement of Optical Methods & Digital Image Correlation in Experimental Mechanics, Volume 3. In: Lamberti L, Lin M-T, Furlong C, Sciammarella C, Reu PL, Sutton MA, editors. Cham: Springer International Publishing; 2019. pp. 1–4.

141. Avril S, Badel P, Duprey A. Anisotropic and hyperelastic identification of in vitro human arteries from full-field optical measurements. J Biomech. 2010;43: 2978–2985. doi:10.1016/j.jbiomech.2010.07.004

142. Kim JH, Avril S, Duprey A, Favre JP. Experimental characterization of rupture in human aortic aneurysms using a full-field measurement technique. Biomech Model Mechanobiol. 2012;11: 841–853. doi:10.1007/s10237-011-0356-5

143. Humphrey JD, Schwartz MA, Tellides G, Milewicz DM. Role of mechanotransduction in vascular biology: Focus on thoracic aortic aneurysms and dissections. Circ Res. 2015;116: 1448–1461. doi:10.1161/CIRCRESAHA.114.304936

144. Wilson JS, Bersi MR, Li G, Humphrey JD. Correlation of Wall Microstructure and Heterogeneous Distributions of Strain in Evolving Murine Abdominal Aortic Aneurysms. Cardiovasc Eng Technol. 2017; doi:10.1007/s13239-017-0301-6

145. Humphrey JD, Holzapfel GA. Mechanics, mechanobiology, and modeling of human abdominal aorta and aneurysms. J Biomech. Elsevier; 2012;45: 805–814. doi:10.1016/j.jbiomech.2011.11.021

146. Raghavan ML, Vorp DA. Toward a biomechanical tool to evaluate rupture potential of abdominal aortic aneurysm: Identification of a finite strain constitutive model and evaluation of its applicability. J Biomech. 2000;33: 475–482. doi:10.1016/S0021-9290(99)00201-8

147. Vorp DA, Vande Geest JP. Biomechanical determinants of abdominal aortic aneurysm rupture. Arterioscler Thromb Vasc Biol. 2005;25: 1558–1566. doi:10.1161/01.ATV.0000174129.77391.55

148. Genovese K, Lee Y-U, Lee AY, Humphrey JD. An improved panoramic digital image correlation method for vascular strain analysis and material characterization. J Mech Behav Biomed Mater. 2013;27: 132–142. doi:10.1016/j.jmbbm.2012.11.015

149. Ning J, Braxton VG, Wang Y, Sutton MA, Wang Y, Lessner SM. Speckle Patterning of Soft Tissues for Strain Field Measurement Using Digital Image Correlation: Preliminary Quality Assessment of Patterns. Microsc Microanal. 2011;17: 81–90. doi:10.1017/s1431927610094377

150. Grédiac M, Pierron F, Avril S, Toussaint E. The virtual fields method for extracting constitutive parameters from full-field measurements: A review. Strain. 2006;42: 233–253. doi:10.1111/j.1475-1305.2006.00283.x

151. Drury JL, Mooney DJ. Hydrogels for tissue engineering: scaffold design variables and applications. Biomaterials. 2003;24: 4337–4351. doi:http://dx.doi.org/10.1016/S0142-9612(03)00340-5

152. Lee CH, Singla A, Lee Y. Biomedical applications of collagen. Int J Pharm. 2001;221: 1–22. doi:10.1016/S0378-5173(01)00691-3

153. Sherman VR, Yang W, Meyers MA. The materials science of collagen. J Mech Behav Biomed Mater. Elsevier; 2015;52: 22–50. doi:10.1016/j.jmbbm.2015.05.023

154. Prockop DJ, Kivirikko KI. Collagens: molecular biology, diseases, and potentials for therapy. Annu Rev Biochem. Annual Reviews 4139 El Camino Way, PO Box 10139, Palo Alto, CA 94303-0139, USA; 1995;64: 403–434.

155. Abou Neel E, Cheema U, Knowles J, Brown R, Nazhat S. Use of multiple unconfined compression for control of collagen gel scaffold density and mechanical properties. Soft Matter. 2006;2: 986. doi:10.1039/b609784g

156. Yost MJ, Baicu CF, Stonerock CE, Goodwin RL, Price RL, Davis JM, et al. A novel tubular scaffold for cardiovascular tissue engineering. Tissue Eng. 2004;10: 273–284. doi:10.1089/107632704322791916

157. Biechler S V, Junor L, Evans AN, Eberth JF, Price RL, Potts JD, et al. The impact of flow-induced forces on the morphogenesis of the outflow tract. Front Physiol. Frontiers; 2014;5: 225. doi:10.3389/fphys.2014.00225

158. Jones RS, Chang PH, Perahia T, Harmon KA, Junor L, Yost MJ, et al. Design and Fabrication of a Three-Dimensional In Vitro System for Modeling Vascular Stenosis. Microsc Microanal. 2017/07/17. Cambridge University Press; 2017;23: 859–871. doi:DOI: 10.1017/S1431927617012302

159. Ruszczak Z. Effect of collagen matrices on dermal wound healing. Adv Drug Deliv Rev. 2003;55: 1595–1611. doi:10.1016/j.addr.2003.08.003

160. Willoughby C.E, M B, Kaye MD S. Collagen Corneal Shields. Surv Ophthalmol. 2002;47: 174–182.

161. Hasan A, Khattab A, Islam MA, Hweij KA, Zeitouny J, Waters R, et al. Injectable Hydrogels for Cardiac Tissue Repair after Myocardial Infarction. Adv Sci. 2015;2: 1–18. doi:10.1002/advs.201500122

162. Simon DD, Horgan CO, Humphrey JD. Mechanical Restrictions on Biological Responses by Adherent Cells within Collagen Gels. J Mech Behav Biomed Mater. 2013;14: 216–226. doi:10.1016/j.jmbbm.2012.05.009.Mechanical

163. Costa KD, Lee EJ, Holmes JW. Creating alignment and anisotropy in engineered heart tissue: role of boundary conditions in a model three-dimensional culture system. Tissue Eng. 2003;9: 567–577. doi:10.1089/107632703768247278

164. Liu X, Umino T, Cano M, Ertl R, Veys T, Spurzem J, et al. Human bronchial epithelial cells can contract type I collagen gels Human bronchial epithelial cells can contract type I collagen gels. Am J Physiol - Lung Cell Mol Physiol. 1998;274: 58–65.

165. Gourdie RG, Myers T a, McFadden a, Li YX, Potts JD. Self-Organizing Tissue-Engineered Constructs in Collagen Hydrogels. Microsc Microanal. 2012; 1–8. doi:10.1017/s1431927611012372

166. Oyen ML. Mechanical characterisation of hydrogel materials. Int Mater Rev. 2014;59: 44–59. doi:10.1179/1743280413Y.0000000022

167. Knapp DM, Barocas VH, Moon AG, Yoo K, Petzold LR, Tranquillo RT. Rheology of reconstituted type I collagen gel in confined compression. J Rheol (N Y N Y). SOR; 1997;41. doi:10.1122/1.550817

168. Anseth KS, Bowman CN, Brannon-Peppas L. Mechanical properties of hydrogels and their experimental determination. Biomaterials. 1996;17: 1647–1657. doi:10.1016/0142-9612(96)87644-7

169. Roeder BA, Kokini K, Sturgis JE, Robinson JP, Voytik-Harbin SL. Tensile Mechanical Properties of Three-Dimensional Type I Collagen Extracellular Matrices With Varied Microstructure. J Biomech Eng. 2002;124: 214. doi:10.1115/1.1449904

170. Wang X, Li X, Yost MJ. Microtensile testing of collagen fibril for cardiovascular tissue engineering. J Biomed Mater Res A. 2005;74: 263–8. doi:10.1002/jbm.a.30387

171. Ramtani S, Takahashi-Iniguez Y, Helary C, Geiger D, Giraud-Guille MM. Mechanical Behavior Under Unconfined Compression Loadings of Dense Fibrillar Collagen Matrices Mimetic of Living Tissues. J Mech Med Biol. 2010;10: 35–55. doi:10.1142/S0219519410003290

172. Humphrey JD, Delange SL. An introduction to biomechanics: solids and fluids, analysis and design. New York: Springer; 2004.

173. Aljabri B, Al Wahaibi K, Abner D, Mackenzie KS, Corriveau MM, Obrand DI, et al. Patient-reported quality of life after abdominal aortic aneurysm surgery: A prospective comparison of endovascular and open repair. J Vasc Surg. 2006;44. doi:10.1016/j.jvs.2006.08.015

174. Aghvami M, Barocas VH, Sander E a. Multiscale mechanical simulations of cell compacted collagen gels. J Biomech Eng. 2013;135: 71004. doi:10.1115/1.4024460

175. Simon DD, Humphrey JD. On a class of admissible constitutive behaviors in free-floating engineered tissues. Int J Non Linear Mech. Elsevier; 2012;47: 173–178. doi:10.1016/j.ijnonlinmec.2011.04.029

176. Blatz PJ, Ko WL. Application of finite elastic theory to the deformation of rubbery materials. Trans Soc Rheol. 1962;VI: 223–251. doi:10.1122/1.548937

177. Mollica DAF. The role of stress in the growth of a multicell spheroid. Math Biol. 2004;499: 477–499.

178. Beatty MF. Topics in Finite Elasticity: Hyperelasticity of Rubber, Elastomers, and Biological Tissues—With Examples. Appl Mech Rev. ASME; 1987;40: 1699–1734.

179. Horgan CO. Remarks on Ellipticity for the Generalized Blatz-Ko Constitutive Model for a Compressible Nonlinearly Elastic Solid. J Elast. 1996;42: 165–176.

180. Horgan CO, Murphy JG. Compression tests and constitutive models for the slight compressibility of elastic rubber-like materials. Int J Eng Sci. Elsevier Ltd; 2009;47: 1232–1239. doi:10.1016/j.ijengsci.2008.10.009

181. Beatty MF, Stalnaker DO. The Poisson Function of Finite Elasticity. J Appl Mech. ASME; 1986;53: 807–813. doi:10.1115/1.3171862

182. Fung Y, Tong P, Chen X. Classical and computational solid mechanics. World Scientific Publishing Company; 2017.

183. Castro APG, Laity P, Shariatzadeh M, Wittkowske C, Holland C, Lacroix D. Combined numerical and experimental biomechanical characterization of soft collagen hydrogel substrate. J Mater Sci Mater Med. Springer US; 2016;27: 1–9. doi:10.1007/s10856-016-5688-3

184. Holzapfel G. Nonlinear solid mechanics: a continuum approach for engineering. Vol 24 Chichester Wiley. 2000;

185. Lee CR, Grodzinsky AJ, Spector M. The effects of cross-linking of collagen-glycosaminoglycan scaffolds on compressive stiffness, chondrocyte-mediated contraction, proliferation and biosynthesis. Biomaterials. 2001;22: 3145–3154. doi:http://dx.doi.org/10.1016/S0142-9612(01)00067-9

186. Qin X. Matrix Metalloproteinase Inhibition Attenuates Aortic Calcification. Arterioscler Thromb Vasc Biol. 2006;26: 1510–1516. doi:10.1161/01.ATV.0000225807.76419.a7

187. Lee JS, Basalyga DM, Simionescu A, Isenburg JC, Simionescu DT, Vyavahare NR. Elastin calcification in the rat subdermal model is accompanied by up-regulation of degradative and osteogenic cellular responses. Am J Pathol. 2006;168: 490–498. doi:10.2353/ajpath.2006.050338

188. Stein AM, Vader DA, Weitz DA, Sander LM. The micromechanics of three-dimensional collagen-I gels. Complexity. Wiley Subscription Services, Inc., A Wiley Company; 2011;16: 22–28. doi:10.1002/cplx.20332

189. Barocas VH, Tranquillo RT. An anisotropic biphasic theory of tissue-equivalent mechanics: the interplay among cell traction, fibrillar network deformation, fibril alignment, and cell contact guidance. J Biomech Eng. 1997;119: 137–145. doi:10.1115/1.2796072

190. Underwood CJ, Edgar LT, Hoying JB, Weiss J a. Cell-generated traction forces and the resulting matrix deformation modulate microvascular alignment and growth during angiogenesis. Am J Physiol Heart Circ Physiol. 2014;307: H152-64. doi:10.1152/ajpheart.00995.2013

191. Ferrenq I, Tranqui L, Vailhé B, Gumery PY, Tracqui P. Modelling biological gel contraction by cells: mechanocellular formulation and cell traction force quantification. Acta biotheoretica. 1997. pp. 267–293. doi:http://dx.doi.org/10.1023/A:1000684025534

192. Moon AG, Tranquillo RT. Fibroblast-Populated Collagen Microsphere Assay of Cell Traction Force .1. Continuum Model. Aiche J. 1993;39: 163–177. doi:10.1002/aic.690390116

193. Barocas VH, Moon AG, Tranquillo RT. The Fibroblast-Populated Collagen Microsphere Assay of Cell Traction Force - Part 2: Measurement of the Cell Traction Parameter. J Biomech Eng. 1995;117: 161–170.

194. Deryugina EI, Bourdon MA, Reisfeld RA, Strongin A. Remodeling of collagen matrix by human tumor cells requires activation and cell surface association of matrix metalloproteinase-2. Cancer Res. 1998;58: 3743–3750.

195. Chung AWY, Au Yeung K, Sandor GGS, Judge DP, Dietz HC, Van Breemen C. Loss of elastic fiber integrity and reduction of vascular smooth muscle contraction resulting from the upregulated activities of matrix metalloproteinase-2 and -9 in the thoracic aortic aneurysm in Marfan syndrome. Circ Res. 2007;101: 512–522. doi:10.1161/CIRCRESAHA.107.157776

APPENDIX A

CONSTITUTIVE MODELING OF COMPRESSIBLE TYPE-I COLLAGEN HYDROGELS[7]

[7] B.A. Lane, K.A. Harmon, R.L. Goodwin, M.J. Yost, T Shazly & J.F. Eberth. Constitutive modeling of compressible type-I collagen hydrogels, *Medical Engineering and Physics* (2018), https://doi.org/10.1016/j.medengphy.2018.01.003. Reprinted here with permission of publisher.

A.1 ABSTRACT

Collagen hydrogels have been used ubiquitously as engineering biomaterials with a biphasic network of fibrillar collagen and aqueous-filled voids that contribute to a complex, compressible, and nonlinear mechanical behavior - not well captured within the infinitesimal strain theory. In this study, type-I collagen, processed from a bovine corium, was fabricated into disks at 2, 3, and 4% (w/w) and exposed to 0, 10^5, 10^6, and 10^7 μJ of ultraviolet light or enzymatic degradation via matrix metalloproteinase-2. Fully hydrated gels were subjected to unconfined, aqueous, compression testing with experimental data modeled within a continuum mechanics framework by employing the uncommon Blatz-Ko material model for porous elastic materials and a nonlinear form of the Poisson's ratio. From the Generalized form, the Special Blatz-Ko, compressible Neo-Hookean, and incompressible Mooney-Rivlin models were derived and the best-fit material parameters reported for each. The average root-mean-squared (RMS) error for the General (RMS=0.13±0.07) and Special Blatz-Ko (RMS=0.13±0.07) were lower than the Neo-Hookean (RMS=0.23±0.10) and Mooney-Rivlin (RMS=0.18±0.08) models. We conclude that, with a single fitted-parameter, the Special Blatz-Ko sufficiently captured the salient features of collagen hydrogel compression over most examined formulations and treatments.

A.2 INTRODUCTION

Collagen is a naturally occurring polymer that provides a low immunogenic and biologically compatible platform for cellular attachment [151,152]. Type-I collagen, the most abundant of the collagens, endows a diverse group of mammalian tissues with their mechanical properties [153,154]. This material can be processed from primary tissue

sources into acidic solutions, molded into a variety of shapes, and reconstituted into gels using pH neutralization [155]. As such, its applications in biomedical engineering are vast. These applications include scaffolding for tissue engineering, biomimetics, and drug delivery [152,156–158]. Clinically, collagen hydrogels have been used as one of the major constituents of bioactive skin substitutes, corneal shields, and as drug-loaded wound dressings that enhance the healing and recovery processes [159,160]. Injectable collagen hydrogels are currently being investigated to stabilize and improve ventricle remodeling after myocardial infarction [161]. When physically loaded, (e.g., following implantation or when seeded with contractile cells) collagen gels undergo compression and compaction due to the collapse of aqueous voids within the material [162–165]. Accurate interpretation of the response of these materials to applied loads of these (e.g., using finite element analysis), requires the application of an appropriate constitutive model that captures the complex mechanical behavior.

Diverse testing techniques have been employed to measure the mechanical properties of collagen hydrogels (e.g., shear rheometry, tension/compression, indentation, dynamic mechanical analysis). The best experimental tool is selected based on the range of anticipated material behavior, conditions of interest, availability of equipment, and intended material application [155,166–170]. In simple unconfined axisymmetric compression tests, as performed here, two impermeable and rigid parallel plates compress a specimen submerged in an aqueous solution while permitting lateral deformation to occur [155,171]. With the direct measurement of deformed cross-sectional area and force, the Cauchy stress can be calculated at each experimental state and a relationship between the

lateral extension and axial compression (Poisson's ratio) can easily be formulated [127,167,172].

Assuming the orientation of the collagen fibers are random (cf., Figure A.1) and the time-scale of experimentation is such that viscoelastic and plastic effects are negligible, the material can be modeled within the finite strain theory as being nonlinearly-elastic and isotropic [155,163,173–175]. To encompass the salient features of these compressible collagen hydrogels within a mechanical formulation on the continuum scale, we employ an uncommon strain-energy function developed by Blatz and Ko in 1982 [176]. In its full form the model is called the General Blatz-Ko, aptly named after the pioneering work of these two investigators whose original experiments were used to explain a class of foamed polyurethane rubbers in uniaxial and biaxial tension [176]. Despite previous validation in both tension and compression by Beatty and others [176–178], this framework has been used sparingly to model biological tissues. An immediate advantage to this model is that, at most, only three material parameters are needed; one of which is measured directly, another can be measured or prescribed, and the last is related to the fraction of voids within the material. From the General form of the Blatz-Ko, the popular compressible Neo-Hookean and incompressible Mooney-Rivlin models can be derived [179]. A further reduced form, called the Special Blatz-Ko, has only a single fitted parameter thereby greatly simplifying the required mechanical measurements and facilitating comparisons between groups of gels with different material characteristics.

In this work we prepared hydrogels using collagen processed from a bovine corium and modified the hydrogel's mechanical properties through manipulations of concentration, UV crosslinking, and enzymatic degradation. We then tested the hypothesis

that the lesser-known Blatz-Ko material model could provide a better, and simpler, representation of a diverse group of collagen hydrogels under compressive loading compared to the popular Neo-Hookean or Mooney-Rivlin models. As a representative example of the model's utility, we applied these findings to the gel contraction assay using neonatal rat cardiac fibroblasts (NCFs) and calculated the acute energy required to deform this material in culture. In doing so, a constitutive model for hydrogel mechanics was developed and validated that can easily be used to interpret clinical or experimental results.

A.3 MATERIALS AND METHODS

A.3.1 Collagen Isolation and Preparation

Type-I collagen was isolated from a bovine corium through mechanical separation of the dermis and epidermis following the procedure outlined in Yost et al. 2004 [156]. Briefly, hair follicles and non-collagenous proteins were removed using a $Ca(OH)_2$ and a solution of NaHS and subsequently treated with pepsin, grinded with ice, and mixed with acetic acid to create a gel solution. Collagen proteins were then salted out of the solution, collected via centrifugation, and then dialyzed against dH_2O to remove excess salts. A collagen type-I standard and a resultant hydrogel sample of extracted collagen were then pipetted onto a polyvinylidene difluoride (PDVF) membrane and incubated with a mouse primary type-I collagen antibody diluted (1:1000) using Tween Tris Buffered Saline (TTBS) for one hour. The membrane was washed and placed in a secondary goat anti-mouse antibody (1:3000) tagged with horseradish peroxidase (HRP) solution for one hour. After serial washings, the membrane was exposed to 3,3'-Diaminobenzidine (DAB) chromogen which produced a colorimetric change on the membrane after reduction by

HRP. The presence of type-I collagen was confirmed using the dot-blot assay as indicated by a color change on the PVDF membrane upon reduction of the DAB substrate.

The pH of the collagen solution was adjusted to 5.5 and the desired concentrations (2, 3, and 4% w/w) were obtained via dilution and centrifugation. Non-polymerized collagen gels were then loaded into 10 mm diameter by 3.5 mm height molds and subsequently polymerized via pH neutralization using a 10x HEPES buffer (pH = 7.8). To create stiffer gels, a Stratalinker 2400 UV Crosslinker was employed at 10^5, 10^6, and 10^7 μJ. On the other hand, to reduce stiffness, proteolysis was induced via the addition of matrix metalloproteinase-2 (MMP2). Here a pro-MMP2 standard solution was diluted to a concentration of 8 nM with PBS. The MMP solution was subsequently activated with the addition of 40 mM p-aminophenyl mercuric acetate (APMA) solution and incubated for 1 hour at 37°C. Collagen hydrogel disks were then submerged in a 1:1 mixture of activated MMP solution and reaction buffer (50 mM Tris-HCl, 150 mM NaCl, 5 mM $CaCl_2$, 0.0025% Brij-35; pH = 7.5) for 2 hours at 37°C and then removed from the MMP2 solution and placed in PBS supplemented with Ethylenediaminetetraacetic acid (EDTA) to inhibit MMP activity.

A.3.2 Microscopy

A subset of samples were imaged using confocal reflectance microscopy that were first fixed in 4% paraformaldehyde (PFA) at 4ºC overnight and then mounted. A Zeiss LSM 510 Meta (Carl Zeiss Microimaging, Inc.) with a 488 nm wavelength Argon laser and a photomultiplier tube was used with a 475 nm long-pass filter placed before the PMT to detect wavelength reflectance at 475 and 494 nm of collagen fibers in the sample. 63x

was the maximum objective available so that confocal microscopy was used as a qualitative measure of random fiber dispersion within a sample (Figure A.1).

A.3.3 Unconfined Compression Testing

Fully-hydrated disks were submerged in phosphate buffered saline (PBS) and compressed using a MARK-10 mechanical test rig (ESM301-L) with the M5-5 (25 N capacity, 0.005 N resolution) force transducer at rate of 10 mm/min. Synchronous measurements of radial and axial dimensions were taken using a Thorlabs CMOS Camera (DCC1645C) with 1280 x 1024 resolution and a maximum of 24.9 frames-per-second (fps). At least 15 measurements were recorded for each sample at a rate of 1.0 fps. At 13 mm in diameter, the upper platen was sufficiently large so as to provide a continuous surface during radial expansion but small enough to prevent camera interference. We assumed that inertial effects between the solid and liquid phases were negligible at low strain-rates and that the compression surfaces were frictionless so that "simple" compression could occur [180]. This assumption was validated by noting the lack of curvature at the sample edge during compression. Very little change in load or dimensions at maximum compression under static conditions were observed suggesting minimal relaxation. To best recreate the immediate physical response to applied compression, specimens were tested unidirectionally with data collected for a single loading cycle in the loading regime occurring prior to failure. Failure was indicated by discontinuity in the loading curve and a sudden, asymmetric, radial expansion of the sample. Any sample that failed prematurely (i.e., prior to 30% compression), occurring in less than 10% of the samples, was discarded and excluded from mechanical analysis. Experimental Cauchy stress was calculated by $\sigma^{\exp} = f/a$, with $a = \pi r^2$ the current (or deformed) cross

sectional area (r the radius of that deformed area) and f the force measured at the deformed state (Figure A.2).

A.3.4 Cell and Contraction Assay

Rat neonatal cardiac fibroblast cells were cultured to confluence on 75 mm plates and then trypsinized to create a cell-suspension with an approximate concentration of $1x10^7$ cells/mL. Collagen was concentrated to achieve a final 3% (w/w) after the addition of both the cells & HEPES solution. An equal volume of cell suspension and HEPES was added to equal volumes of the hydrogel solutions to provide uniform cell distribution and promote polymerization. After carefully mixing to avoid introduction of bubbles, the collagen-cell mixture, henceforth abbreviated Col1-NCF, was loaded into a mold, covered with 5% FBS supplemented DMEM, and allowed to polymerize overnight in an incubator. The Col1-NCF gel disks were then removed from the mold and were placed into our real-time incubator based contraction chamber (Figure A.7). The contraction chamber consisted of a transparent polystyrene culture dish in which a 3 mm thick polytetrafluoroethylene (PTFE) circular base was placed covering the entire bottom surface. A total of 10 needles (26-gauge) were inserted into the PTFE and then Col1-NCFs disks were gently placed on the PTFE allowing the needle to puncture the center, creating a biologically inert anchor point to maintain a consistent focal length for real-time imaging. Careful examination and manipulation of the Col1-NCFs ensured that no additional boundary conditions or tractions were applied and the Col1-NCF disks did not adhere to the syringe needle or PTFE. Disks were then cultured for more than 7 days, refreshing media every 3 days, with diameter and height measurements recorded daily using a harsh environment camera (EO-1312, Edmund Optics).

A.3.5 Theoretical Framework

Material points in the cylindrically shaped hydrogel are originally at (R,Θ,Z) in an unloaded reference configuration and mapped to (r,θ,z) in a axisymmetric deformed configuration (Figure A.2) so that $r=\lambda R$, $\theta=\Theta$, $z=\Lambda Z$. The deformation gradient for this motion is given as

$$\mathbf{F}=\begin{bmatrix}\lambda & 0 & 0\\ 0 & \lambda & 0\\ 0 & 0 & \Lambda\end{bmatrix}, \qquad [A.1]$$

with the right Cauchy-Green strain tensor represented by $\mathbf{C}=\mathbf{F}^{T}\mathbf{F}$. Compressible material behavior is definded when the determinant of the deformation gradient $\det\mathbf{F}=\Lambda\cdot\lambda^{2}$ is less than 1.

The Cauchy stress tensor for isotropic, homogeneous, elastic, and compressible, materials (i.e., the General Blatz-Ko, Special Blatz-Ko, and Neo-Hookean), is [127]

$$\boldsymbol{\sigma}=\frac{1}{\det\mathbf{F}}2\mathbf{F}\frac{\partial W}{\partial\mathbf{C}}\mathbf{F}^{T}, \qquad [A.2]$$

but for an incompressible material (Mooney-Rivlin model only) we have

$$\boldsymbol{\sigma}=-p\mathbf{I}+2\mathbf{F}\frac{\partial W}{\partial\mathbf{C}}\mathbf{F}^{T}, \qquad [A.3]$$

With p, the Lagrange multiplier used to enforce incompressibility and $\mathbf{I}$ the identity matrix.

The strain energy function W for a homogeneous isotropic elastic material is a function of the principal invariants of $\mathbf{C}$ so that:

$$I_C=tr(\mathbf{C}),\quad II_C=\frac{tr(\mathbf{C})^{2}-tr\mathbf{C}^{2}}{2},\quad III_C=\det(\mathbf{C}). \qquad [A.4]$$

Following the chain rule [9], we have

$$\frac{\partial W}{\partial \mathbf{C}} = \frac{\partial W}{\partial I_C}\frac{\partial I_C}{\partial \mathbf{C}} + \frac{\partial W}{\partial II_C}\frac{\partial II_C}{\partial \mathbf{C}} + \frac{\partial W}{\partial III_C}\frac{\partial III_C}{\partial \mathbf{C}}, \qquad \text{[A.5]}$$

and by definition

$$\frac{\partial I_C}{\partial \mathbf{C}} = \mathbf{I}, \quad \frac{\partial II_C}{\partial \mathbf{C}} = I_C\mathbf{I} - \mathbf{C}^T, \quad \frac{\partial III_C}{\partial \mathbf{C}} = III_C\mathbf{C}^{-T}. \qquad \text{[A.6]}$$

Evaluating the remaining non-zero derivatives of [A.2] or [A.3] using [A.5] and [A.6], and when the appropriate form of W is chosen, [A.6] yields an expression for Cauchy stress. In the case of simple uniaxial compression, the only nonzero value of [A.6] is in the axial direction.

The General Blatz-Ko material model used to represent compressible foamed materials undergoing large deformations has the form [176,179]

$$W = \frac{\mu\alpha}{2}\left(I_C - 1 - \nu^{-1} + \frac{(1-2\nu)}{\nu} III_C^{\frac{-\nu}{1-2\nu}} \right) + \frac{\mu(1-\alpha)}{2}\left(\frac{II_C}{III_C} - 1 - \nu^{-1} + \frac{(1-2\nu)}{\nu} III_C^{\frac{\nu}{1-2\nu}} \right), \qquad \text{[A.7]}$$

where the three material parameters are the shear modulus $\mu > 0$, an interpolation parameter thought to be related to the void fraction $\alpha \in [0,1]$, and the nonlinear Poisson's ratio-like parameter $\nu \in [0, 0.5]$ [181]. Unlike the classic Poisson's ratio, we use a nonlinear form that relates the dependence on axial to radial/circumferential stretch ratios via

$$\lambda(\Lambda) = \Lambda^{-\nu}, \qquad \text{[A.8]}$$

per the ad hoc assumption of [2] and later derived equivalently by [178,181]. It can be shown that for small strains equation [A.8] becomes the linearized and familiar form of

Poisson's ratio $\varepsilon_r = -\nu\varepsilon_z$ with ε the linearized Green strain. This nonlinear form is applicable when the graph of $\ln(1/\lambda)$ versus $\ln(\Lambda)$, in tension or compression, results in a straight line (see, Figure A.3) [178,181].

The physical meaning of α in compression was not immediately evident. For this investigation however, we explore the utility of assigning values to this parameter consistent with the work of other investigators [176,178,179]. First, we consider $\alpha = 0$ so that equation [A.7] becomes

$$W = \frac{\mu}{2}\left(\frac{II_C}{III_C} - 1 - \nu^{-1} + (1-2\nu)\, III_C^{\frac{\nu}{1-2\nu}} \nu^{-1} \right), \qquad \text{[A.9]}$$

and, when a value of $\nu = 1/4$ is assigned, [A.9] becomes the Special Blatz-Ko. On the other hand, with a value of $\alpha = 1$, equation [A.7] becomes

$$W = \frac{\mu}{2}\left(I_C - 1 - \nu^{-1} + (1-2\nu)\, III_C^{-\frac{\nu}{1-2\nu}} \nu^{-1} \right), \qquad \text{[A.10]}$$

which is the strain energy function for a compressible Neo-Hookean material.

In contrast to the compressible forms [A.7], [A.9], and [A.10], an incompressible Mooney-Rivlin material can be found by taking the limit as $III_C \to 1$ and $\nu \to 1/2$ in equation [A.7]. Then [A.7] becomes,

$$W = \frac{\mu\alpha}{2}(I_C - 3) + \frac{\mu}{2}(1-\alpha)(II_C - 3), \qquad \text{[A.11]}$$

The remaining free parameters μ (all models) and α (General Blatz-Ko and Mooney-Rivlin models only) were found via minimizing the residual of the objective function defined by

$$RMS = \sqrt{\sum_{n=1}^{N} \left(\sigma_n - \sigma_n^{\exp} \right)^2 \Big/ N} \,, \qquad \text{[A.12]}$$

where n is the number of discrete measurements of N total measurements in each experimental dataset.

For the cell based gel contraction assay we calculated the stored elastic energy (microjoules) via integration of the strain energy function as [182]

$$\hat{W}(\mathbf{C}) = \int_{-H/2}^{H/2} \int_{0}^{2\pi} \int_{0}^{R} W\left(I_C, II_C, III_C \right) \cdot R \cdot dR d\Theta dZ \,, \qquad \text{[A.13]}$$

with H the undeformed height of the disk. Equation [A.13] provides a metric of acute cell-based gel contraction provided the material is considered elastic. At long time scales (>3 days) plasticity of collagen hydrogels may be observed therefore we only considered acute deformations in the calculation of $\hat{W}$.

A.3.6 Statistical Analysis

All numerical values are expressed as the mean ± standard deviation with 3 to 5 samples in each group of the unconfined compression experiments and 9 samples in the cell based compaction experiments. An uneven two-way ANOVA with Tukey Post-Hoc analysis was performed to find significant differences at $p < 0.05$. Comparisons were made between the parameters (μ, ν, α) of the different constitutive models (General Blatz-Ko, Special Blatz-Ko, Neo-Hookean, Mooney-Rivlin) and for the stress-stretch (σ; λ, Λ) relationships of different collagen treatments (0, 10^5, 10^6, 10^7 μJ UV; MMP2) and formulations (2, 3, 4% w/w). RMS errors were also compared between these groups.

A.4 RESULTS

Confocal reflectance micrographs of a 3% (w/w) gel demonstrate both the initially random microstructural organization of collagen fibers and the inherent material porosity

contained therein (Figure A.1). The nonlinear form of the Poisson's ratio described by equation [A.8] yielded an excellent fit to all experimental data (Figure A.1; $R^2 > 0.976$). No significant differences in nonlinear Poisson's ratio were observed between any experimental groups resulting in an average value of ν =0.29±0.06. Material parameters (Tables A.1-A.3) determined from uniaxial unconfined compression testing (Figure A.2) indicate that the shear modulus increases with w/w collagen (e.g., Special Blatz-Ko: μ =0.198±0.09 to 0.575±0.04 kPa) and exposure to ultraviolet cross-linking (e.g., Special Blatz-Ko 10^7 μJ UV: μ =3.45±0.89 kPa) while decreasing in the presence of proteases (e.g., Special Blatz-Ko: μ =0.119±0.09 kPa). Fitted shear modulus values were slightly higher in the Neo-Hooekan (μ =0.896±0.03 kPa) than the General Blatz-Ko (μ =0.609±0.01 kPa) at 4% w/w. When used as a free parameter, α approaches 0 for all experimental groups except for the 2% gel (General Blatz-Ko: α =0.973±0.05). All other comparisons of μ or α between models failed to reach statistical significance.

A representative stress-stretch behavior of a 3% w/w of collagen hydrogel under unconfined compression can be observed in Figure A.4. Here the General Blatz-Ko, Special Blatz-Ko, compressible Neo-Hookean, and incompressible Mooney-Rivlin models are plotted next to the raw experimental data and a linear fit. The General Blatz-Ko (RMS=0.019) and Special Blatz-Ko (RMS=0.017) provide the best representation of experimental data and, by virtue of similar values for ν and a low value for α in the General Blatz-Ko, are virtually indistinguishable. Subsequently, the compressible Neo-Hookean (RMS=0.057) provides the poorest fit of the nonlinear material models. Collectively the average root-mean-squared fitting error using the General Blatz-Ko material model (RMS=0.13±0.07) was comparable to the Special Blatz-Ko (RMS=0.13±0.07) and much

improved over the Neo-Hookean (RMS=0.23±0.10) or Mooney-Rivlin (RMS=0.18±0.08) material models (Figure A.5). An exception to this was observed for the 2% collagen gels using the Special Blatz-Ko. The Cauchy stress vs. axial stretch ratio fit for all experimental groups using the Special Blatz-Ko is visualized in Figure A.6.

Following an initial seeding period, the Col1-NCF contraction assay demonstrated progressive and isometric contraction for 7 days in culture (Figure A.7) with no statistical significance between axial (Λ = 0.85±0.8) and radial (λ = 0.88±0.03) compaction but considerable volumetric changes were observed ($\det \mathbf{F}$ =0.68±0.7). During this time, gels did not need to be freed from the surrounding material as commonly observed in coated polystyrene dishes since both the PTFE base and stainless steel syringe provided little to no additional traction forces as demonstrated by the free and uniform contraction of these gels. The stored energy from acute deformations using the Special Blatz-Ko model was calculated to be $\hat{W}$ =12.5±7.49 μJ.

A.5 DISCUSSION

Working within the finite strain theory of continuum mechanics, the present work describes the macroscopic mechanical response of collagen hydrogels under unconfined compression testing using collagen harvested and processed from a bovine corium. As expected the shear modulus μ was readily tunable using different collagen treatments and formulations thereby emphasizing the diverse application of this material for a variety of biomedical applications. A nonlinear form of the Poisson's ratio was calculated for each sample and not found to be significantly different between any of the experimental groups. Based on the overall nonlinear mechanical response, we compared four different, but related, constitutive models to find an optimal fit amongst candidates: the General Blatz-

Ko, Special Blatz-Ko, compressible Neo-Hookean, and incompressible Mooney-Rivlin models. Of these, the Special Blatz-Ko provided the best overall fits with the minimum number of free parameters and was therefore used to represent experimental data in Figure A.6.

The Special Blatz-Ko material model is simply a form of the General Blatz-Ko where it is assumed that $\alpha = 0$ and $\nu = 1/4$ [178,180]. This particular model was desirable since, after applying the constraints, μ becomes the only fitted parameter thereby adding considerable simplicity to the requisite mode of mechanical testing for parameter estimation. To this point, the experimentally measured value of the nonlinear Poisson's ratio (equation 8) $\nu = 0.29 \pm 0.06$ was close to the value prescribed in the Special Blatz-Ko model resulting in a good fit to most experimental data. This value was recorded directly in our experiments through measurements of axial and lateral dimensional changes. Other examples of hydrogel mechanics solve for the Poisson's ratio indirectly through an assumed constitutive behavior (linearized), or parameter fitting, rather than being measured directly [183].

The α parameter has been described as being related to the volume-fraction of voids in the material [179]. However, in the original work performed by Blatz and Ko, α was found to be 0 for a 47% void fraction polyurethane foamed rubber in tension while a value of 1 was used to describe a continuum rubber [176,178,179]. Although it was tempting to prescribe the value based on a direct or indirect measurement of the void fraction (e.g., as a structurally motivated model), the physical meaning is not as straight-forward. In our experimental procedure a lower percentage of collagen resulted in a better fit at higher values of α (see Tables A.1-A.3). This seemingly paradoxical behavior suggests that a

better description is that it's value is assigned as an "interpolation parameter" [178,184]" and that the Blatz-Ko model is a purely phenomenological one. Regardless, the overall fitting error for the Special Blatz-Ko (RMS=0.13±0.07) was indistinguishable from the General Blatz-Ko material model (RMS=0.13±0.07) thus with these materials there was little advantage to leaving it as a free parameter - especially for the stiffer gels. We conclude therefor that the Special Blatz-Ko is the preferred model.

Our uniaxial compression measurements are qualitatively similar to those found in [171] at comparable collagen concentrations and loading rates. A notable difference was that the experimental data in that work was presented in terms of the First Piola-Kirchoff stress while ours was Cauchy stress. Note that these two measures of stress are related through the deformation gradient $\mathbf{F}$ [172]. In general, the First Piola-Kirchoff stress would tend to overestimate the Cauchy stress in unconfined compression since the cross-sectional area in the deformed configuration would be greater. In reality we found the radial expansion to be considerable for all samples but surprisingly consistent as indicated by the lack of statistical significance of the nonlinear Poisson's ratio between experimental groups.

To modify the inherent stiffness, ultraviolet light exposure was used to cross-link the collagen molecules (Table A.2) [170,185]. Many other methods of collagen hydrogel crosslinking have also been explored by others including: dehydrothermal treatment, glutaraldehyde, and carbodiimides, and their effects on cell mediated contraction, proliferation, and biosynthesis characterized. In contrast, we also quantified the effect of collagen degradation by the protease matrix metalloproteinase-2 (MMP2), which was found to cause a 37.2% decrease in the Blatz-Ko stiffness parameter (Table A.). MMP2

plays a major role in a variety of diseases and over/under-expression in the cardiovascular system can lead to complications such as aortic aneurysms and calcification [186,187]. A broad-reaching implication of these particular tests was that collagen hydrogels could be used as a test-bed to evaluate the efficacy of neutralizing MMPs to preserve tissue-analogue mechanics.

Although the models presented here capture well the mechanical behavior under these conditions of interest, they are inherently limited to quantification of the macroscopic mechanical response which may differ from the local mechanical environment experienced by adhered cells. Moreover, our focus was exclusively on the elastic (acute) portion of this response. We acknowledge that the operative time scale in hydrogel mechanics is extremely important to the mechanical behavior. Under rapid loading, viscous loss is significant due to the aqueous drag during flux, while at slow or static loading plastic deformation and creep occur as crosslinks can break down over time [188]. Ultimately, the appropriate theoretical framework and constitutive model depends on the anticipated application. For example, at small strains Neo-Hookean behavior is a sufficient descriptor of material behavior but at higher strains the Blatz-Ko models present a better approach to hydrogel mechanics.

Unconfined compression has been used to produced dense collagen matrices representing a more “tissue like” structure [155]. Evidence suggests that without these distinct fiber-alignment techniques that collagen gels are initially isotropic due to the random alignment of fibers within the gel during fabrication [175,189]. The fabrication process used in the present work does not provide any strain- or chemically-driven fiber alignment in the hydrogels, thus allowing the formation of a random fiber network as

shown in the confocal reflectance micrographs (see Figure A.1). Additionally, we avoided preconditioning cycles to maintain the random alignment of fibers in our samples, to minimize fluid loss, and to promote consistency with potential applications (e.g., implantation, laboratory assay, drug delivery) [169].

Cell-based compaction of hydrogels primarily involve observation of the changes in size or shape of the hydrogel and estimation of cell-generated traction forces from the known material behavior [163,165,190–193]. As mentioned earlier, interpretation of experimental results depends on the selection of a suitable material model that can perform under the conditions of interest. As an illustrative example of the utility of the derived constitutive models, we embedded 3% collagen gels with neonatal rat cardiac fibroblasts (Col1-NCF) and observed compaction for one week. In our setup we used a virtually free floating gel with only an axisymmetric boundary applied via the syringe needle. It was clear that this setup enabled consistent and uniform isometric compaction (Figure A.7). Although the magnitude of acutely stored energy among the compressible constitutive formulations for the Col1-NCF materials was virtually equivalent for small strains, larger deformations would likely introduce greater error and therefore utilizing the best constitutive model would generate more accurate results. Incompressible models, such as the Mooney-Rivlin as derived here, are not applicable as volume changes are significant ($\det \mathbf{F} = 0.68 \pm 0.7$).

The gel contraction assay could be used to better inform clinicians of certain cancer or cardiovascular pathologies [194]. For example, Marfan syndrome includes a loss of vascular smooth muscle cell (VSMC) contractility and dysfunctional remodeling due to increased MMP activity which contributes to the formation of aortic aneurysms [195]. With

an aortic biopsy, clinicians could culture explanted VSMCs by placing cells within a collagen gel, with or without MMPs, and observe the cell-based compaction over time. In this manner, candidate therapeutics could be safely be evaluated in isolation while the contractile capacity of these cells is continually assessed. Accurate interpretation of these experiments however, requires the application of an appropriate constitutive model that captures the complex mechanical behavior.

To help explain and interpret tunable collagen mechanics we've employed a constitutive model that was developed for foamed polyurethane rubbers and applied this toward collagen hydrogel mechanics under uniaxial compression. This approach was motivated by experimental evidence that demonstrates the collapse of aqueous voids under compressive strains [193]. The Special form of the Blatz-Ko demonstrated results that are superior to the Neo-Hookean or Money-Rivlin models and comparable to the General form of the Blatz-Ko for all formulations of collagen concentrations greater than 2%. Unconfined compression testing may not be suitable at very low collagen concentrations that are outside of the scope of this paper. We conclude that the single parameter Special Blatz-Ko material model was sufficient for representation of a wide-class of collagen hydrogels but greater errors are introduced at low collagen concentrations. The parameters for this and the other material models are tabulated in this work and can easily be implemented into diverse experimental, analytical, and computational applications.

A.6 ACKNOWLEDGEMENTS

The authors would like to acknowledge the contributions of undergraduate researchers Andrew Shuler, Michael Hendley, Alex Ruppe, and Mary Kay Matula for aid in the processing of collagen from the bovine corium.

A.7 TABLES

Table A.1: Material parameters for the General Blatz-Ko, Special Blatz-Ko, Neo-Hookean, and Mooney-Rivlin models using 2, 3, and 4% collagen gels. * Denotes statistical significance ($p<0.05$) between the experimental group and the 3% while § indicates statistical significance between material model and the General Blatz-Ko model.

		General Blatz-Ko	**Special Blatz-Ko**	**Neo-Hookean**	**Mooney-Rivlin**
2% collagen (w/w)	$\mu(\mathrm{kPa})$	0.313 ±0.14	0.198 ± 0.09	0.317 ± 0.10	0.285 ±0.13
	α	0.973 ± 0.05*	0	1	0.928 ± 0.10*
	ν	0.313 ± 0.07	1/4	0.313 ± 0.07	1/2
3% collagen (w/w)	$\mu(\mathrm{kPa})$	0.370 ± 0.07	0.353 ± 0.09	0.564 ± 0.16	0.372 ± 0.10
	α	0.136 ± 0.24	0	1	2.9E-10 ± 2.6E-11
	ν	0.286 ± 0.05	1/4	0.286 ±0.05	1/2
4% collagen (w/w)	$\mu(\mathrm{kPa})$	0.609 ± 0.01*	0.575 ± 0.04*	0.896 ± 0.03*§	0.607 ± 0.04*
	α	0.105 ± 0.18	0	1	4.4E-12 ± 4.8E-12
	ν	0.332 ± 0.05	1/4	0.332 ± 0.05	1/2

Table A.2: Material Parameters for General Blatz-Ko, Special Blatz-Ko, Neo-Hookean, and Mooney-Rivlin models using a 3% collagen gel at 10^5, 10^6, and 10^7 μJ of ultraviolet light. * Denotes statistical significance ($p<0.05$) between the experimental group and the 3% gel without ultraviolet crosslinking while § indicates statistical significance between material model and the General Blatz-Ko model.

		General Blatz-Ko	**Special Blatz-Ko**	**Neo-Hookean**	**Mooney-Rivlin**
10^5 μJ UV cross-linking	$\mu(\mathrm{kPa})$	0.689 ± 0.26	0.635 ± 0.29	0.980 ± 0.41	0.677 ± 0.30
	α	0.207 ± 0.36	0	1	0.066 ± 0.11
	ν	0.321 ± 0.06	1/4	0.321 ± 0.06	1/2
10^6 μJ UV cross-linking	$\mu(\mathrm{kPa})$	1.92 ± 0.37*	1.90 ± 0.38*	2.89 ± 0.62*	1.98 ± 0.39*
	α	1.6E-10 ± 2.0E-10	0	1	5.1E-11 ± 7.9E-11
	ν	0.332 ± 0.09	1/4§	0.332 ± 0.09	1/2
10^7 μJ UV cross-linking	$\mu(\mathrm{kPa})$	3.43 ± 0.89*	3.45 ± 0.89*	5.66 ± 1.37*	3.63 ± 0.92*
	α	3.7E-11 ± 6.1E-11	0	1	4.0E-11 ± 4.4e-11
	ν	0.21 ± 0.03	1/4	0.214 ± 0.03	1/2

Table A.3: Material Parameters for General Blatz-Ko, Special Blatz-Ko, Neo-Hookean, and Mooney-Rivlin models using a 3% collagen gel and exposure to MMP2. No statistical significance was found between groups.

		General Blatz-Ko	**Special Blatz-Ko**	**Neo-Hookean**	**Mooney-Rivlin**
MMP2	$\mu(\mathrm{kPa})$	0.232 ± 0.09	0.119 ± 0.09	0.297 ± 0.13	0.222 ± 0.09
	α	0.355 ± 0.33	0	1	0.218 ± 0.19
	ν	0.285 ± 0.05	1/4	0.285 ± 0.05	1/2

A.8 FIGURES

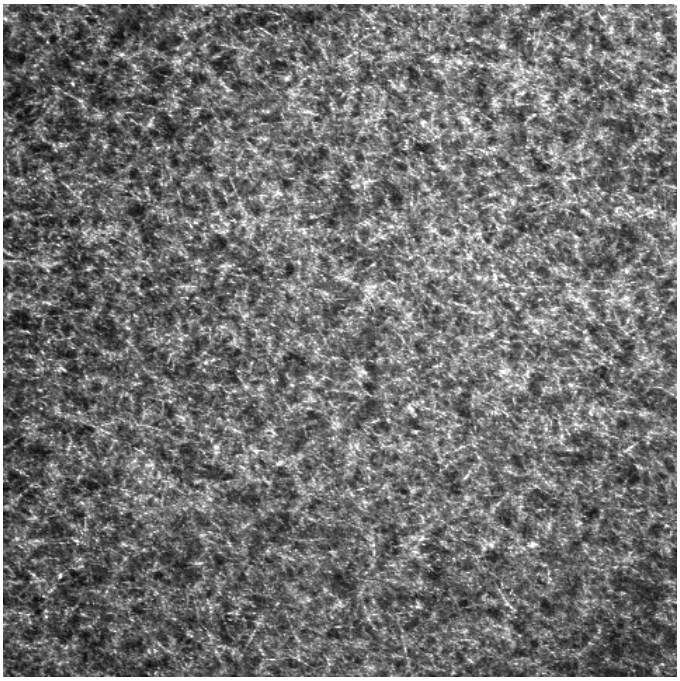

Figure A.1: Confocal reflectance microscopy of a 3% collagen hydrogel. Image recorded with a 63X oil immersion objective to illustrate the random orientation of collagen fibers within the gel.

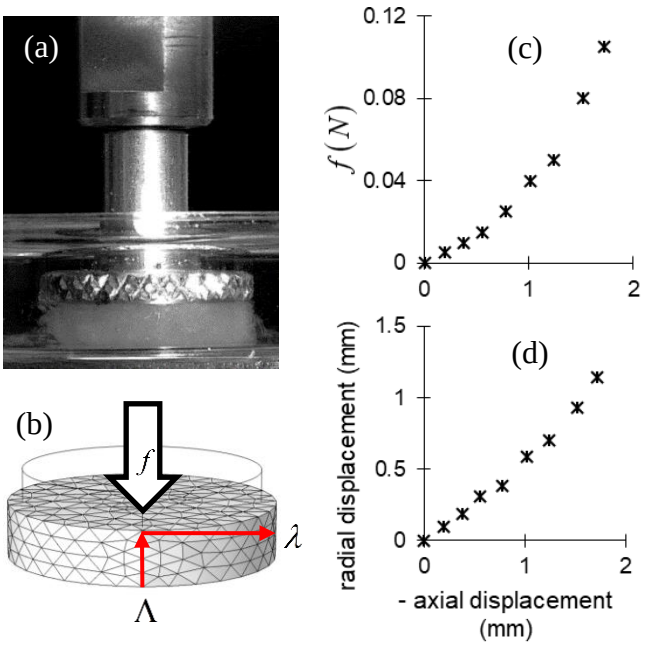

Figure A.2: Uniaxial unconfined compression testing of (3.5 x 10 mm height x diameter) type-I collagen hydrogel disks. (a) Setup illustrating compression testing in an aqueous solution. The image depicts a disk that has already undergone compression. (b) Schematic demonstrating the axial Λ and radial λ stretch ratios as a result of the force f applied during compression testing and a single representative dataset from a 3% collagen hydrogel showing (c) force vs. (-) axial displacement and (d) radial vs. (-) axial displacement.

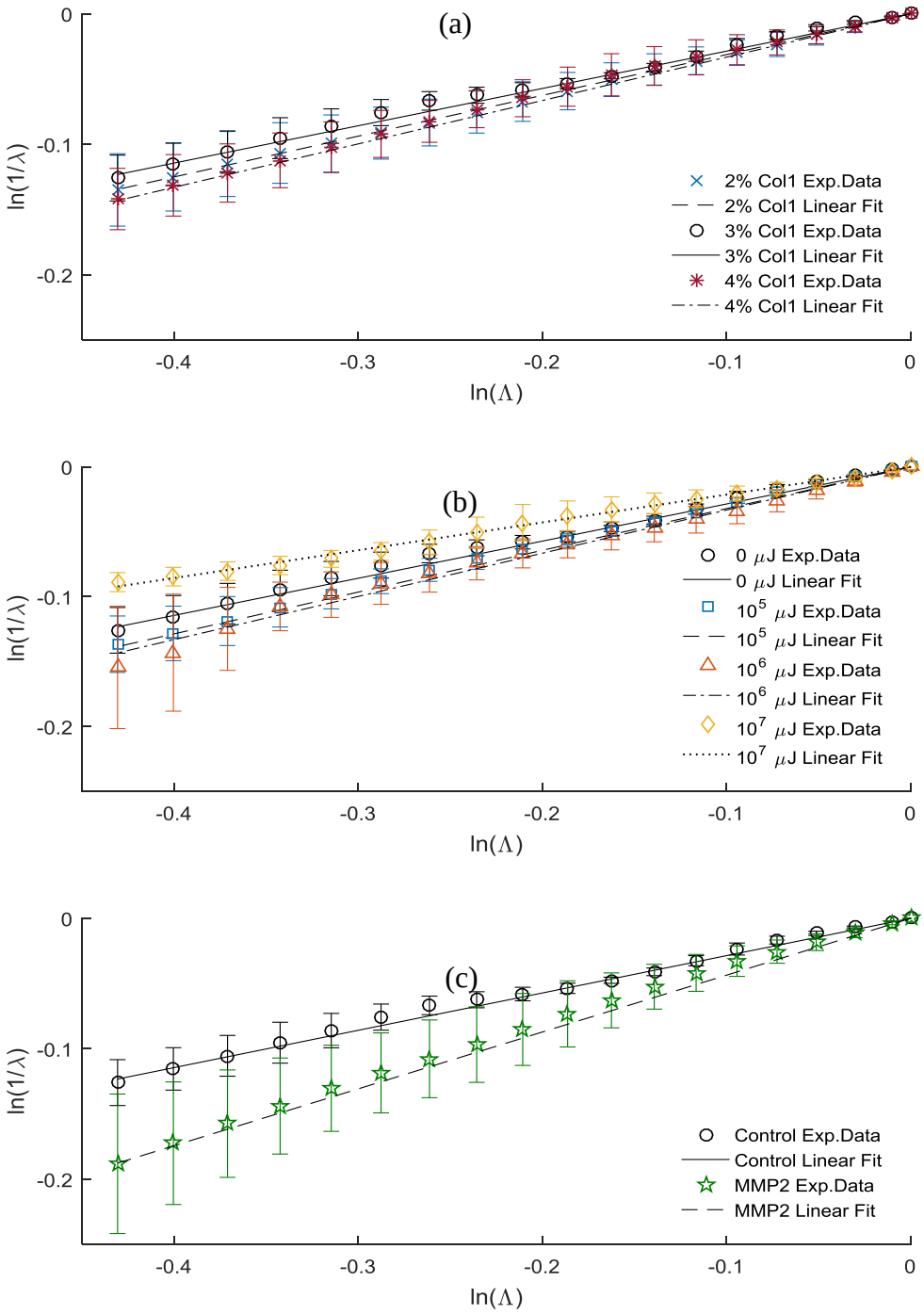

Figure A.3: Experimental and fitted data illustrating the dependence of the radial extension on axial compression for (a) 2% (R^2=0.996), 3% (R^2=0.987), and 4% (R^2=0.989) collagen gels, (b) 3% gels following 0, 10^5 (R^2=0.985), 10^6 (R^2=0.985), and 10^7 (R^2=0.976) μJ of UV crosslinking, and (c) 3% gels (control) exposed to MMP2 (R^2=0.993). The slope of these lines are equal to the nonlinear Poisson's ratio for each group. Error bars ± standard deviation.

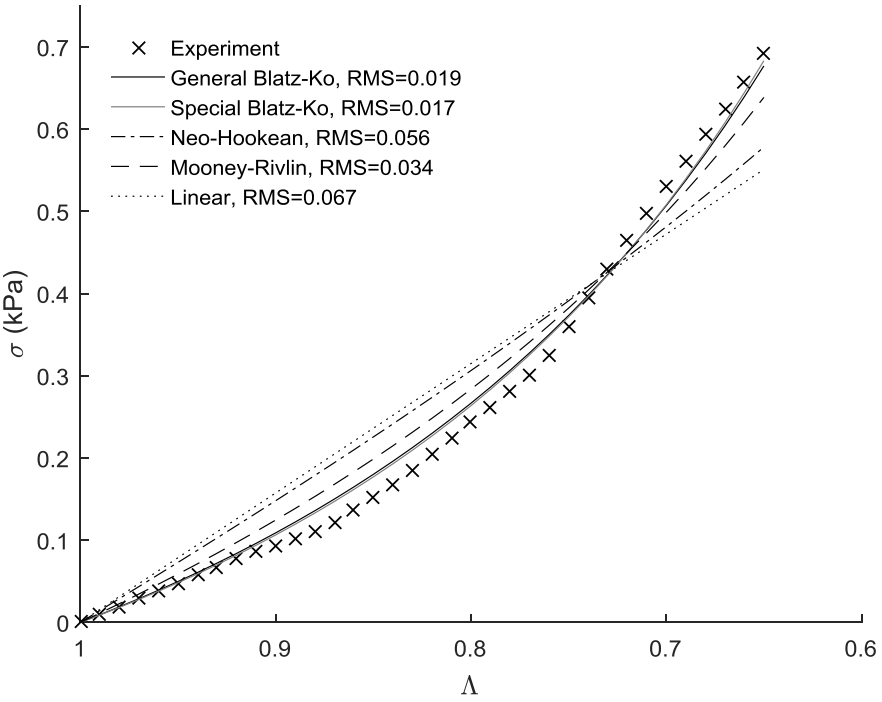

Figure A.4: Example of Cauchy stress vs. axial extension ratio of a 3% collagen disk using different constitutive models. Experimental data is indicated by (×) and modeling results, using the General Blatz-Ko (μ =0.355 kPa, α =0, ν =0.29), Special Blatz-Ko (μ =0.352 kPa, α =0, ν =1/4), Neo-Hookean (μ =0.561 kPa, α =1, ν =0.29), or Mooney-Rivlin (μ =0.371 kPa, α =0, ν =1/2) materials, are illustrated by the continuous curves. A linear (Hookean) fit is shown for comparison. Note that compressive stress is indicated by a positive value.

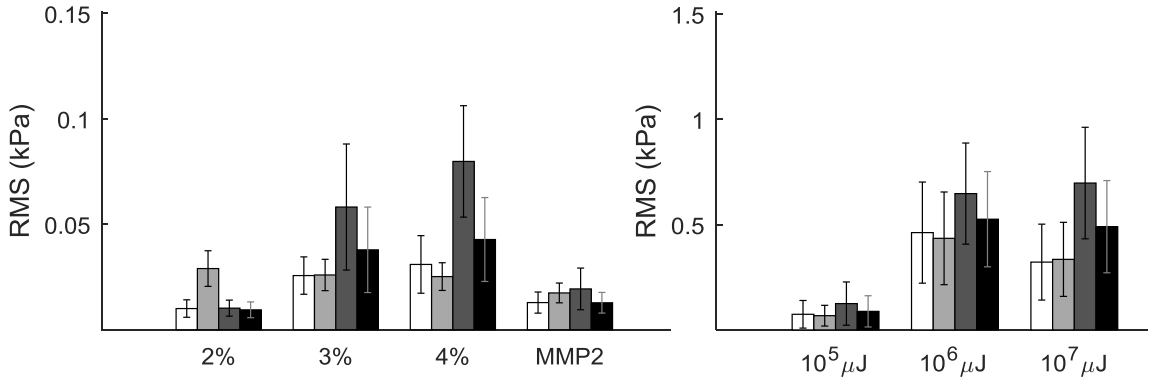

Figure A.5: Fitting errors reported as Root-Mean-Squared (RMS) of experimentally measured stress using the General Blatz-Ko □, Special Blatz-Ko ■, Neo-Hookean ■, or Mooney-Rivlin ■ material models for all collagen hydrogels under unconfined compression. Error bars are ± standard deviation.

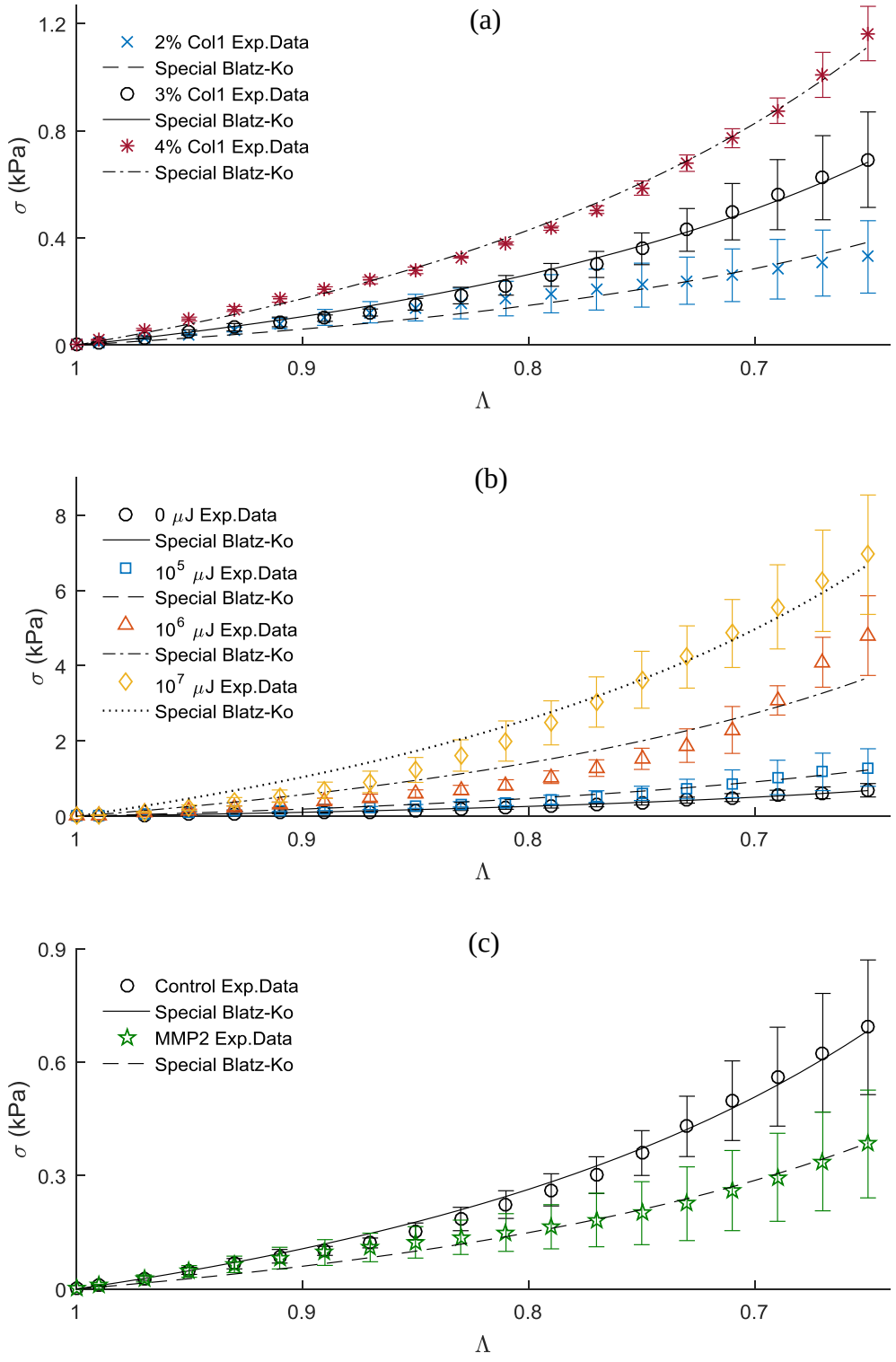

Figure A.6: Cauchy stress vs. axial extension ratio for all groups under unconfined uniaxial compression. Experimental data (symbols) and that data represented using the Special Blatz-Ko model (curves) for (a) 2%, 3%, and 4% collagen, (b) 3% collagen gels following UV 0, 10^5, 10^6, and 10^7 μJ of UV crosslinking energy, and (c) 3% gel exposed to MMP2. Error bars ± standard deviation.

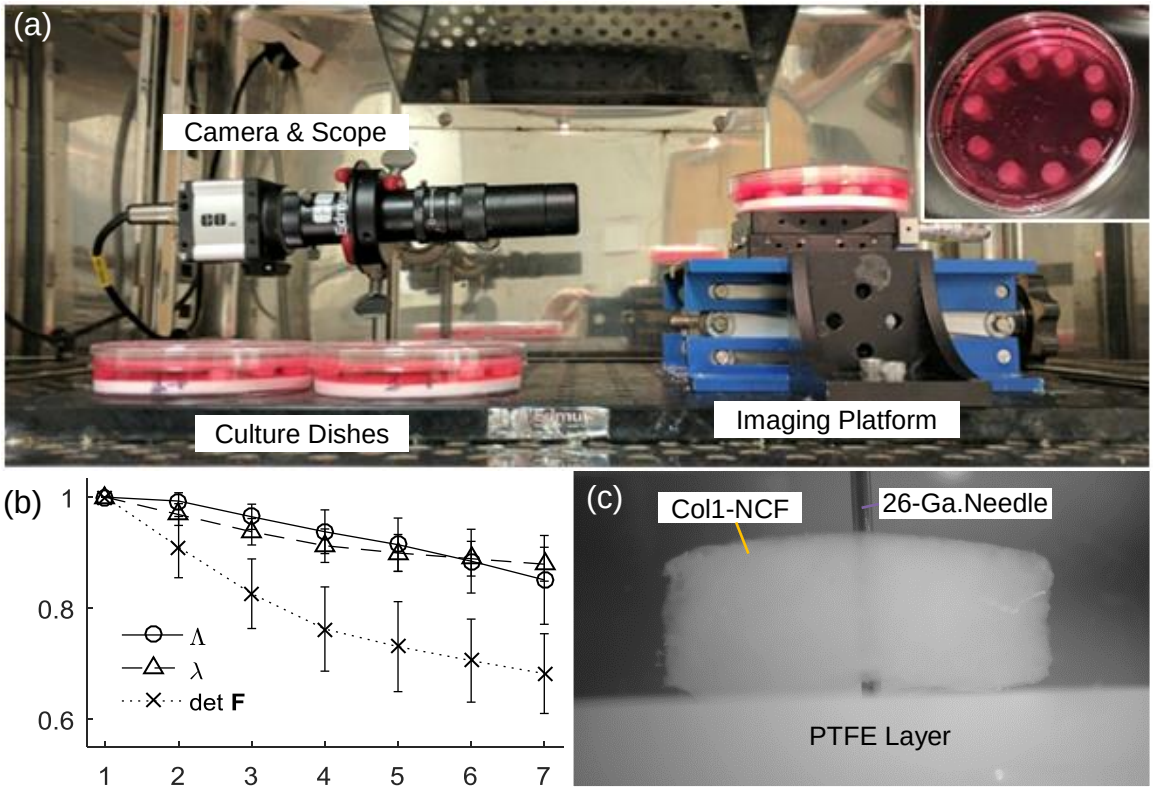

Figure A.7: Gel contraction/compaction experiments using neonatal rat cardiac fibroblasts (Col1-NCF). (a) Incubator setup for real-time contraction/compaction measurements of Col1-NCF floating in culture media (n=9). (inset) Orientation of multiple Col1-NCF disks for batch recording. (b) The measured axial Λ and radial λ stretch ratios plotted next to $\det \mathbf{F} = \Lambda \cdot \lambda^2$ indicates a significant reduction in volume. (c) A sample image of a Col1-NCF after 7 days in culture. A 26-Ga (0.46 mm) syringe needle is located at the center of the disk and anchored in a layer of polytetrafluoroethylene (PTFE) to provide traction free boundaries.

APPENDIX B

COPYRIGHT PERMISSION

Figure B.1: Permission from Journal of Medical Engineering & Physics to include published manuscript in this dissertation (Appendix A).